QUANTUM NANOPHOTONIC INTERFACES IN DIAMOND

A DISSERTATION
SUBMITTED TO THE DEPARTMENT OF APPLIED PHYSICS
AND THE COMMITTEE ON GRADUATE STUDIES
OF STANFORD UNIVERSITY
IN PARTIAL FULFILLMENT OF THE REQUIREMENTS
FOR THE DEGREE OF
DOCTOR OF PHILOSOPHY

Hope Lee
December 2025

I certify that I have read this dissertation and that, in my opinion, it is fully adequate in scope and quality as a dissertation for the degree of Doctor of Philosophy.

Jelena Vuckovic, Primary Advisor

I certify that I have read this dissertation and that, in my opinion, it is fully adequate in scope and quality as a dissertation for the degree of Doctor of Philosophy.

Joonhee Choi

I certify that I have read this dissertation and that, in my opinion, it is fully adequate in scope and quality as a dissertation for the degree of Doctor of Philosophy.

Amir Safavi-Naeini

Approved for the Stanford University Committee on Graduate Studies.

Kenneth Goodson, Vice Provost for Graduate Education

Abstract

Quantum networks promise to connect distinct quantum computing or sensing units through distributed entanglement. Such a network requires quantum nodes, which consist of long-lived qubits with an optical interface. In the recent decade, the group-IV color centers in diamond have garnered great interest and success for this purpose given their optical addressability, compatibility with nanophotonic integration, and spin state coherence. However, high-fidelity state readout and the implementation of entanglement protocols require efficient photon emission, extraction, and routing. In this thesis, I discuss efforts to address these requirements by developing nanophotonic interfaces.

To begin, I review solid state defect centers and their suitability to serve as spin qubits. I then motivate our interest in negatively charged group-IV color centers in diamond, with a detailed discussion of their optical and spin properties. In this section, I summarize our experimental progress in optical spin state initialization and readout, and in microwave spin control. I discuss the current limitations to our spin state readout fidelity, and the consequent necessity for nanophotonic interfaces to improve both photon collection efficiency and photon emission rate. I next proceed to introduce the specific type of nanophotonic interface—the one-dimensional photonic crystal cavity—that was of focus of my work.

In the next chapter, I present our results coupling the tin-vacancy center (SnV^-) to one-dimensional photonic crystal cavities fabricated in a thin-film diamond platform. We demonstrate, via the Purcell effect, enhanced photon emission rate from a color center. Furthermore, we develop a model to describe the spontaneous emission dynamics of our system. By considering both the orthogonality of the SnV^- C/D transition dipoles and the C/D branching ratio, we develop a rigorous, novel method to extract Purcell factors. Next, I discuss the heterogeneous integration of diamond color centers to thin-film lithium niobate photonics. We report high efficiency photon channeling between the two material platforms and optical addressing of SiV^- centers. Our preliminary demonstration paves the way for on-chip quantum frequency conversion and long distance photon routing. Lastly, I will discuss the extensions of my work towards the development of quantum nodes based on group-IV color centers in diamond.

Acknowledgments

Qubits may need to live in a vacuum, but humans don't—and honestly probably shouldn't. Therefore, my preciously limited time at Stanford was only possible due to a legion of others, both in my professional and personal spheres, who have gifted me a fount of support.

I would like to start by thanking of thesis advisor, mentor, and scientific role model Professor Jelena Vučković. Her influence and guidance both in technical fields and beyond will most definitely persist well into the rest of my career. I told this story in person during my defense, but it wouldn't hurt to immortalize it in writing: during the 2nd year of my PhD, some visitors visited the lab two days in a row. The first day, Jelena described the quasi-isotropic diamond undercut (refer to Chapter 3), gesturing to describe how difficult it is for the O_2 plasma to make its way up into device structures. The next day, I was encouraged to explain this process, and I found myself, halfway stumbling through the description, making the *exact* same hand gesture as Jelena. I am sure moments like this will only continue to occur with the coming months and years. Jelena, thank you entertaining that naive cold email all the way back in 2019-2020, and giving me the chance to learn from you and the group.

Talking about cold emails, it would also be remiss of me not to thank my undergraduate research advisor and mentors: Professor David Awschalom, Chris Anderson, and Alex Crook. In a even greater degree of naivete, I sent an email to Chris inquiring about working in the Awschalom group as an undergraduate. I emailed Chris since his name was first, alphabetically, on the group webpage. Chris, very graciously, replied and gave me advice for how best to reach out to Prof. Awschalom. Now, having gone through the graduate school process, I have come to appreciate how generous it was for him to entertain my nearly one dozen emails. Alex Crook very kindly served as my direct mentor and took the time to get me started in the cleanroom even as just a second year undergrad. Even more remarkably, he afforded me the trust to work with actual samples! Independently! In a brand new nanofabrication facility! (My time at the PNF spoiled me somewhat, as I came to believe every ebeam writer can be booked at 10 am in the morning for 2pm the same day.) The generosity with time and resources that I was offered was truly a privilege.

I would also like to thank my labmates and mentors that I had the chance to work with here at Stanford. It has been a wonderful experience to learn from, work alongside, and, sometimes, waste time with such fantastic people.

Alison, Shahriar, and Daniel were the leaders of the diamond subteam when I joined the project. Alison was wonderfully kind and insightful; my only regret was that I didn't have a chance to interact with her more before she graduated and moved on to greener pastures. I've always appreciated Shahriar's pragmatic evaluations which I could tell helped organize and direct our efforts. Daniel was an excellent mentor who trained me in the optics lab and explained fundamental concepts half a dozen times until they lodged themselves in my brain. Indeed, Daniel was also the one to teach me the critical quasi-isotropic undercut (the fabrication procedure that builds character.) We've had multiple post 9 pm chats in the lab after long days of fab. If Daniel, Alison, and Shahriar constitute the 'Diamond Old Guard,' then Hannah, Abby, and Dominik constitute the 'Diamond New Guard.' Abby and Hannah are both extraordinary, insightful and driven. It has truly been a delight to work with them over the last few years. I honestly don't think I would have had the emotional strength to make it through my PhD if not for knowing that I got to work with such amazing subteam members. I remember meeting Hannah for the first time when she visited and I think we discussed how not to kill our respective pothoses—mine are still alive, and I hope yours are too. And I remember sitting with Abby and Yakub in Tressider when Abby was starting out in the group, and she asked at what point a graduate student would feel like they 'know things.' I think in retrospective, the answer might be 'never,' but that might also be purpose of the whole ordeal. Dominik arrived a little more recently, but with a unique dedication and diligence that will be perfect for the struggles, frustration, but also excitement that diamond has to offer.

I would also like to thank the Stanford fabrication technical and support staff. The cleanrooms are large and users are many, but the staff remain diligent and responsive, which could not possibly be easy. None of the work presented in this thesis would've been possible without their constant support and maintenance of the shared facilities.

Outside of the lab, Dominic, Yakub, and Jason have been not only been wonderful collaborators and labmates, but also superb weekend drinking buddies. I must thank them for all the interesting times and experiences, such as Dominic introducing me to beer pong or Jason joining me in surviving overnight in the Denver airport. There have been many 'depression Coupa' moments with Yakub where we sought out coffee and the sun to reorient ourselves, before we descended back into the subbasement labs to meet our fates.

Lastly, I want to thank my friends and my family. Whether it was monthly discord calls or getting to meet up in person at conventions. To Sid, you are, as I often remind you, truly the strangest man I have ever met. But I wouldn't choose to spend the last 5 years doing laundry and dishes, and debating how lazy we can be for dinner with anyone else. To Clare, Mom, and Dad, thank you for the endless and unconditional support. Clare—you are talented and hardworking and so much better adjusted as a human being than I will ever be. Mom and Dad, somehow you never gave up on me—thank you for that unwavering trust and support.

Contents

List of Tables

List of Figures

Chapter 1

Introduction

1.1 Overture

The story of quantum technologies began in the 20th century. In 1900, at a conference, Max Planck proposed energy discretization in order to rectify a troubling discrepancy between theoretical prediction and experimental observation for blackbody radiation spectra. In Plank's paper, 'On the Theory of the Energy Distribution Law of the Normal Spectrum,' he suggested that energy in the spectrum be composed of discretized 'energy elements' [1]; the energy for each element would be proportional to its frequency by some factor h. Although December 14th, the day of Plank's presentation, is now celebrated as the birthday of quantum physics, the far-reaching ramifications of Planck's *ad hoc* proposal was initially overlooked, and indeed Planck himself referred to his proposal as 'an act of desperation' [1] [1].

Fortunately, this thread of reasoning was soon picked up by Einstein in 1905 during his efforts to explain the photoelectric effect [1]. When a metal is illuminated by UV light, electrons are expelled from the metal surface. However, this phenomenon showed a dependency on the frequency of illumination. Below a characteristic frequency, no electrons are expelled regardless of illumination intensity. To explain this phenomenon, Einstein extended Planck's idea of quantization to free radiation, or light itself, effectively introducing the concept of the 'photon.'

Gradually, over the next 25 years, from the efforts of Heisenberg, Schrödinger, and Dirac, this nascent idea of quantization was substantiated by matrix mathematics, the wave equation, and special relativity [1]. In 1924, Born coined the term 'quantum mechanics' to name this new burgeoning field of physics [1]. Henceforth, the sweeping consequences of this new theory—the uncertainty principle, entanglement, superposition, just to name a few—have colored all corners of modern sciences.

The second chapter of this saga started in 1947, with the first demonstration of the transistor, at Bell Laboratories by Bardeen and Brattain [1]. The first 'point-contact' transistor was greatly

---

[1] This is also how I describe my experience writing these pages.

unwieldy and impossible to manufacture, being roughly fist-sized and inferior in performance to the vacuum tube. However, within a single year, Shockley theorized the p-n junction transistor, which was experimentally demonstrated in 1950 [1]. Production of these miniaturized devices was first adopted by General Electronics, and then Texas Instruments, who made the all-important switch from using germanium to silicon. Within just another decade, by the 1960's, integrated circuits with transistors have began to enter the civilian market, and semiconductor CMOS processing cemented itself as a keystone of modern technologies [1].

Skipping forward to the 21st century, these two branches, of quantum physics and semiconductor processing, have intertwined themselves ever more closely through the emergence of the field of quantum technologies. These emerging technologies aim to harness the properties demonstrated by quantum physics, which, when combined with the scalability and integration of device engineering, may deliver novel capabilities in computation, simulation, communication, and information processing.

1.2 Qubits

In direct analogy to the 'bit,' the foundational informational unit for modern computational and communication paradigms, the 'qubit' or quantum bit underlies current established conventions for quantum technologies. Similar to the classical bit, the conceptual qubit consists of two energy levels that encode binary logical states, notated as $|0\rangle$ and $|1\rangle$.

However, as a consequence of its quantum nature, the qubit can be prepared as in a superposition of these two energy states, expressed in the form:

$$\begin{aligned} |\psi\rangle &= c_0 |0\rangle + c_1 |1\rangle \\ &= e^{i\phi}\sin(\theta/2) |0\rangle + \cos(\theta/2) |1\rangle \end{aligned} \tag{1.1}$$

In this generalized example, the qubit, when measured, will have some probability $|c_0^2|= \sin^2(\theta/2)$ and $|c_0^2|= \cos^2(\theta/2)$ of being found in the logical states $|0\rangle$ and $|1\rangle$, respectively. By definition and construction, the state is normalized such that $|c_0^2|+|c_0^2|= 1$. For realistic qubits, large effort and attention is given to the preservation of θ and ϕ of a prepared superposition. The duration for which a superposition can be maintained is referred to as the dephasing or T_2 coherence time. On a related note, the energy relaxation time, T_1, refers to the duration a qubit prepared in the higher energy state $|1\rangle$ can remain in the state until it decays.

For a system with two qubits, a general state formed from a tensor product can be written (disregarding normalization):

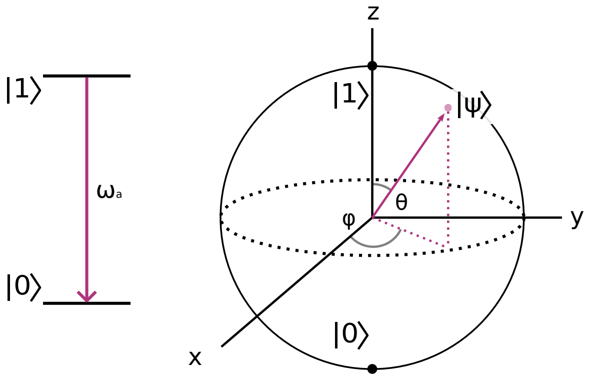

Figure 1.1: Qubit and Bloch sphere schematic.
An ideal qubit consists of two energy levels ($|0\rangle$, $|1\rangle$), with a transition frequency of ω_a. This qubit is also often referred to as a two-level system. A Bloch sphere serves as a useful tool to visualize the state and evolutions of a qubit. A pure state is represented by a vector of unit length (ie. $|\psi\rangle$), and characterized by θ and ϕ.

$$\begin{aligned} |\Psi_o\rangle &= (c_{0,A}\,|0\rangle_A + c_{1,A}\,|1\rangle_A) \otimes (c_{0,B}\,|0\rangle_B + c_{1,B}\,|1\rangle_B) \\ &= c_{0,A}c_{0,B}\,|0\rangle_A\,|0\rangle_B + c_{1,A}c_{0,B}\,|1\rangle_A\,|0\rangle_B + c_{0,A}c_{1,B}\,|0\rangle_A\,|1\rangle_B + c_{1,A}c_{1,B}\,|1\rangle_A\,|1\rangle_B \end{aligned} \tag{1.2}$$

The measurement results for this state as a whole are identical to if the two qubits were measured entirely independently. However, it is also possible to construct state which is not separable in this fashion, for example:

$$|\Psi\rangle = c'_0\,|0\rangle_A\,|1\rangle_B + c'_1\,|1\rangle_A\,|0\rangle_B \tag{1.3}$$

These entangled states demonstrate varieties of correlations which can not be replicated with systems constructed of classical bits. For instance, in the presented example state $|\Psi\rangle$, a measurement of solely qubit A immediately informs the resulting state of qubit B, as the combined system can only be in either the state $|0\rangle_A\,|1\rangle_B$ or $|1\rangle_A\,|0\rangle_B$, with probabilities $|c'_o|^2$ and $|c'_1|^2$, respectively.

Although presented here through a decidedly incomprehensive summary, superposition and entanglement serve as some core differences between quantum systems and their classical counterparts. By consequence, a quantum computer may be capable of solving problems or simulating systems which are classically intractable [2, 3]; a quantum network could connect discrete computing units with unprecedented levels of security [4, 5]. Furthermore, these quantum principles can be employed to perform measurements of physical quantities with levels of sensitivity and precision beyond those feasible classical analogs [6].

In 1996, the requirements for physical realization of quantum technologies were delineated by

DiVincenzo [7]. For computing purposes, a quantum system requires:

1. Scalable and well-characterized qubits.
2. The ability to initialize qubits in arbitrary states.
3. Sufficiently long coherence times for qubit states.
4. Implementation of a 'universal' set of gates.
5. Accurate measurement of final results from qubits.

And furthermore, in order to network distinct computing units, DiVincenzo described the necessity of 'flying' qubits which transmit the quantum information, contrasting with 'stationary' qubits which perform the computational tasks. A quantum network, according to DiVicenzo, requires in addition to the aforementioned:

1. Interconversion between the 'stationary' and 'flying' qubits.
2. High-fidelity transmission of 'flying' qubits between target locations.

There is a large number of different candidate qubit platforms which may fulfill the listed criteria; for stationary qubits, the current front-runners may be roughly divided into two categories. The first are mesoscopic qubit candidates, which often rely on CMOS and circuit technology, such as the family of Josephson-junction-based superconducting circuits or semiconductor quantum dots [8, 9, 10]. In particular, super conducting qubits are well marketed and ambitiously pursued by many industry players. The fabrication and control techniques required for these qubits are relatively mature, and therefore the path towards scalable manufacturing seems clear [11]. However, as a drawback, this category of qubits suffers from stringent temperature requirements. To maintain qubit coherence, milliKelvin temperatures are required, necessitating large dilution refrigerators which introduce significant infrastructure overhead.

The other category are 'atomic' style spin qubits such as trapped ions or atoms, quantum dots, molecules, and solid state defect centers, which utilize the spin states of a species of choice as a qubit [12, 13, 14]. For many of these candidates, they also possess optically active orbital states. Through spin-orbit coupling, the qubit state can therefore be initialized, manipulated, and readout via optical means. This is an attractive feature as an intrinsic spin-photon interface fulfills both of DiVicenzo's requirements for quantum networks, with the spin qubit operating as the 'stationary' qubit, and the emitted photon fulfilling the natural role of 'flying' qubit.

1.3 Thesis Overview

My work presented in this thesis will focus on solid state defect centers and their integration with nanophotonics. In Chapter 1, I will discuss solid state defect, or color, centers, focusing on those hosted in diamond. Using the NV^- as representational system, I will briefly discuss some common considerations for all color centers before describing in detail the characteristics of my primary color centers of study: the SnV^-, and in lesser part the SiV^-. In the second half of this chapter, I will discuss the integration of color centers and nanophotonics for the purpose of efficient photon extraction and spin qubit readout through introductions to cavity quantum electrodynamics (CQED) and photonic crystals.

In Chapter 3, I will detail our efforts to integrate the SnV^- with one-dimensional photonic crystal cavity resonators, fabricated in a thin-film diamond platform. In this chapter, I will illustrate evidence of emitter-cavity interaction, as well as present a model developed to rigorously determine Purcell enhancement factor.

Next, in chapter 4, I will both motivate and describe our efforts to heterogeneously integrate diamond and diamond color centers with another photonics platform: thin-film lithium niobate. We present in this section high efficiency photon transfer between the two materials, which paves the way for quantum frequency conversion of color center photons.

Lastly, in Chapter 5 I will delineate future directions of this work, before concluding with a summary of this thesis.

Chapter 2

Quantum Nanophotonics

2.1 Solid State Defect Centers

Solid state defect centers, also referred to as color centers, consist of a controlled defect in a crystal lattice. A semiconductor crystal lattice, stemming from its atomic periodicity, possesses an electronic band structure. A defect, formed from a combination of vacancies and substitutional and/or interstitial atoms, forms a predominantly isolated set of bound energy states within the band gap. In this sense, the defect center can be considered a artificial trapped atom or ion in the solid state.

2.1.1 Diamond and the NV^- Center

Over the last two decades, diamond has demonstrated exceptional success as a host lattice for solid state defect, or color, centers [15]. Despite being an 'exotic' material with limited availability and difficult processing, diamond is nevertheless a semiconductor and possesses a range of unique properties. Composed entirely of carbon with tetrahedral bonds, diamond possess a wide $\sim$5.5 eV ($\sim$225 nm, well into the UV) bandgap, offering a large wavelength transparency range and separation of defect energy structures from the valence and conduction bands [16]. Furthermore, diamond has a remarkably high Debye temperature of $\Theta = 2000$ K [17]. The Debye temperature effectively describes the 'stiffness' of a material, with higher temperatures corresponding to 'stiffer' materials; a material with a high Debye temperature possess a reduced population of thermal phonons and is therefore mechanically quiet. Lastly, carbon in its natural isotope mixture is 98.9% ^{12}C, which possess no nuclear spin. Indeed, in artificially grown diamond, the remaining nuclear spin environment can be removed through isotope purification. Or, through isotope engineering, precise densities of nuclear spins can be introduced during diamond growth or defect implantation to be used long-lived spin memories [18]. From these properties, diamond positions itself as an exceptionally quiet solid state

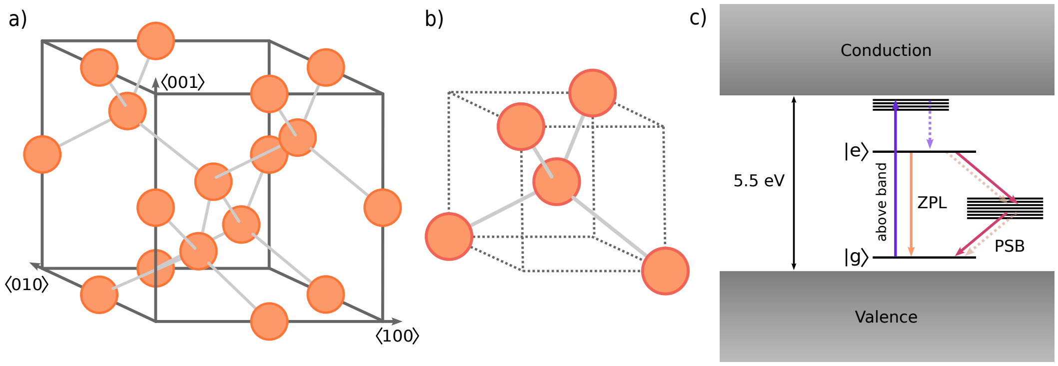

Figure 2.1: Diamond crystal structure and bandgap schematic.
(a) Crystal lattice structure of diamond; the orange spheres represent carbon atoms, bonded in a tetrahedral geometry. **(b)** A single unit cell of the diamond crystal cubic lattice. This designation can be visualized by the dashed gray lines. **(c)** Schematic of diamond bandgap and embedded color center transitions. For a viable defect center in diamond, its orbital transitions must fit within the 5.5 eV bandgap of the host material. Direct transitions within the energy structure is referred to as the zero phonon line (ZPL, yellow) of the color center, while phonon-assisted transitions make up the red-shifted, broadband phonon sideband (PSB, red). During photoluminescence (PL) spectroscopy, above band illumination (purple) excites the color center electronic state to a higher energy continuum of phononic states. The defect can then relax back to the orbital excited state, before decaying to the ground state through either the ZPL or PSB pathways.

environment: electronically, thermally, and magnetically. Such a material is the ideal host for long-lived defect center spin qubits.

Color centers in diamond have been studied and cataloged for geological and gemology purposes long before single defect centers were identified as individually addressable spin qubits [19, 20]. The primogenitor color center to be recognized as a spin qubit was the negatively charged nitrogen vacancy center (NV^-), which is composed of a substitutional nitrogen atom partnered with a single carbon vacancy (Fig. 2.3) [15]. The NV^- possesses a permanent dipole moment, pointing towards the carbon vacancy site. In the last decade, the NV^- has demonstrated great success serving as a qubit in long-distance quantum networks [21, 22, 23, 24, 25, 4] and as an excellent quantum sensor [26, 27]. We will use the NV^- as a representational system to discuss some shared considerations regarding color center defects.

Although its energy structure is relatively insulated from the valence and conduction of the diamond host lattice, a color center can still interact with its surrounding lattice through phonon-assisted processes. When a defect center is excited, there is some probability, referred to as the quantum efficiency, that the center will radiatively decay. A further fraction of these radiative decay events, referred to as the Debye-Waller factor, will consist of a direct, coherent transition between energy states. The coherent photons emitted have well-defined wavelengths and lifetimes, and constitute the zero-phonon line (ZPL). The remaining fraction of radiative decay events involves interaction with the crystal lattice and are phonon mediated; these emitted photons are therefore both red-shifted from the ZPL and very broadband in frequency distribution, and form the phonon sideband (PSB) (Fig. 2.1).

Photoluminescence (PL) and photoluminescence excitation (PLE) are cornerstone techniques to characterize a sample with color centers. In the former, an above-band laser excites the color center electronic state to a continuum of higher energy phononic states. For a portion of these excitations, the defect center then relaxes back to the excited state and subsequently decays to the ground state through either through ZPL and PSB pathways. By scanning an excitation spot across the surface of the sample and counting the photons collected within the ZPL and/or PSB wavelength range, we can construct a spatial map of color center locations. Upon further probing of these color center locations, the collected signal can be routed to a spectrometer to construct a spectrum of color center PL. Given that the exact lattice conditions surrounding the color center (ie. electric field noise, strain) can differ and are often not characterized, the PL spectrum provides the precise ZPL wavelength for the defect of study. Up to this point, only non-resonant addressing of the color center has been discussed. In PLE, the defect center is now excited with a laser near/on resonance with the ZPL wavelength; PSB photons are collected. As the laser tunes onto resonance with the ZPL, the efficiency of excitation increases, leading to a greater number of decays, and therefore increased PSB counts. Therefore, although non-resonant photons are collected, PLE provides key information regarding a color center's ZPL wavelength, linewidth, and stability [28, 29, 30, 31]. Lastly, if the resonant excitation laser can be filtered from the collection, for example through temporal or polarization filtering, the ZPL emission can then be collected. This scheme of resonant excitation and resonant collection is referred to as resonance fluorescence [32, 33, 34]. Examples of PL and PLE characterization are provided in Fig. 2.2.

Thus far, the discussion have focused on just the orbital transitions of the color center. To actually encode quantum information and realize a long-lived qubit, we must now address the spin degree of freedom of the color center. The NV^- center electronically consists of 6 electrons, which forms a s=1 spin system. In the absence of a magnetic field, the NV^- has two ground states, with spin $m = 0$ and $m = \pm 1$. These two states can be used to realize a spin qubit, and addressed via microwave excitation tuned to their splitting of 2.87 GHz. The degeneracy of the $m = \pm 1$ manifold can be lifted via the Zeeman effect, and a spin qubit defined from any two out of the three available ground spin states. The qubit state can be initialized by optical-spin pumping given the dipole selection rules of the NV^- center, such that resonant excitation preferentially initializes the qubit to the spin $m = 0$ state. As the $m = \pm 1$ excited spin state decays into the intermediate singlet states with greater probability, different spin states result in differing PL intensity. Therefore, PL count rate can serve as readout of the spin state. As a note, the exact details of the spin initialization and readout scheme differ from color center to color center, depending on the exact energy and spin states of the qubit. However, in general, some form of optical spin initialization and fluorescence

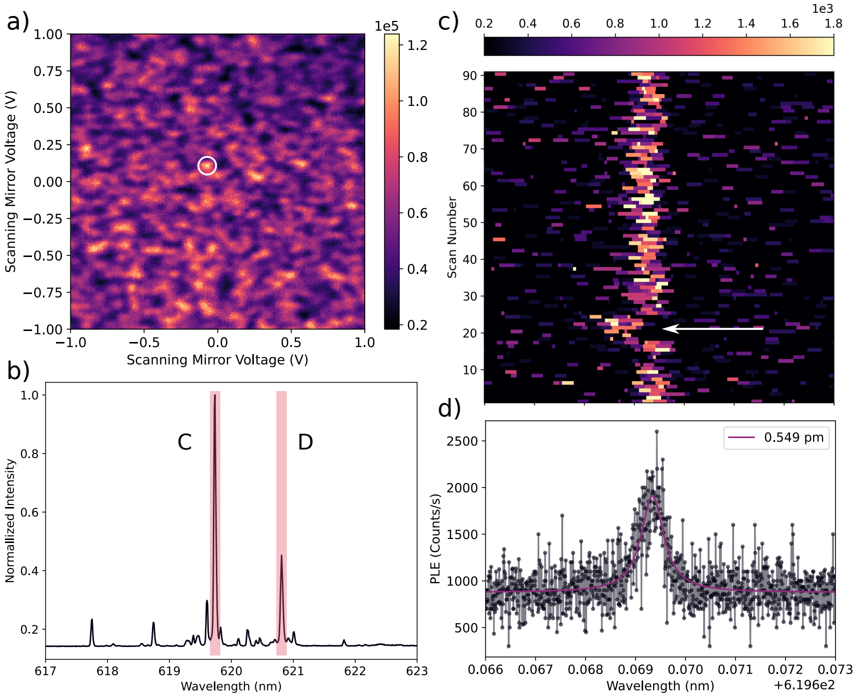

Figure 2.2: Example of SnV^{-} PL and PLE characterizations.
(a) PL confocal scan of an SnV^{-}. The color bar indicates counts collected per second. **(b)** PL spectrum example. The collection spot is indicated by the white circle in (a). The 'C' and 'D' transitions of a selected color center is indicated by red shading. Given the high implantation density of the sample in this example, the collection spot consists of a SnV^{-} color center cluster. Therefore, resonant addressing is necessary to selectively target a single defect center. **(c)** PLE traces taken over ∼15 minutes. The laser is scanned to resonantly excite a selected SnV^{-} transition and the PSB is collected. PLE effectively traces out the ZPL transition linewidth, and can also provides information regarding the color center stability; for instance, the white arrow points to a brief jump in PLE wavelength. Panel (c) shares an x axis with panel (d). **(d)** Averaged PLE. The traces in (c) are averaged and then fit to Lorentzian. The averaged PLE linewidth for this example is 0.55 pm, which translates into ∼440 MHz, which is noticeably broadened. For the SnV^{-}, linewidths down to ∼30 MHz have been reported [28].

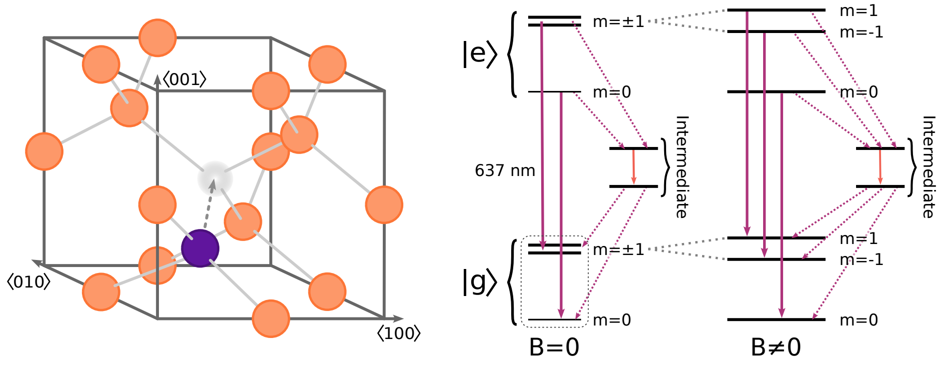

Figure 2.3: NV$^-$ color center atomic and energy structure.
The atomic structure of the NV$^-$ center (left) is composed of a substitutional nitrogen atom (purple) next to a carbon vacancy (gray). The NV$^-$ possesses a permanent dipole which points towards the vacancy site (dashed gray arrow). The orange circles represent carbon atoms. The orbital and spin structure of the NV$^-$ is given to the right. In the absence of a magnetic field (B=0), the $m = 0$ and $m = \pm 1$ spin states are separated by 2.87 GHz and can function as a spin qubit (dashed gray box). The dashed purple lines indicate non-radiative transitions of the NV$^-$ to/ from the intermediate singlet states. Non-radiative decay transition between the excited $m = \pm 1$ and intermediate states therefore allows for initialization into the $m = 0$ spin state via optical spin-pumping. At non-zero magnetic field (B$\neq$0), the $m = \pm 1$ degeneracy is lifted; any two of the three spin ground states can be selected to operate as a qubit.

based state readout is feasible.

Many entanglement protocols take advantage of the spin-optical interface offered by color centers, and entangles spin qubits by interfering emitted photons [21, 25]. The rate of success for these interference-based entanglement schemes depends directly on the in-distinguishability and rate of emission of the transmitted photons. Therefore, from these requirements, the ‘useful’ emission from a color center consists of coherent ZPL photons, whose probability of emission per excitation event is given by the product of quantum efficiency and Debye-Waller factor. Therefore, efficient ZPL photon collection and routing is therefore crucial to the utilization of color center defects as spin qubits for networking purposes. For the NV$-$, although the quantum efficiency is estimated to be near unity ($\sim 0.85 - 1$ [15, 35]), the natural fraction of coherent photon emission is severely limited by its Debye-Waller factor of $\sim$0.03 [36, 37].

Additionally, the NV$^-$, with its permanent dipole moment, is sensitive to nearby electric field fluctuations and the proximity of sample surfaces. Although this property positions the NV$^-$ center as an excellent sensor and magnetometer [26, 27], such sensitivity proves detrimental to to efforts to integrate the NV$^-$ in nanophotonic devices.

Therefore, to tackle these two issues, we would ideally like to search for a color center that has intrinsically a higher proportion of ZPL emission as well as natural resistance towards electric field fluctuations. Thankfully, diamond offers a plethora of other possible defect centers! One of these

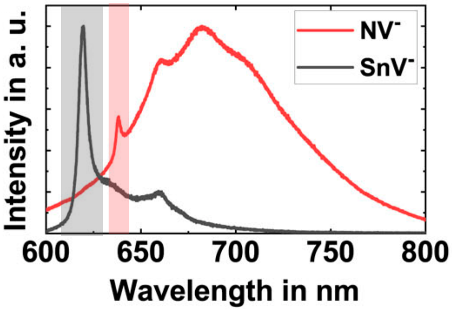

Figure 2.4: Comparison of PL intensity at room temperature between the NV$^-$ and the SnV$^-$. Figure is adapted from [38]. The ZPL for the NV$-$ (SnV$^-$) is indicated by the gray (red) shaded region. As evidenced, the natural ZPL emission rate of the SnV$^-$ is much greater than that of the NV$^-$.

which has recently come to the forefront is a family of color centers referred to as the group-IV centers.

2.1.2 The SnV$^-$ (and SiV$^-$) Center

The negatively charged group-IV color centers in diamond are a family of color centers that all share an atomic structure. Each member of this family consists of dual carbon vacancies with an interstitial group-IV atom (ie. Si, Ge, Sn, Pb). The dual-vacancy structure grants this family of color centers a geometric inversion symmetry and no permanent dipole moment, in contrast to the NV$^-$ (Fig. 2.5). As consequence, a group-IV defect center is, to first-order, insensitive to electric fields and ideal for integration with nanophotonic devices whose fabricated surfaces often have a fluctuating charge environment. Although the most mature of the family is the silicon vacancy center (SiV$^-$) [39, 40, 41, 42, 43], a focus of this thesis will be on third defect center of this family, the negatively charged tin-vacancy center (SnV$^-$), whose properties I will describe in greater detail. As a note, in Chapter 4, experimental demonstrations will be performed with the SiV$^-$, due to material constraints at the time, and therefore relevant characteristics of the SiV$^-$ will be mentioned as well.

The SnV$^-$, compared to the NV$^-$, has a slightly reduced quantum efficiency of $\sim$0.8 [44], but boasts a significantly larger Debye-Waller factor of 0.57 [29]. The SnV$^-$ energy structure, as with all other members of its family, consists of four orbital energy states, with two ground state and two excited states. This characteristic orbital state splitting is caused by a combination of spin-orbit coupling and the Jahn-Teller effect (the spontaneous symmetry-breaking geometric distortion of the defect center) [45], and with the exact frequency splitting differing for each member of the group-IV family. For the SnV$^-$, the energy splitting for the two orbital ground states is $\sim$850 GHz and for the orbital excited states $\sim$3000 GHz [46]. For the Si$^-$ these splittings are $\sim$50 GHz and $\sim$300 GHz,

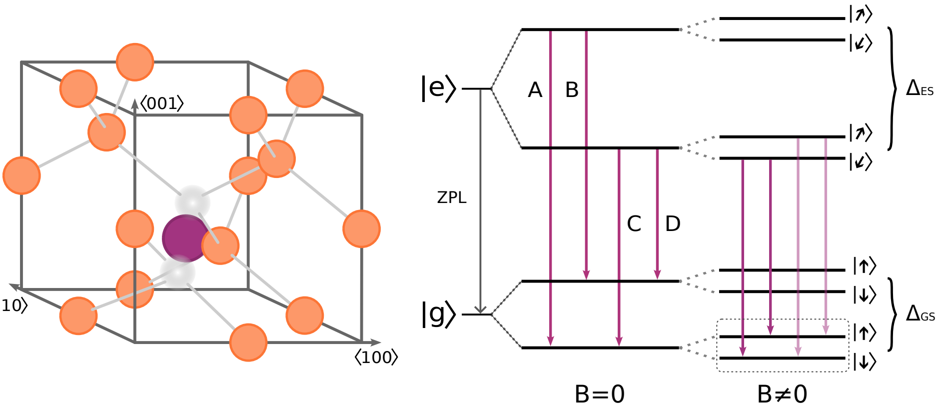

Figure 2.5: Group-IV color center atomic and energy structure.
The color center's atomic structure (left) consists of a dual carbon vacancies (gray) with an interstitial group-IV atom (purple). The orange circles represent carbon atoms. Due to the geometrical symmetry, a group-IV color center possesses no permanent dipole moment, and therefore is first-order insensitive to electric fields. The orbital and spin structure is given at the right. The SnV^- ZPL is $\sim$620 nm and the SiV^- $\sim$737 nm. The combined effects of spin-orbit coupling and the Jahn-Teller effect split both the ground and excited states to yield a characteristic set of four orbital states, labeled from lowest to highest wavelength as A, B, C, and D. For the SnV^-, the ground state splitting (Δ_{GS}) is $\sim$850 GHz and the excited state splitting (Δ_{ES}) is $\sim$3000 GHz; the SiV^- has Δ_{GS} $\sim$50 GHz and Δ_{ES} $\sim$200 GHz. To address the group-IV spin states, a magnetic field is necessary to lift the orbital state spin degeneracies. Either pair of orbital ground spin states can be defined as a spin qubit, but most current demonstrations have addressed the lower subset of states (dashed gray box). Furthermore, a 'lambda' system can be defined between a pair of qubit states and a chosen excited spin-resolved excited state (either the bold or transparent transitions for $B \neq 0$); resonantly driving the predominantly spin-preserving transition of a lambda system would spin-pump the qubit into the opposite spin state.

respectively [47, 45]. In particular, the ground state splitting (Δ_{GS}) of a group-IV color center is of particular importance, as it sets the maximum temperature at which the color center can maintain spin coherence. To understand the importance of this ground state splitting for the group-IV's, we will discuss spin state initialization, readout, and control for the SnV$^-$.

2.1.3 Spin Initialization, Readout, and Control of the SnV$^-$ Center

The SnV$^-$ spin system, similar to that for all other group-IVs, consists of 11 electrons, arranged within orbital states to yield a total spin of s=1/2 for the defect center [45, 48]. Therefore, unlike the NV$^-$ which even at zero magnetic field has addressable spins states (m=0 and m=±1), access to the spin states of the SnV$^-$ requires Zeeman splitting to the lift the m=±1/2 degeneracy of its orbital states [46]. In doing so, the four orbital states each split into two sublevels, for a total of eight addressable spin states. Either pair of spin ground states can be chosen to define a qubit (Fig. 2.5) [49, 50, 51, 52, 53, 54]. Furthermore, as the spin quantization axis differs slightly between the ground and excited state manifolds, one can define a 'lambda' system between a pair of spin qubit states and a chosen excited spin state [49]. From this three-level substructure, one can identify two transitions: the spin-preserving and spin-flipping transitions. This 'lambda' system will enable optical initialization and readout of the SnV$^-$ spin state (Fig. 2.6).

To initialize the spin state, the spin-preserving transition is resonantly addressed. To demonstrate this, we follow the schematic presented in Fig. 2.6(a), which shows two possible 'lambda' systems formed from the spin states resolved from the orbital 'C' transition. If the SnV$^-$ is in spin state $|\downarrow\rangle$, the color center will be resonantly excited to excited spin state $|\swarrow\rangle$ via the transition labeled 'C1'. Otherwise, if the SnV$^-$ is in state $|\uparrow\rangle$, the resonant laser will not address any transition as the rate of Zeeman splitting differs for orbital ground and excited states. Therefore, in this scenario, the color center will remain in state $|\uparrow\rangle$. When the color center is in state $|\swarrow\rangle$, ZPL emissions will predominantly consist of decays along the spin-preserving transition. However, given the slight misalignment of the spin quantization axis for the excited state, there is a slight probability that the electronic spin state will decay instead along the spin-flipping transition.

The probability of a spin-preserving decay to that of a spin-flipping decay is referred to the cyclicity. As studied in [52, 40], cyclicity is controlled through the degree of misalignment between the emitter transition dipole moment and the magnetic field necessary to split spin degenerate orbital states. This ratio is minimized when the two vectors are orthogonal ($\vec{\mu}_{eg} \cdot \vec{B} = 0$), and maximized when they are parallel ($\vec{\mu}_{eg} \cdot \vec{B} = 1$). If the spin-preserving transition is repeatedly addressed, the spin state will eventually be initialized into $|\uparrow\rangle$. The number of excitation attempts required is directly related to the cyclicty: with high cyclicity, the spin-preserving transition needs to be addressed for a large number of repetitions before the spin state flips. In summary, the spin state can be initialized to state $|\uparrow\rangle$ by driving transition 'C1' and, similarly, the state can be initialized in $|\downarrow\rangle$ by driving instead 'C2.' Experimentally, this is accomplished by resonantly driving the spin-preserving

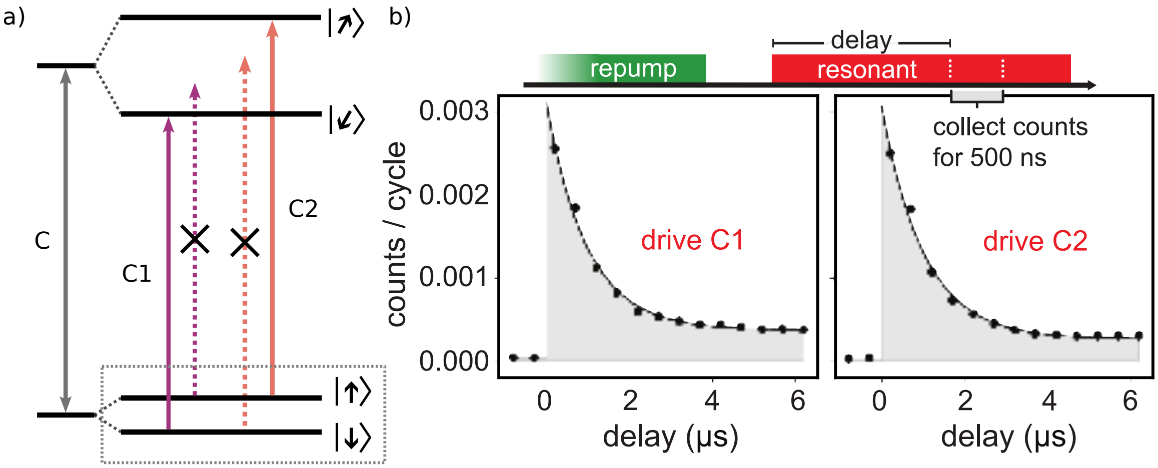

Figure 2.6: Optical spin initialization for the SnV$^-$.
(a) Schematic of lambda systems formed from the orbital C transition. Either lambda system can be utilized to initialize the spin state. For instance, if the qubit is in ground state $|\downarrow\rangle$, driving the spin-preserving transition 'C1' will excite the color center to $|\swarrow\rangle$. The color center can then which then decay, emitting photons; this transition is impossible if the qubit instead starts in $|\uparrow\rangle$ (crossed out transition). During the decay, there exists some low probability of a spin-flip. Therefore, continuously exciting along 'C1' for a sufficient duration will eventually initialize the spin into state $|\uparrow\rangle$. Similarly, the spin state can be initialized to $|\downarrow\rangle$ by driving transition 'C2.' The probability of decay along the spin-preserving transition to that along the spin-flipping transition is referred to as the cyclicity. **(b)** Experimental determination of resonant drive duration required for high fidelity spin state initialization. Figure is adapted from [50]. As the spin-preserving transition is driven for longer durations, the probability of spin-flipping decay increases, leading to an exponential decay in measured fluorescence.

transition for a sufficiently long duration (Fig. 2.6(b)).

The mechanism to optically read out the spin state is identical to initialization. Once again, the spin-preserving transition is probed resonantly. As described above, when the spin is in state $|\downarrow\rangle$ ($|\uparrow\rangle$), the color center will excite then decay, emitting (no) PL photons. Therefore, the spin state of the emitter can be determined by distinguished between 'bright' and 'dark' states. The accuracy, or fidelity, of this readout depends on the Poissonian distribution of photons emitted from each state (Fig. 2.7(a)). Conventionally, this readout fidelity ($\mathcal{F}$) is defined by:

$$\mathcal{F} = 1 - \frac{1}{2}P(\uparrow \mid \downarrow) - \frac{1}{2}P(\downarrow \mid \uparrow) \tag{2.1}$$

where $P(\uparrow \mid \downarrow)$ ($P(\uparrow \mid \downarrow)$) is the probability that spin state initialized in $|\uparrow\rangle$ ($|\downarrow\rangle$) during readout returns (in)sufficient photons that the state is judged to be in the opposite state, $|\downarrow\rangle$ ($|\uparrow\rangle$). The photon count threshold used to differentiate between these states can therefore be chosen to maximize fidelity $\mathcal{F}$, but is constrained by the average photon count number of each distribution (Fig. 2.7(a)).

In experimental realities, the reduction of the average photon count rate for the 'bright' state distribution ($\bar{n}_2$) is dominated by insufficient collection efficiency and photon loss, while imperfect filtering of laser scattering and other background light sources may increase the average rate for the 'dark' state ($\bar{n}_1$). From (Fig. 2.7(b)), we see that, for fixed contrast $\Delta\bar{n} = \bar{n}_2 - \bar{n}_1$, as the background increases, the maximum readout fidelity correspondingly decreases; this trend can be rectified for any $\bar{n}_1$ if $\Delta\bar{n}$ is improved through increased $\bar{n}_2$ (Fig. 2.7(c)).

Having discussed spin state initialization and readout, I now review how to prepare arbitrary spin qubit states for the SnV$^-$. The spin state can be controlled either by manipulating the qubit through a Raman drive scheme [49]—a fully optical scheme which drives the spin-preserving and spin-flipping transitions of a 'lambda' system simultaneously—or by directly applying a microwave drive resonant with the spin qubit transition [50, 51, 52, 53, 54]. Operations applied on the spin state are conventionally referred to as 'gates.' As controlling the qubit state via a Raman drive sets constraints on gate fidelity [49], microwave spin control may prove more scalable and reliable. As a tradeoff, microwave spin control of the SnV$^-$ requires a nuanced understanding of the effects of strain and careful alignment of the applied magnetic field [50, 52].

To control the spin state via a microwave drive, we must first precisely identify the qubit frequency through optically detected magnetic resonance (ODMR). In this measurement, the spin state is initialized, a microwave pulse of variable frequency is applied, and lastly the spin state is read out. The qubit frequency is indicated by the peak location of the resulting Lorezntian lineshape (Fig. 2.8(a)). Sweeping the duration of the microwave pulse at this optimized frequency will coherently rotate the state between $|\downarrow\rangle$ and $|\uparrow\rangle$, driving Rabi oscillations. From these oscillations, we can calibrate the duration of microwave drive necessary to to prepare an equal superposition of qubit states ($\pi/2$ gate) and perform a full spin flip (π gate) (Fig. 2.8(b)). The frequency of Rabi oscillations, and therefore the speed of these gates, improves linearly with applied microwave power (Fig. 2.8(c)).

From this discussion on the SnV$^-$ system, we therefore see that the qubit is encoded and all state manipulations take place within a single branch of the orbital ground state manifold. Therefore, any transition between the two orbital ground states would destroy state coherence. Unfortunately, such population transfers are feasible via phonon-mediated processes [55]. Quoting the treatment presented in [56], the relation between temperature, orbital ground state splitting, and phonon absorption (emission) γ_+ (γ_-) rate is given by:

$$\begin{aligned} \gamma_+ &\propto \Delta_{GS}^3 * \frac{1}{\exp(h\Delta_{GS}/k_B T) - 1} \\ \gamma_- &\propto \Delta_{GS}^3 * (\frac{1}{\exp(h\Delta_{GS}/k_B T) - 1} + 1) \end{aligned} \tag{2.2}$$

where Δ_{GS} is the group-IV ground state splitting, h is Planck's constant, k_B is Boltzmann's constant, and T is the temperature. From analyzing these equations, we identify that the maximum

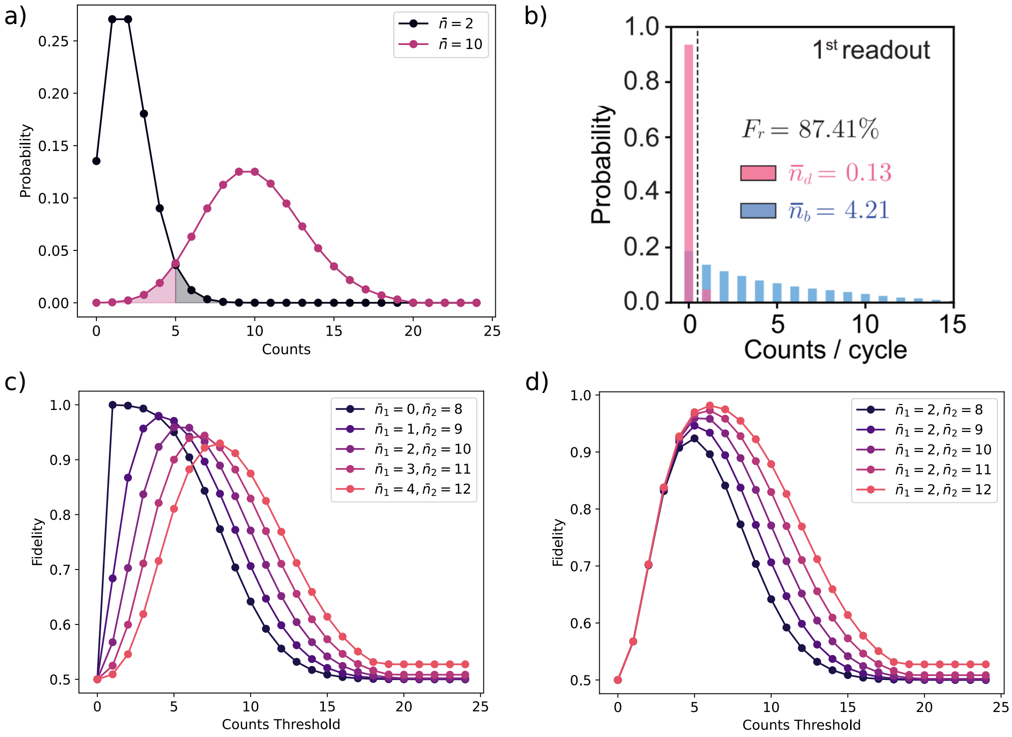

Figure 2.7: Optical spin state readout for the SnV$^-$.
(a) Example of what may constitute the Poissonian probability distributions of ‘dark‘ and ‘bright’ state photon count rates. From these distributions, one can identify the count threshold (N) for which the fidelity metric is maximized; in this case, $N = 5$. The portions of the distributions which contribute to the fidelity error terms are shaded accordingly. **(b)** Experimental demonstration of single-shot spin state readout for the SnV$^-$. Figure is adapted from [52]. Although this experimental demonstration was performed with etched nanopillars to help improve scattering of photons out of plane, the total collection efficiency of the system was remain quite low, estimated to be $\sim 0.2\%$. This low photon collection rate therefore constrained the readout fidelity to 87.41%. Further enhancement to collection efficiency will help improve this metric towards unity by increasing the contrast between ‘dark’ and ‘bright’ states. **(c)** Accessible readout fidelities plotted against various choices of threshold, for varying $\bar{n}_1$ and $\bar{n}_2$. As evidenced, despite constant $\Delta\bar{n} = \bar{n}_2 - \bar{n}_1$, an increasing overall background decreases the maximum possible fidelity value. **(d)** Accessible readout fidelities plotted against various choices of threshold, for increasing $\bar{n}_2$. As the contrast between the two distributions improves, the maximally possible fidelity converges towards unity.

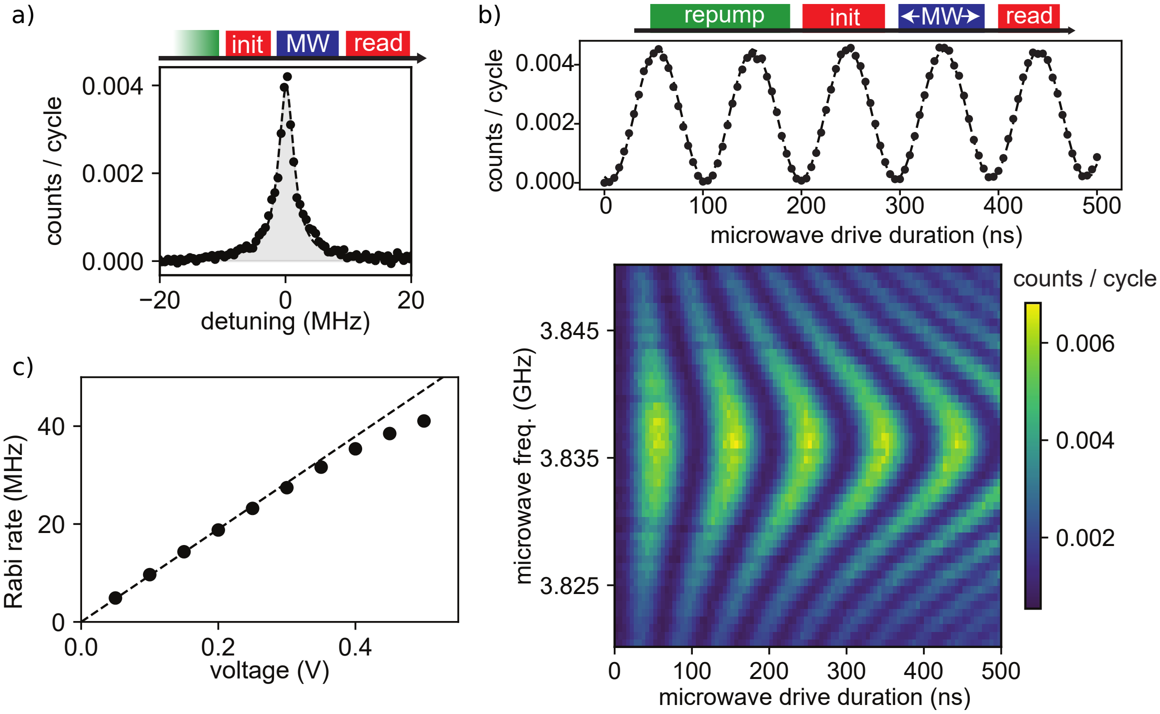

Figure 2.8: Microwave spin control of the SnV$^-$.

Figures are adapted from [50]. **(a)** Example of optically detected magnetic resonance (ODMR) peak. The spin state is first initialized. Then, a microwave pulse of variable frequency is applied, before the spin state is read out. The spin qubit frequency is determined as the center frequency of the resulting Lorentzian lineshape. **(b)** Example of high fidelity Rabi oscillations via microwave spin driving. Rabi oscillations are measured by fixing the microwave drive frequency and sweeping the drive duration. As shown from top sub-panel, there is no visible decay in contrast after many oscillatory cycles, indicating a long qubit coherence lifetime. On the bottom subpanel, a two dimensional sweep of both drive frequency and duration. Characteristically, with increased frequency detuning, the rate of oscillations increase as the contrast diminishes. **(c)** Linear trend of microwave drive power to Rabi oscillation frequency. Faster Rabi oscillations are advantageous for decreasing the length of microwave drive required for spin qubit gates.

temperature at which the SnV− can maintain spin state coherence is ∼1.7 K—roughly the temperature of liquid helium. Although still requiring a chilly environment, the SnV$^-$ does not require the miliKelvin temperatures and dilution refrigerators that both superconducting qubit or its close cousin, the SiV$^-$, require to maintain qubit coherence.

In this section I have discussed the characteristics of the SnV− center in diamond and its suitability as a color center spin qubit both in terms of optical and spin properties. Intrinsically, the SnV− offers a nearly 15-fold improvement in coherent photon (ZPL) emission probability compared to the NV−. Given that spin-state readout relies on thresholding on the number of photons collected when probing a 'bright' versus 'dark' state, increase in total photon emission from a color center would improve spin state readout fidelity. Furthermore, there exists a tension between optimizing cyclicity, thereby maximizing the number of photons emitted during state readout, and elongating the duration of resonant laser excitation required for spin initialization and readout. Not only is the need for long initialization and readout pulse durations detrimental to the duty cycle of the system, extended excitation with a laser can cause additional decoherence to the qubit state [52]. Nanophotonic interfaces can therefore help address these issues both by improving the collection efficiency of emitted photons and increasing the rate of spontaneous emission itself via the Purcell effect.

2.2 Nanophotonic Interfaces

For a SnV$^-$ located roughly 100 nm below the surface of a bulk diamond, only a small fraction of ZPL emission at 620 nm will escape the substrate. This collection efficiency is mainly constrained by the relatively high refractive index of diamond (2.42) at visible wavelengths which causes strong refraction at its dielectric-air interface. By designing photonic structures coupled to the color center, we can therefore boost this photon collection rate via two effects: i) photon channeling into designed optical modes from which photons easily extracted and/or ii) enhancement the spontaneous photon emission rate via the Purcell effect.

2.2.1 SILs and Nanopillars

The first approach towards improving photon collection is to structure the bulk diamond around the SnV$^-$, for instance by etching solid immersion lenses (SILs) or pillars in the bulk diamond [57, 46]. From Lumerical FDTD simulations, we estimate that, from a 620 nm dipole embedded 100 nm below a diamond substrate surface, ∼3% of all emission will be collected. For SILs, as analyzed by [57], one can expect a roughly 3-fold increase in photon extraction. In the case of nanopillars, SnV$^-$ emission can be even more efficiently guided out of bulk, leading to upwards of ∼25% photon collection [58, 52] (Fig. 2.9). SILs and nanopillars therefore represent a reliable method to enhance photon counts from color centers, especially given the simplicity of their design and (relative) ease

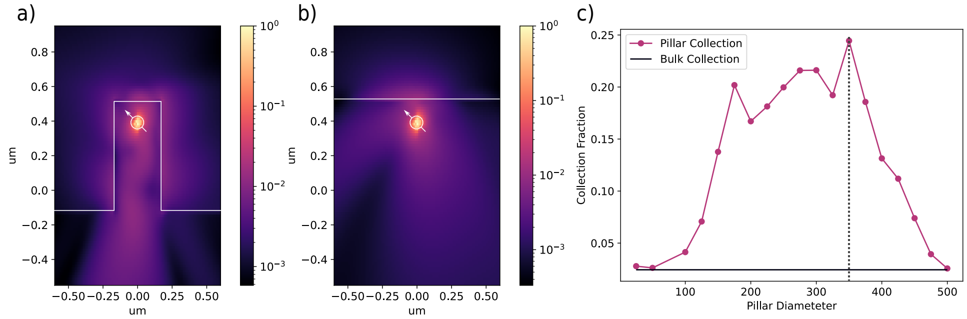

Figure 2.9: FDTD simulations of SnV^- ZPL collection efficiency from a diamond pillar. **(a)** FDTD simulation of out-scattering from a pillar with a diameter of 350 nm and a height of 500 nm. The white outline indicates the location of pillar and of the color center emitter. The colorbar represents normalized electric field intensity. **(b)** FDTD simulation of out-scatting from diamond bulk. The color center is placed 100 nm below the substrate surface (white line), which is the general depth at which our samples are implanted. From the cross-section, one can observe the significant amount of leakage into the bulk below. The colorbar represents normalized electric field intensity. **(c)** Summary of collection efficiencies from a pillars of 500 nm in height and variable diameters. The collection efficiency is calculated through the overlap integral between the pillars' farfield projection and the gaussian mode of the a 0.9 NA objective. We see that at a diameter of 350 nm, a maximum of ∼25 % of color center emission can be collection (grey dashed line). The bold horizontal line indicates the collection efficiency from bulk diamond, as visualized in (b).

of fabrication. However, given that they are still attached to the substrate, SILs and nanopillars will suffer from significant leakage of emission into the bulk below.

To surpass this limitation, one can instead envision separating the color center from the high-refractive index bulk material, such as in an a suspended or 'air-clad' waveguide [59, 60], or by bonding the high refractive index material onto some low index substrate, as is commonly done for mature silicon photonics. In the case of integrating a color center in a suspended waveguide, the dipole emission now couples to guided modes. In probing the color center emitter directly from above, out of plane, simulations yield estimated collection efficiencies up to $\sim 25\%$. Meanwhile, for optimized waveguide dimensions, $\sim 16\%$ are coupled into the TE fundamental mode at each end, for a total of $\sim 32\%$ (Fig. 2.10). Indeed, just by coupling color centers to waveguides, interesting quantum optics and physics can be probed [61, 62]. Furthermore, coupling of color centers to waveguides will be a key component of the discussion in Chapter 4.

However, what is much more exciting is to fundamentally alter the emission behavior of the color center via Purcell enhancement. to do so, we design nanophotonic interfaces in the form of optical resonators or cavities. In fact, by the nature of these interfaces, photon emission will naturally be channeled into a well-defined optical mode, thereby boosting passive photon extraction rates from the system, lending us a two-fold improvement to our quandary.

2.2.2 Cavity Quantum Electrodynamics

Strong Coupling

To understand how a resonator may alter emission properties, I first lay out the formalism of cavity quantum electrodynamics (CQED). The simplest CQED system would consist of an optical resonator, or cavity, coupled to a two-level, atomic system. For the cavity, we consider a single resonant mode which is quantized and represented as a quantum harmonic oscillator with some frequency ω_c. We model the atom as a two-level system with energy levels $|g\rangle$ and $|e\rangle$, separated by a transition of frequency ω_a (Fig. 2.11(a)). As derived through the quantization of the electric field as presented in course material from EE340, Quantum Photonics, the coupling rate g serves as a measure of the cavity-atom coupling strength and takes into account the vacuum Rabi rate g_o, the spatial positioning of the atom in the cavity mode electric field, and the polarization alignment between the atom dipole moment and the cavity mode polarization [63]:

$$\begin{aligned} g_o &= \frac{\mu_{eg}}{\hbar}\sqrt{\frac{\hbar\omega_c}{2\varepsilon_M \mathcal{V}}} \\ g &= 2g_o \frac{E(\vec{r_a})}{|E(\vec{r}_{max})|}(\vec{\epsilon_a}^* \cdot \vec{\epsilon_c}) \end{aligned} \tag{2.3}$$

where in the definition of g_o, μ_{eg} is the atomic transition dipole moment matrix element, $\varepsilon_M = \sqrt{n}$ is the dielectric constant of the cavity medium and $\mathcal{V} = \frac{\int d^3\vec{r}\epsilon(\vec{r})|\vec{E}(\vec{r})|^2}{\max\{\epsilon(\vec{r})|\vec{E}(\vec{r})|^2\}}$ is the cavity mode volume. $E(\vec{r})$ is the cavity mode electric field amplitude, with $\vec{r_a}$ and $\vec{r}_{max}$ being the position of the atom and the the electric field maximum, respectively. Lastly, $\vec{\epsilon_a}^* \cdot \vec{\epsilon_c}$ describes the overlap between the atomic transitions dipole orientation and the cavity mode polarization. More details are presented in Appendix A.1.

To begin, we forego considerations of loss in the system, effectively analyzing the case of strong coupling. Following the conventions from Chapter 3 of [64], we can write following Hamiltonian ($\hat{H}_{JC}$) to describe this model system (post rotating wave approximation, additional details in Appendix A.1):

$$\hat{H}_{JC} = \hbar\omega_c \hat{a^\dagger}\hat{a} + \frac{1}{2}\hbar\omega_a \hat{\sigma_z} + \frac{1}{2}i\hbar g(\hat{a^\dagger}\hat{\sigma_-} - \hat{a}\hat{\sigma_+}) \tag{2.4}$$

where $\hbar$ is the reduced Planck's constant, $\hat{a^\dagger}$ and $\hat{a}$ are the raising and lowering operator for cavity mode, respectively, $\hat{\sigma_+}$ and $\hat{\sigma_-}$ are the atomic raising and lowering operators such that $\hat{\sigma_+} = |e\rangle\langle g|$ and $\hat{\sigma_-} = |g\rangle\langle e|$, and $\hat{\sigma_z}$ is defined as $|e\rangle\langle e| - |g\rangle\langle g|$. From inspection, we can see that the terms $\hat{a}\hat{\sigma_+}$ and $\hat{a^\dagger}\hat{\sigma_-}$ represent the exchange of energy between the cavity and the atom.

Diagonalizing the Hamiltonian in a two state ($|g, n+1\rangle, |e, n\rangle$) sub-basis results in the following two eigenenergies ($E_\pm$) and eignstates ($|+\rangle, |-\rangle$). We also introduce the frequency detuning $\Delta = \omega_a - \omega_c$:

$$\begin{aligned} E_{\pm} &= \hbar\omega_c(n+1) \pm \sqrt{\Delta^2 + g^2(n+1)} \\ |+\rangle &= \cos(\theta/2)\,|e,n\rangle + i\sin(\theta/2)\,|g,n+1\rangle \\ |-\rangle &= \sin(\theta/2)\,|e,n\rangle - i\cos(\theta/2)\,|g,n+1\rangle \end{aligned} \tag{2.5}$$

In this representation, $\sin(\theta/2)$ and $\cos(\theta/2)$ are defined in relation to $\tan(\theta) = g\sqrt{n+1}/\Delta$ (additional details provided in Appendix A.2). These eigenstates are the well-known 'dressed states' of the Jaynes-Cummings Hamiltonian for which the atom and cavity mode become entangled at small Δ; in the time-domain the system therefore exhibits coherent Rabi oscillations between $|e,n\rangle$ and $|g,n+1\rangle$ (Fig. 2.11(b)). However, such a system with no energy dissipation is unrealistic.

Lossy Systems and Purcell Enhancement

To introduce dissipation in this atom-cavity model, I summarize the treatment presented in Chapter 4 from [64]. For all further discussion in this section, we assume that the atom and cavity are perfectly on resonance, such that $\Delta = 0$. We can now write the Lindbladian master equation [1] to take into account loss channels by considering the atom-cavity system to be coupled to a thermal photon bath:

$$\frac{\mathrm{d}\rho}{\mathrm{d}t} = \frac{1}{i\hbar}[\hat{H}_{JC}, \rho] + \sum_i [\hat{\mathcal{L}}_i \rho \hat{\mathcal{L}}_i^\dagger - \frac{1}{2}(\hat{\mathcal{L}}_i^\dagger \hat{\mathcal{L}}_i \rho + \rho \hat{\mathcal{L}}_i^\dagger \hat{\mathcal{L}}_i)] \tag{2.6}$$

where ρ is the density matrix, and $\hat{\mathcal{L}}_i$ are the quantum jump operators, can be defined [2] as follows:

$$\hat{\mathcal{L}}_i = \begin{cases} \sqrt{\Gamma(1+n_{th})}\hat{\sigma_-} \\ \sqrt{\Gamma n_{th}} \\ \sqrt{\kappa(1+n_{th})}\hat{a} \\ \sqrt{\kappa n_{th}}\hat{a^\dagger} \end{cases} \tag{2.7}$$

Γ is the atomic spontaneous emission rate in this system; κ is the cavity mode damping rate, which is directly related to the cavity quality factor (Q) as $\kappa = \omega_c/Q$. n_{th} represents the thermal photon bath. These four operators therefore describe all single thermal photon emission and absorption processes for the atom or cavity. However, in most experimental situations, the systems are cryogenically cooled such that the thermal bath photon population is negligible, such that the approximation $n_{\mathrm{th}} \approx 0$ can be made which reduces the jump operators to:

$$\hat{\mathcal{L}}_i = \begin{cases} \sqrt{\Gamma}\hat{\sigma_-} \\ \sqrt{\kappa}\hat{a} \end{cases} \tag{2.8}$$

---

[1] I've since decided that understanding exactly how the Lindbladian came to be is a lost cause for me.

[2] Or in my opinion, intuited through sporadic bouts of divine inspiration.

Having set up this infrastructure, we can now see that the threshold for strong coupling can be defined in terms of relations between g and Γ, κ. In the case when $g \gg \Gamma, \kappa$, the jump operator contributions in the Lindbladian can be neglected by approximating $\Gamma, \kappa \approx 0$, returning the system's dynamics to the perfectly, eternally coherent Rabi oscillations described in the previous section. More realistically, in the case where the loss is not entirely negligible, the Rabi oscillations gain a damping term. This is seen by constructing a system of rate equations by expanding the Lindbladian in the three state subspace $(|e,0\rangle, |g,1\rangle, |g,0\rangle)$ such that $\rho_1 = |e,0\rangle\langle e,0|$, $\rho_{22} = |g,1\rangle\langle g,1|$, and $\rho_{33} = |g,0\rangle\langle g,0|$. To simplify the system of rate equations, a further assumption is made that the dissipation in the system is mainly dominated by cavity loss, or, the approximation that $\Gamma \approx 0$ holds.

$$\begin{cases} \frac{\mathrm{d}\rho_{11}}{\mathrm{d}t} = -g/2(\rho_{12} + \rho_{21}) \\ \frac{\mathrm{d}\rho_{22}}{\mathrm{d}t} = g/2(\rho_{12} + \rho_{21}) - \kappa\rho_{22} \\ \frac{\mathrm{d}(\rho_{12}+\rho_{21})}{\mathrm{d}t} = g(\rho_{11} - \rho_{22}) - \kappa/2(\rho_{12} + \rho_{21}) \\ \frac{\mathrm{d}\rho_{33}}{\mathrm{d}t} = \kappa\rho_{22} \end{cases} \tag{2.9}$$

This set of rate equations can be solved as an eigensystem with with redefined variables $x = \rho_{11}, y = \rho_{22}, z = \rho_{12} + \rho_{21}$. The eigenvalues of such a system are

$$\lambda = -\kappa/2, -\kappa/2 \pm \kappa/2\sqrt{1 - 4g^2/\kappa^2} \tag{2.10}$$

There emerges a threshold at $g = \kappa/2$, such that when $g > \kappa/2$, the solution for the excited state population takes on an oscillatory form. Therefore, $g > \kappa/2$ defines the strong coupling regime for atom-cavity interactions. On the other hand, when $g < \kappa/2$, the system instead enters the weak coupling regime, where the solution is approximately a single-exponential decay. To the decay lifetime, we make the approximation $g \ll \kappa$, from which the solved eigenvalues from 2.10 can be expanded around $g/\kappa \approx 0$:

$$\begin{gathered} \sqrt{1 - 4g^2/\kappa^2} \approx 1 - 2(g/\kappa)^2 - \mathcal{O}((g/\kappa)^4) \\ \lambda = \begin{cases} -\kappa/2 \\ -\kappa/2 + \kappa/2(1 - 2(g/\kappa)^2) \approx -g^2/\kappa \\ -\kappa/2 - \kappa/2(1 - 2(g/\kappa)^2) \approx -\kappa + g^2/\kappa \approx -\kappa \end{cases} \end{gathered} \tag{2.11}$$

we observe that g^2/κ dominates significantly in terms of time scale. Recasting using the definition of g from equation 2.3, $\kappa = \omega_c/Q$, and $n = \sqrt{\varepsilon_M}$:

$$\Gamma_c = \frac{2d^2}{n^2\hbar}\frac{Q}{\mathcal{V}}\left|\frac{E(\vec{r_a})}{E(\vec{r}_{max})}\right|^2 |\vec{\epsilon_a}^* \cdot \vec{\epsilon_c}|^2 \tag{2.12}$$

The spontaneous emission rate of the atom embedded within a uniform medium of the same refractive index n is given by:

$$\Gamma = n\Gamma_o = \frac{d^2\omega_a^3 n}{3\pi\epsilon_o\hbar c^3} \tag{2.13}$$

for which Γ_o is the spontaneous emission rate of the atom in vacuum, given by Fermi's Golden Rule.

Taking the ratio of 2.12 and 2.13, and converting from frequency to wavelength ($\lambda_c = 2\pi c/\omega_c$), now gives the factor by which the atom's emission rate has been increased via coupling to the cavity mode:

$$F_o = \frac{3n}{4\pi^2}\frac{Q}{\mathcal{V}}\left(\frac{\lambda_c}{n}\right)^3 \left|\frac{E(\vec{r_a})}{E(\vec{r}_{max})}\right|^2 |\vec{\epsilon_a}^* \cdot \vec{\epsilon_c}|^2 \tag{2.14}$$

This value F_o is the Purcell enhancement factor. It is important to note for later discussions that the Purcell enhancement factor is proportional to the ratio $Q/\mathcal{V}$, a value which can be engineered via cavity design. Realistically, it is very unlikely that a cavity will be perfectly on resonance with the atomic transition without tuning. In the case that $\Delta \neq 0$:

$$F = F_o \frac{\delta^2}{\delta^2 + 4(\lambda - \lambda_c)^2} \tag{2.15}$$

where F_o is the Purcell factor defined in 2.14, $\delta = \lambda_c/Q$ is the cavity linewidth, and λ is the frequency of the atomic transition. Lastly, from the Purcell factor, we can define the spontaneous emission coupling factor β, which describes the fraction of spontaneous emission from the atom which is channeled into the cavity mode [63]:

$$\beta \approx \frac{\Gamma_c}{\Gamma_c + \Gamma_o} = \frac{F}{1+F} \tag{2.16}$$

In summary, in this section, I have written out the formalism describing the most simple CQED system, consisting of a two-level atom coupled to a single-mode cavity resonance. Focus is placed on analyzing the dynamics of the system when the atomic transition and cavity mode are on resonance, such that $\Delta = \omega_a - \omega_c \approx 0$. In the strong-coupling regime, when $g > \kappa/2$, the atom and cavity field are entangled and demonstrate coherent Rabi oscillations in the time domain. When $g < \kappa/2$, the system instead enters the weak-coupling regime, where the spontaneous emission rate of the atom is enhanced by the Purcell factor F when the atom and cavity are on resonance. Furthermore, the atomic emission is preferentially channeled into the well-characterized cavity mode, quantified by β, for which highly efficient methods of photon extraction can be designed. In the next section I will describe how to physically implement a CQED system.

2.2.3 Photonic Crystal Cavities

A variety of different cavity types for have been explored to serve as nanophotonic interfaces for diamond color centers. A few of these categories will be reviewed in brief, before attention is turned to photonic crystal cavities.

One category is Fabry-Perot style micro-cavities constructed from two Bragg mirrors; a thin membrane of the color center material is then inserted between the two reflectors [37, 4, 65, 66]. Often, one of the mirrors would be integrated with tip of an optical fiber for ease of photon collection. These cavities provide a straightforward means towards tuning the frequency and position of the cavity through modulation of the cavity length and scanning of the fiber mirror position, respectively; such tunability allows for coupling to target color centers either through spectral or spatial selection. This style of cavities is useful for color centers which need to reside far from any material surface in order to maintain coherence, such as for the NV^-. However, these cavities possess large mode volumes with limited scalability and integration options. Sophisticated techniques are also often necessary for stabilizing vibrations from the flexible fiber input.

In terms of scalability and integration, it is preferable to directly structure the cavity in the color center host dielectric. The simplest fabricated cavity would likely be the disk or ring resonator [67, 68, 69, 70, 71, 72]. These devices confine light via total internal refraction, sustaining 'whispering gallery' modes which propagate around the structure. Devices can either be suspended and fully air-clad, or remain on a sufficiently low refractive index substrate. Evanescent coupling to the disk or ring cavity modes can be achieved via fabricated waveguides or tapered fibers, although generally fabrication defects would cause some small fraction of out-of-plane scattering. However, this variety of resonators are limited in terms of mode volume, given a direct tradeoff between device radius and quality factor. As the device size is reduced, bending loss increases, and the maximally achievable quality factor is lowered [3].

In comparison, photonic crystal cavities, in return for increased complexity in both design and fabrication, can achieve high $Q/\mathcal{V}$ ratios [77, 76, 78, 75, 79, 80]. A photonic crystal is constructed via the periodic modulation of its dielectric constant. As consequence, in analog with solid state semiconductor crystals, the eigenmodes of these devices abide by Bloch's theorem and their dispersion relation or band structure demonstrate ranges of forbidden frequencies, or bandgaps. To show this, following the discussions provided in [73, 81, 63] and in course material from EE340, Quantum Photonics, we can start by invoking the periodicty of the dielectric constant $\varepsilon(\vec{r})$:

$$\varepsilon(\vec{r}) = \varepsilon(\vec{r} + \vec{a}) \tag{2.17}$$

where $\vec{a}$ is referred to as a lattice vector. From this statement of periodicity, the dielectric constant

---

[3] In reality, the $Q/\mathcal{V}$ scaling of these devices favor increased Q even at the concession of $\mathcal{V}$, as Q scales exponentially with ring radius [73]. Techniques such as photoresist reflow can therefore be used to dramatically increase quality factors without too much compromise in mode volume, allowing the system enter the strong-coupling regime [74]. However, I worked really hard on photonic crystals, so please let me talk about them.

can therefore be expressed via Fourier decomposition:

$$\varepsilon(\vec{r}) = \sum_{\vec{G}} \varepsilon_{\vec{G}} e^{i\vec{G}\cdot\vec{r}} \tag{2.18}$$

$\vec{G}$ are the reciprocal lattice vectors, with the relation $\vec{G}\cdot\vec{a} = 2n\pi$ where n is an integer. At this point a number of assumptions are now made regarding the system: the material is assumed to be linear, isotropic, non-dispersive, and transparent in the frequency ranges of interest [73]. From these conditions, we make the assumptions that the material possesses no charge density ($\rho = 0$), no current ($\vec{J} = 0$), and no magnetization ($\mu(\vec{r}) = 0$). This allows for simplification of Maxwell's equations, and the formation of a wave equation for the electric field ($\vec{E}(\vec{r})$):

$$\nabla \times (\nabla \times \vec{E}(\vec{r})) = \omega^2 \varepsilon(\vec{r}) \mu_o \vec{E}(\vec{r}) \tag{2.19}$$

The constructed wave equation can be analyzed as an generalized eigensystem with operators $\hat{\mathcal{O}} = \nabla\times\nabla\times$ and $\varepsilon(\vec{r})$. The periodicity of the system implies a discrete translational symmetry, which can be expressed the translational operator, $\hat{\mathcal{T}}_{m\vec{a}}$ (where m is an integer) which transforms $\vec{r} \to \vec{r} - m\vec{a}$. Applying this operator to equation 2.19, we can determine the following: i) $\hat{\mathcal{T}}_{m\vec{a}}\varepsilon(\vec{r}) = \varepsilon(\vec{r} - m\vec{a}) = \varepsilon(\vec{r})$ and ii) $[\hat{\mathcal{O}}, \hat{\mathcal{T}}_{m\vec{a}}] = 0$, which implies $\mathcal{O}$ and $\hat{\mathcal{T}}_{m\vec{a}}$ share eigenmodes. It proves easier to determine from the characteristics of $\hat{\mathcal{T}}_{m\vec{a}}$ that these shared eigenmodes are plane waves:

$$\begin{aligned} \hat{\mathcal{T}}_{m\vec{a}} e^{i\vec{k}\cdot\vec{r}} &= e^{i\vec{k}\cdot(\vec{r}-m\vec{a})} \\ &= e^{-im\vec{k}\cdot\vec{a}} e^{i\vec{k}\cdot\vec{r}} \end{aligned} \tag{2.20}$$

in which $\vec{k}$ are wavevectors. From 2.20, we also see that the system returns the same eigenvalue under the transformation $\vec{k} \to \vec{k} + \vec{G}$. Therefore, a generalized form of the electric field eigenmode $\vec{\mathcal{E}}_{\vec{k}}(\vec{r})$ can be composed from a linear combination of these degenerate modes:

$$\begin{aligned} \vec{\mathcal{E}}_{\vec{k}}(\vec{r}) &= \sum_{\vec{G}} \vec{A}(\vec{k} - \vec{G}) e^{i(\vec{k}-\vec{G})\cdot\vec{r})} \\ &= e^{i\vec{k}\cdot\vec{r}} \sum_{\vec{G}} \vec{A}(\vec{k} - \vec{G}) e^{-i\vec{G}\cdot\vec{r}} \\ &= e^{i\vec{k}\cdot\vec{r}} \vec{u}_{\vec{k}}(\vec{r}) \end{aligned} \tag{2.21}$$

where $\vec{A}(\vec{k} - \vec{G})$ are expansion coefficients, and $\vec{u}_{\vec{k}}(\vec{r})$ proves periodic such that $\vec{u}_{\vec{k}}(\vec{r}) = \vec{u}_{\vec{k}}(\vec{r} + m\vec{a})$, where m is an integer. Equation 2.21 is therefore a statement of Bloch's theorem. We can now write a Fourier integral for a general electric field composed of the eigenmode expansion coefficients:

$$\vec{E}(\vec{r}) = \int d^3\vec{k}\vec{A}(\vec{k}) e^{-\vec{k}\cdot\vec{r}} \tag{2.22}$$

Substituting equation 2.18 and 2.22 into 2.19 and rearranging yields the following for the dispersion relation[4]:

$$\vec{k} \times (\vec{k} \times \vec{A}(\vec{k})) = \omega^2 \mu_o \sum_{\vec{G}} \varepsilon_{\vec{G}} \vec{A}(\vec{k} - \vec{G}) \tag{2.23}$$

Allowed frequencies ω can be calculated for varying $\vec{k}$ to sketch out the band diagram for a given photonic crystal. If there is modulation of the dielectric constant, solving this equation will yield ranges forbidden frequencies or bandgaps. Analytically solving this 'master' equation quickly becomes intractable, and therefore I at this point would turn to FDTD simulations (Fig. 2.13). In summary, the main takeaway from this saga is that the photonic crystal, by engineering the dielectric modulation and therefore bandgap, can serve as a highly efficient reflector of targeted frequencies.

However, at the point, it is necessary to point out that a perfectly periodic photonic crystal however does not yet serve as a resonator—such a device is converted into a cavity by introducing a defect within its periodicity [5]. In doing so, a confined state is created within the bandgap which now serves as a resonant mode. For the devices of extended discussion in Chapter 3, periodic modulation of the dielectric constant (implemented by etching holes in a thin slab of suspended material) is designed along the propagation direction, therefore only opening a bandgap in the corresponding dimension (Fig. 2.13). The mode is confined in the other two dimensions via total internal fraction at the diamond/air interface. Although the most straightforward and confined defect to introduce would be removing a single etched hole, such a naive approach would lead to reduced quality factors due to large radiative scattering. Therefore, we instead implement a more delocalized perturbation by quadratically tapering the lattice spacing of the center 12 air holes, as informed by the designs reported in [75].

---

[4] I confess I somehow cannot figure out this algebra.

[5] It seems my time here can be summarized in part as coupling the defect in the crystal to the defect in the crystal.

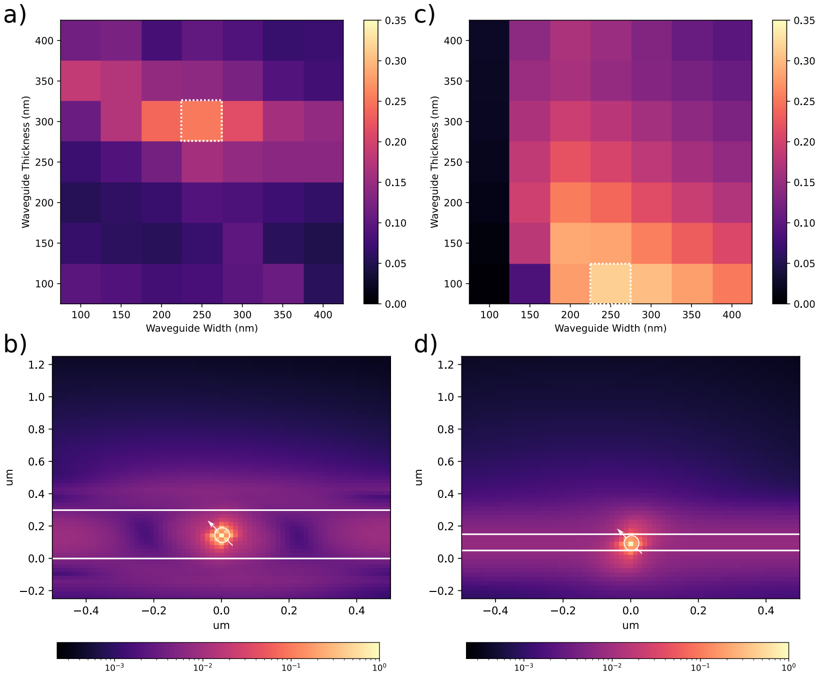

Figure 2.10: FDTD simulations of SnV$^-$ ZPL collection efficiency from diamond waveguides. **(a)** FDTD simulation of out-scattering from diamond waveguides of varying thickness and width. As in the case of pillars, the collection efficiency is calculated through the overlap integral between the farfield projection and the gaussian mode of the a 0.9 NA objective. The dashed box indicates the dimension that resulted in the largest out of plane collection efficiency ∼25%. **(b)** FDTD simulation cross section of the waveguide with the dimensions presented in (a). The white lines indicate the edge of the waveguide. The colorbar represents normalized electric field intensity. **(c)** FDTD simulation of transmission into the fundamental TE mode of the waveguide. The dashed box indicates the waveguide dimensions which yield the highest percentage coupling of dipole emission to the selected waveguide mode ∼35%. **(d)** FDTD simulation cross section of the waveguide with the dimensions presented in (c). As in (b), the white lines indicate the edge of the waveguide and the colorbar represents normalized electric field intensity.

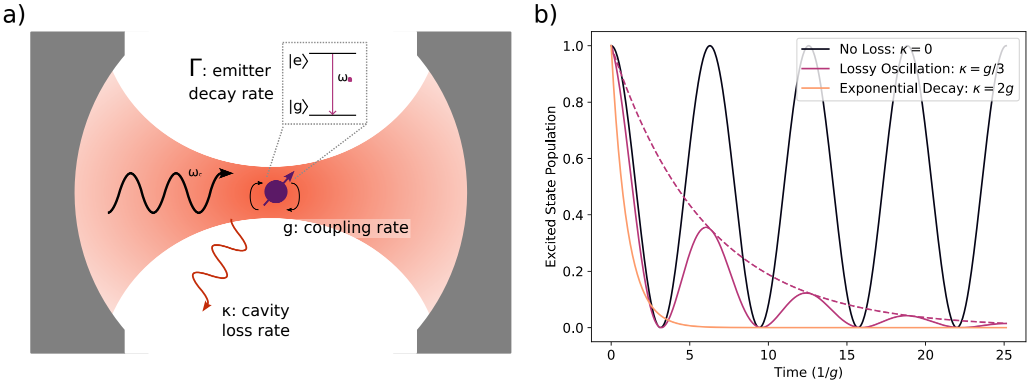

Figure 2.11: CQED schematic and time-domain dynamics.

(a) Schematic of generalized CQED setup, consisting of an two-level atom coupled to a single resonant mode of a cavity. The emitter has a transition frequency ω_c and decay rate Γ. The cavity has some loss rate $\kappa = \omega_c/Q$, where ω_c is the resonance mode frequency and Q is the quality factor of the cavity. The atom and cavity mode is coupled by a coupling rate g. Realistically the emitter is often both spatially and angularly misaligned from the cavity mode intensity maximum and polarization, respectively. **(b)** Atomic excited state ($|e\rangle$) decay dynamics with $\Gamma \approx 0$ and $\Delta = 0$. When the system (unrealistically) contains no loss terms ($\kappa = 0$), the excited state will display Rabi oscillations with frequency $g/4\pi$, exchanging energy with the cavity mode eternally. When $\kappa \neq 0$ and $g > \kappa/2$, the system is in the strong coupling regime and therefore still exhibits coherent Rabi oscillations. However, the oscillations are damped by a rate $\kappa/2$ (dashed purple line). Lastly, in the weak coupling regime, when $g < \kappa/2$, no oscillations are observed, and instead the decay dynamics are dominated by a single exponential decay with rate $\approx g^2/\kappa$. Exact solution forms are written out in Appendix A.3.

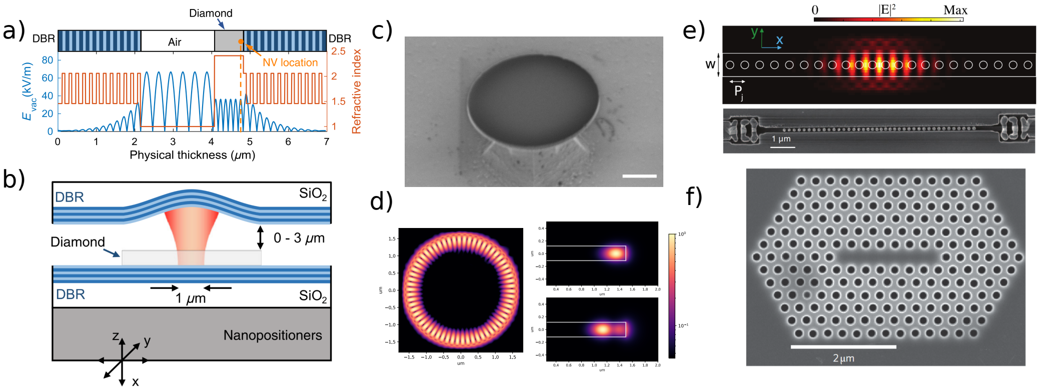

Figure 2.12: Various types of nanophotonic interfaces for diamond color centers. **(a)** Electric field distribution of a Fabry-Perot style microcavity. Figure adapted from [37]. **(b)** Schematic of a Fabry-Perot style microcavity for diamond membranes and color centers. Figure adapted from [37]. **(c)** SEM of diamond disk resonator. The disk was designed to be 3 μm in diameter and ~200 nm. The scale bar is 1 μm. **(d)** Electric field distribution for a resonant mode at ~617 nm supported by a disk with the dimensions in (c). On the left, the electric field distribution of a whispering gallery mode. On the right, examples of guided modes supported by the disk. The top panel is the TE fundamental mode, and the bottom, the second order TE mode. The white lines provide visual indication of the boundaries of the diamond disk. The colorbar is normalized electric field intensity. **(e)** A 1D photonic crystal nanobeam fabricated in diamond. Figure is adapted from [75]. The top panel gives the electric field distribution, and the bottom is an SEM of a fabricated device. **(f)** An example SEM of a 2D photonic crystal cavity. Figure adapted from [76] with permissions. Copyright 2012, Springer Nature.

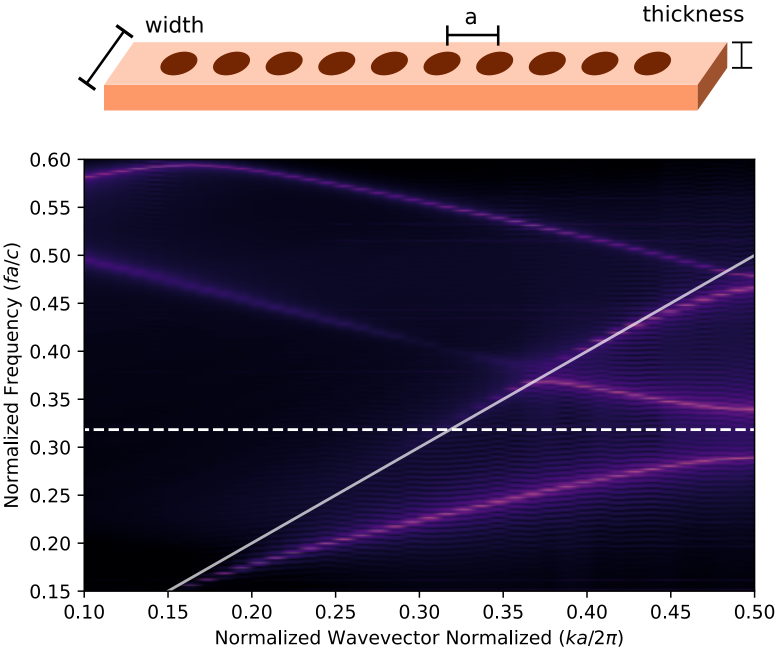

Figure 2.13: 1D photonic crystal example.

a Schematic of 1D photonic crystal. For simulation purposes, the holes are 110 nm in diameter, lattice spacing (a) is 197.5 nm, beam width is 300 nm, and the beam thickness is 180 nm. **b** Example of bandstructure for TE modes in a photonic crystal of the dimensions described in (a), simulated via FDTD. The solid white line indicates the lightline, and therefore all modes above this line are extended, radiative modes. We therefore analyze the guided modes below this light cone. The dashed line corresponds to the normalized frequency for 620 nm and we see that this wavelength resides within the first order bandgap. Therefore, by introducing a defect, we form a isolated mode within this bandgap in order to convert the photonic crystal into a cavity.

Chapter 3

Quantum Nanophotonic Interface for the SnV$^-$ in Thin-Film Diamond

$\mathcal{NB}$: Portions of this chapter are reproduced from the manuscript in preparation, 'Quantum Nanophotonic Interface for Tin-Vacancy Centers in Thin-Film Diamond.'

3.1 Introduction

In this chapter, I will discuss our efforts to implement a nanophotonic interface for the SnV$^-$ via fabricating 1D photonic crystal cavities (1D PCC). As mentioned in the previous chapter, the SnV$^-$ possesses a structural symmetry, which lends it a first-order insensitivity to electric fields. This characteristic positions the SnV$^-$, and the group-IVs in general, as suitable for integration with nanophotonics, as fabricated surfaces often have fluctuating electric charge environments.

Previous reports of 1D PCC's for the SnV$^-$ [75, 79] relied on bulk-carving techniques to suspend devices from the diamond substrate. Theses approaches consist of either angled etching or quasi-isotropic etching [82, 83]. The latter of these two was the focus of my initial efforts, and the process is summarized in Fig. 3.1. However, this fabrication procedure proved rife with failure modes. These include, in order of increasing exasperation:

1. Small (2×2 mm^2, 3×3 mm^2, or 5×5 mm^2) diamond substrates lead to large edge beads and resist non-uniformity. The small size and transparency of the sample also leads to frequent handling errors.

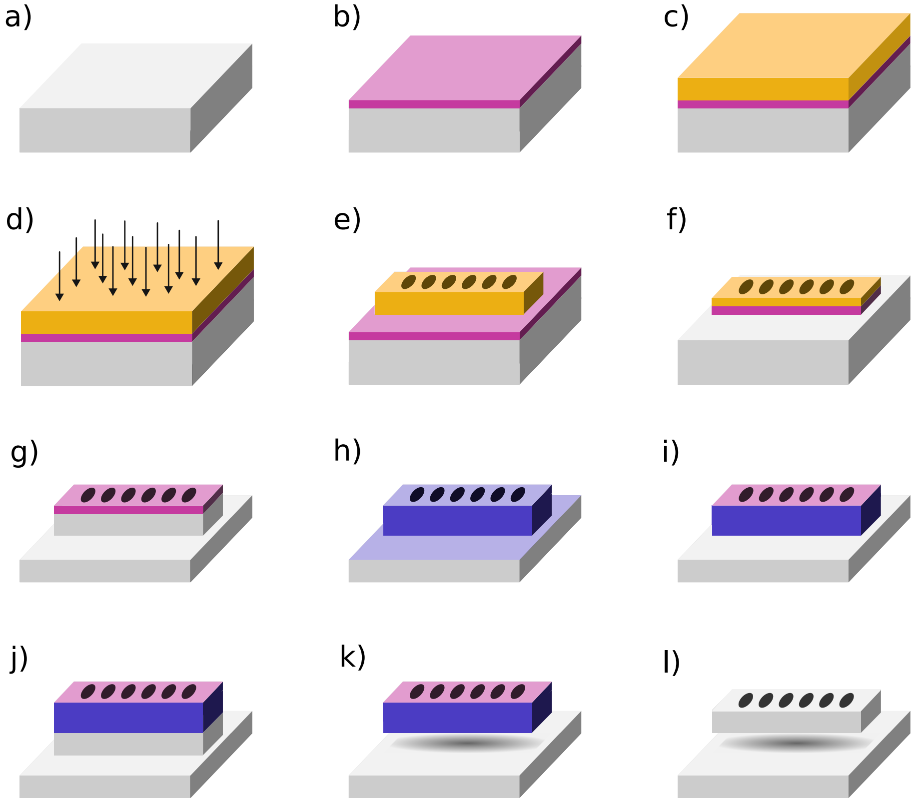

Figure 3.1: The quasi-isotropic undercut fabrication procedure.
The process begins with a a bulk diamond substrate (a). A silicon nitride (Si_xN_y) hard mask is deposited via HDP-CVD (b). ZEP is then spun and a thin charge dissipation layer deposited (eg. 10 nm Al) (c). The pattern exposed via e-beam lithography (d), and the pattern exposed (e). The hard mask is patterned with a ICP-RIE dry etch (f), and then pattern transferred into the diamond substrate with an O_2 chemistry (e). The sample is then conformally coated with a thin layer of Al_2O_3 via ALD (h). The horizontal surfaces are broken through via a ICP anistropic etch (i), and then the pattern further transferred into the diamond substrate to reveal some vertical diamond surfaces (j). The devices are then suspended via the quasi-isotropic undercut, where the sample is etched via a dense O_2 plasma with no RF bias voltage (k). Lastly, the mask layers are stripped via a HF soak (l).

2. Bulk diamond charges up in e-beam lithography without the deposition of metal charge dissipation layers.

3. The process is highly sensitive to sidewall etch angles as the Al_3O_2 sidewall protection 'veil' requires near-perfect sidewall verticality to not detach.

4. Timing for the quasi-isotropic undercut relies on visual inspection and is therefore highly dependent on SEM imaging quality.

5. The quasi-iso undercut etch is dependent on feature size (smaller features etch slower). For a device with varying feature sizes, such as a 1D PCC or grating coupler, the final devices may end up with uneven thicknesses.

6. Stripping the final masking layers requires wet processing. Without proper care, this final procedure may break a sizable portion of the suspended devices, greatly decreasing device yield.

Furthermore, the suspended geometry of the bulk-carved diamond devices limits the varieties on on-chip integration that are feasible. Grating couplers, mode splitters, and other photonic components must be continuous in structure and limited in size, which requires careful design to retain efficiency and performance [84]; electric control lines may end up at a different height from fabricated devices and therefore apply a weaker electric field at the color center position [85, 86]. Additionally, the previous sample studied struggled with color center coherence, potentially due to the combined effects of high dosage ion implantation, insufficient annealing temperatures, and less thorough sample cleaning procedures [75].

To address these issues, diamond thin-film membranes with high quality SnV$^-$ centers have been developed in recent years [87, 72, 88]. In collaboration with Ania Jayich's group at the University of California, Santa Barbara, we have migrated to a thin-film diamond platform, which consists of diamond membranes bonded to sacrificial HSQ and Si. By doing so, we have improved fabrication reliability and yield. Although the membranes themselves are small in size ($200 \times 200\ \mu m^2$), the Si substrate chip can be any dimension, which reduces the possibility of handling errors. The Si bulk also aids in charge dissipation, improving e-beam lithography fidelity. Even though perfectly vertical sidewalls would yield the highest performance, devices still function even with moderate (∼5-10 degrees) sidewall angles. The bonded diamond membrane thicknesses can be tuned before device fabrication, allowing for excellent control of final thicknesses and uniformity. Lastly, no wet processing of suspended structures is necessary: devices can be suspended via well-characterized HF and Xe_2F vapor dry etches, and the top hard mask can be stripped via RIE dry etching at the end of the fabrication procedures.

In this section, we report the fabrication of 1D photonic crystal cavity nanobeams with quality factors of up to ∼6000. In particular, we fabricated two orientations of cavity devices, one parallel to

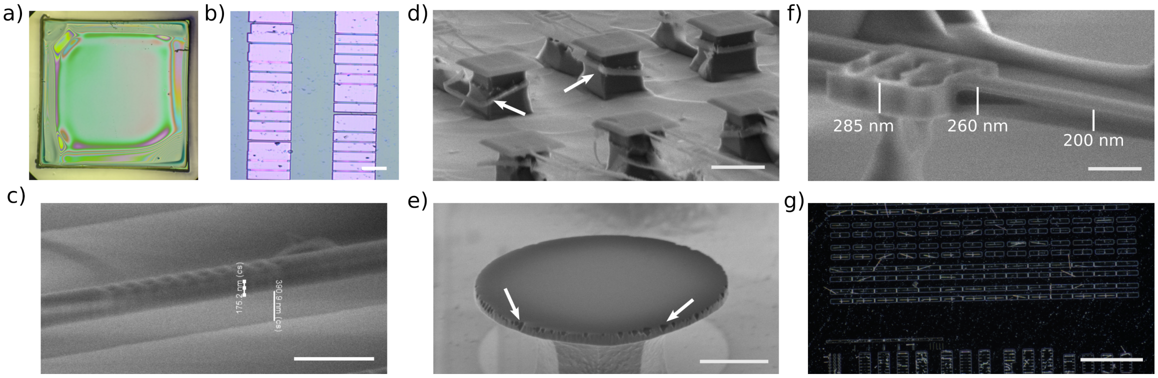

Figure 3.2: Quasi-isotropic undercut failure modes.

(a) White light microscope image of resist spin on a 5 × 5 mm^2 diamond substrate. Given the small sample size, sizable edge beads reduce the amount of usable space on the sample. **(b)** White light microscope image, example of effects of bulk diamond sample charging in e-beam lithography. From the developed resist, we see that write features are distorted and misaligned. The scale bar indicates 10 μm. **(c)** SEM example of in-progress quasi-isotropic undercut. In order to monitor etch progress, the diamond layer thickness is imaged through the thin $\mathrm{Al_3O_2}$ sidewall layer. However, this process relies on visual inspection and is highly dependent on SEM imaging quality. The scale bar represents 1 μm. **(d)** SEM of detached $\mathrm{Al_3O_2}$ sidewall protection 'veils'. The arrows indicate these veils, which had detached from the device sidewalls. In this SEM, as the $\mathrm{Al_3O_2}$ had fully detached, the quasi-isotropic undercut had etched all diamond, leaving only the features defined in the $\mathrm{Si}_x\mathrm{N}_y$ hardmask. The scale bar represents 2 mum. **(e)** SEM of completed disk resonator with arrows to point out some small notches in the top edge of the device. These features stem from partial $\mathrm{Al_3O_2}$ detachment, such that the O_2 plasma etches bits of the diamond from any gaps that emerge. The scalebar indicates 1 μm. **(f)** SEM of completed grating coupling, demonstrating unevenness in device thickness. As the plasma etches differently sized features at different rates, devices such as grating couplers or 1D PCCs, which have complicated structures, often result in uneven thicknesses and reduced performance. The scalebar represents 500 nm. **(g)** Dark field microscope image illustrating the carnage post wet-processing on suspended devices. The scalebar represents 100 μm.

and one at $\sim 55^{\circ}$ to the $\langle 100\rangle$ axis of the diamond lattice. We measure, for each cavity orientation ('parallel' and 'angled') the lifetime reduction of two zero phonon line (ZPL) transitions (C and D) for a SnV- color center. These transitions have the same spatial positioning in the cavity field, but orthogonally polarized dipole moments. The ratio of the C to D transition emission rates is referred to as the branching ratio [46, 61, 48]. The conventional figure of merit for color center-cavity coupling is the Purcell factor, defined as the enhancement in spontaneous emission rate for a particular transition when on resonance with the cavity mode. In previous reports, Purcell factors were calculated via applying lump-sum correction factors to the measured lifetime reduction ratio without consideration of the individual transitions [75, 79]. To determine our Purcell factors with a more rigorous treatment, we construct a model to describe the spontaneous emission dynamics of our system which takes both C/D transitions into account. From this model, we analytically determine the C/D transition branching ratio to be $\eta_{\mathrm{BR}} = 0.7815$, in agreement with previous reports [46, 61, 48]. Ultimately, we report the highest Purcell factor observed for this set of measurements to be $F_C = 26.21 \pm 0.01$ for the C transition in the angled device, for which the cavity mode and dipole emission are best aligned out of the available dipole-cavity orientation combinations. Indeed, our analysis highlights that aligning the photonic crystal cavity at 45° from the diamond $\langle 100\rangle$ crystal axis would result in the highest possible improvement in Purcell factor (∼40%) for either the C or D transition of a coupled SnV^{-} center. These results constitute crucial progress towards the implementation of scalable quantum networks based on the SnV^{-}.

3.2 Results

3.2.1 Device Design and Fabrication

Thin film diamond was prepared via the procedures outlined in [88]. Sn^{2+} was implanted into the bulk sample prior to membrane exfoliation with an implantation energy of 380 keV and at a dose of 2×10^{11} ions/cm^{2}, targeting SnV^{-} formation ∼90 nm below the surface. Final membrane thicknesses were tuned to 180 nm by reactive ion etching.

Photonic crystal cavities were designed with a 300 nm beam width and 115 nm diameter holes etched into the diamond film. The mirror reflectors consist of 10 holes on each side, while the central cavity consists of 12 holes, with quadratically tapered lattice spacings. In order to account for fabrication infidelities and ensure resonances in proximity of the SnV^{-} 619 nm ZPL wavelength, we sweep the lattice spacings from 180 nm to 210 nm in steps of 2.5 nm per device.

For the cavities reported in this manuscript, we measure a post-fabrication beam width of 326 ± 13 nm, average hole diameter of 134 ± 3 nm, and lattice constant of 210 nm for the parallel device; and a beam width of 325 ± 2 nm, average hole diameter of 119 ± 4 nm, and lattice constant of 197.5 nm for the angled device, determined via SEM (Fig. 3.3(b)). We note that our etch recipe renders a $\sim 5-10^{\circ}$ sidewall angle. Taking these dimensions into account, we simulate quality factors (Q) of

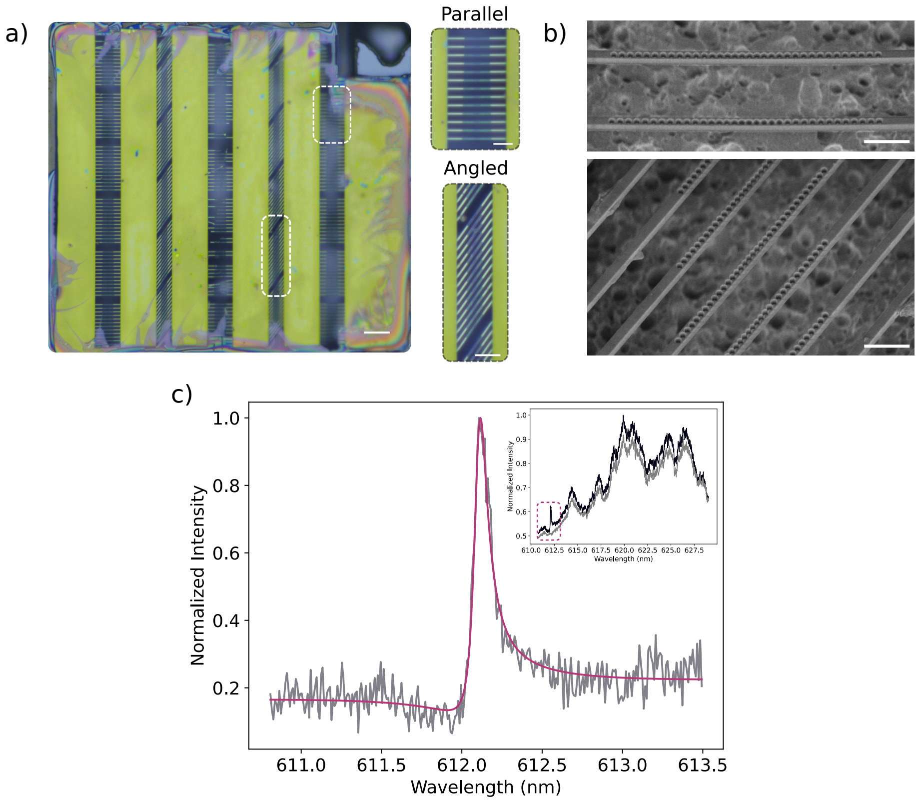

Figure 3.3: Cavity design, fabrication, and characterization.
(a) A white light image of the fabricated devices on the thin film membrane. Representations of the two classes of devices, parallel and angled, are indicated by the white dashed boxes and zoomed to be shown in greater detail. The scale bars indicate 15 μm and 5 μm for the zoomed out and in images, respectively. **(b)** SEM of fabricated devices. Scale bars indicate 1μm. **(c)** The cross polarized reflectivity spectrum for the parallel device. The broadband spectrum is background corrected, then fit to a Fano model, yielding a quality factor of 6032. The inset shows the broadband reflectivity spectra for both the resonance and background. The fitted region is indicated by the dashed box.

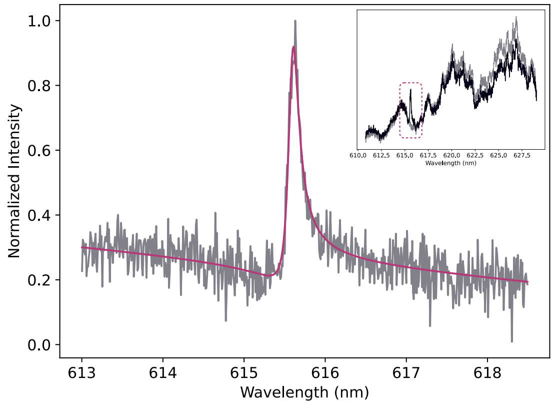

Figure 3.4: Angled cavity quality factor characterization.
The full broadband reflectivity spectra for the resonance and background are shown in the inset. The fitted region is indicated by the dashed line. As with the parallel device, the resonance is fit to a Fano model.

2.8×10^5 (2.3×10^4) and mode volume (V) 0.46 (0.46) $(\frac{\lambda}{n})^3$ for the parallel (angled) device. Further discussion of device design and fabrication yield is provided in Appendix B.1.3.

Additional thin film and device fabrication details are provided in Appendix B.1.1 and B.1.2. In order to optimize space usage of the limited diamond film, transmission access for photonic crystals was forgone and instead all devices were probed out of plane.

3.2.2 Characterization of Devices and Color Centers

Our sample is maintained at 4 K in a Montana Instruments closed cycle cryostat. We utilize two discrete optical paths, subsequently referred to as the i) 'cross-polarized' and ii) photoluminescence ('PL') paths. The two optical paths enable independent access to the cavity resonance and color center signals. The optical setup is described in greater detail in Appendix B.2. We start by probing our cavity resonances using the cross-polarized reflectivity path. The cavities are mounted such that the resonance modes for parallel devices are primarily vertically polarized (the fundamental mode polarization is orthogonal to the cavity axis). Devices are excited via a horizontally polarized, broadband supercontinuum laser, and the vertically polarized, reflected signal is collected by a spectrometer. A half-wave plate (HWP) inserted in the shared excitation and collection path is used to optimize the SNR of the reflected cavity signal, as different HWP settings are required for parallel versus angled devices. Each broadband reflectivity spectrum is background-corrected and then fit to a Fano model. For the parallel device, we determine a quality factor of 6032 (Fig. 3.3(c)). The angled device yielded a quality factor of 3942, determined through a Fano fit of a background corrected broadband spectrum (Fig. 3.4).

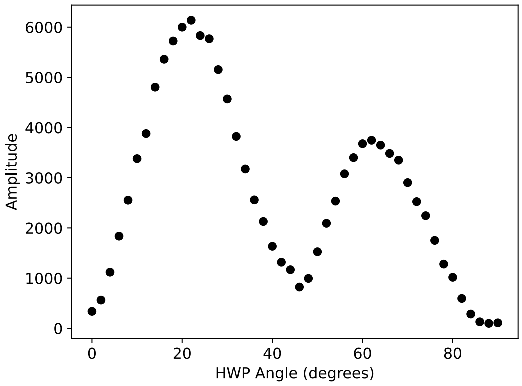

Figure 3.5: Angular dependence of cavity reflectivity amplitude.
The periodicity of the oscillatory behavior is ∼45°, indicating a linearly polarized mode.

To verify that the nanobeam cavity modes are linearly polarized, we measure the angular dependence of the reflectivity amplitude by rotating the HWP. The angular dependence demonstrates sinusoidal behavior with a periodicity of ∼45°, indicating a linearly polarized mode (Fig. 3.5 [89, 90]. The amplitude modulation of the sinusoidal trend is likely due to slight shifts in beam positioning introduced by HWP rotation.

PL enhancement

Next, we perform photoluminescence (PL) spectroscopy to identify emitters located in the cavity mode, exciting with ∼5 mW of a 520 nm CW source and filtering collected counts with a 620/14 nm bandpass filter (Fig. 3.6(b)). Due to the high implantation density, approximately 2-3 emitters lie within our cavity mode. To probe for emitter-cavity coupling, we first red-shift the cavity resonance past the identified SnV$^-$ transitions via argon gas condensation. Then, we 'back-tune' the resonance controllably by illuminating the nanobeam with ∼0.75 mW of green excitation power to evaporate condensed gmas, while simultaneously collecting PL spectra to characterize SnV$^-$ PL enhancement (Fig. 3.6(c)). For the parallel device, we identify a ∼10-fold PL enhancement of the emitter when the cavity is tuned into resonance with the transition (Fig. 3.6(d)). This measure of PL enhancement indicates significant emitter-cavity coupling, but does not suffice as an accurate measure of the Purcell factor given uncertainties in exact collection efficiencies.

In Fig. 3.7, we also present the PL confocal scan of the angled device of interest. Similar to with the parallel cavity, the high implantation dose resulted in a cluster of 2-3 emitters coupled to the cavity mode. The most strongly enhanced transitions demonstrates a ∼2.25-fold PL enhancement when on resonance with the cavity (Fig. 3.7).

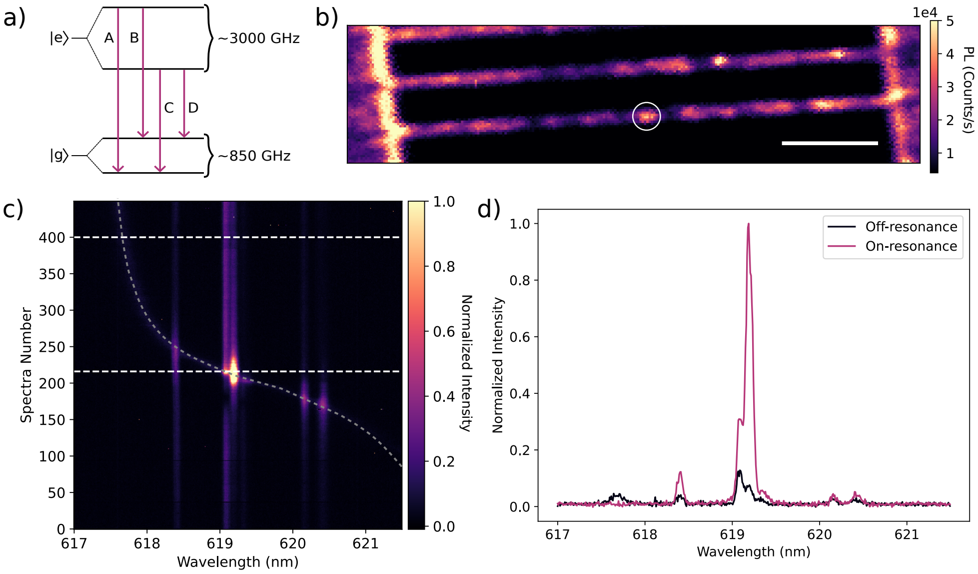

Figure 3.6: SnV$^-$ level structure, PL confocal scan and cavity enhancement. **(a)** Schematic of the orbital energy states of the SnV$^-$. Characteristic of a group-IV color center, the ground ($|g\rangle$) and exited state ($|e\rangle$) are split via the combined effects of spin-orbit coupling and the Jahn-Teller effect. For the SnV$^-$ the ground state splitting is ~850 GHz, and the excited state splitting ~3000 GHz; these state splittings yield four separate ZPL transitions. In cryogenic conditions, PL signal is dominated by the two longer wavelength, lower energy transitions, labeled as C and D [29]. **(b)** PL confocal scan of the parallel device. The emitter cluster addressed is indicated by the white circle. The scale bar indicates 3μm. **(c)** PL enhancement via gas tuning. The cavity resonance is first red-shifted via Ar gas condensation past all SnV$^-$ transitions of interest. The sample is then naturally 'back-tuned' over the course of repeated PL scans. The two spectra of interest are indicated by the white dashed lines. The gray dashed line is an approximate guide for the eye of the cavity resonance. **(d)** PL spectra on and off resonance with the cavity. We see that the most strongly enhanced SnV$^-$ transition demonstrates a ~10-fold PL enhancement.

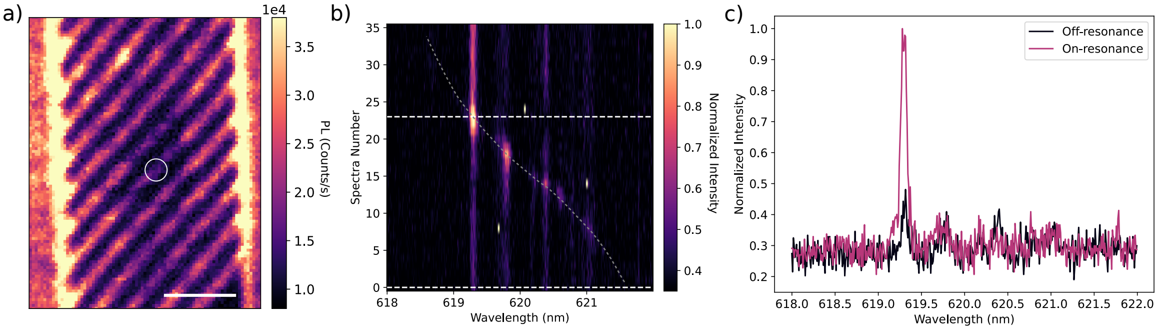

Figure 3.7: Angled cavity PL confocal scan and cavity enhancement.
(a) PL confocal scan of the angled device studied in this manuscript. The emitter cluster of focus is indicated by the white circle. The scale bar indicates 3μm. **(b)** PL enhancement of the SnV^{-}s located in the angled device cavity mode. The spectra for the transition of interest on and off resonance are indicated by the white dahsed lines. The grey dashed line is a guide for the eye of the cavity resonance wavelength. **(c)** PL spectra of the two spectra of interest. From comparing the transition amplitude on and off resonance, we estimate a 2.5-fold PL enhancement from gas tuning.

Lifetime reduction measurement and calculation

To quantify Purcell factors, we measure the lifetime reduction of the emitter when the cavity is tuned into resonance. As before, we red-detune the cavity resonance beyond the SnV^{-} transition in preparation for a back-tuning sweep across the target wavelength. However, we now toggle our excitation between the cross polarized path, used to both monitor and back-tune the resonance wavelength, and the PL path, used to measure the emitter optical lifetime. In the PL path, we isolate a single transition with a narrow band ($\sim$0.3 nm) tunable filter, and excite the emitter above band with a 520 nm pulsed laser. We apply excitation pulses with 16 ns pulse widths, a 3.3 MHz repetition rate and an averaged power of 270 μW. In the cross polarized path, we excite simultaneously with both the supercontinuum and CW green diode laser (set again to $\sim$0.75 mW) in order to both monitor and backtune the cavity resonance. Each lifetime trace is integrated for 3 minutes to build up suitable count rates, while each cross-polarized resonance spectrum is integrated for 3 seconds to allow ample time for the cavity resonance to gradually back-tune across the transition.

We target selective collection from the C transition, but due to collective emission dynamics, we see significant lifetime reduction when the cavity is on resonance with either the C or D transition individually. Furthermore, we will show in Section 3.2.2 that by considering the orthogonality of the C and D dipoles, we can extract the C/D branching ratio and individual Purcell factors for each transition. In preparation for this analysis, we calculate the spontaneous emission rate from the measured emitter decay lifetime via $\Gamma = 1/\tau_{\text{lifetime}}$. When resonant with the cavity, transition C(D) demonstrates a lifetime of 1.847 ± 0.002 ns, or emission rate 0.543 1/ns (4.570 ± 0.02 ns, or emission rate 0.219 1/ns) compared to the off-resonance lifetime of 9.412 ± 0.09 ns, or emission rate 0.106 1/ns

(Fig. 3.8(c)). We then fit the data to a double Lorentzian model. Dividing the fitted Lorentzian amplitude to the background yields a the emission rate enhancement ratio, which we denote as ζ. For the C and D transitions, we extract $\zeta_C = 4.672$ and $\zeta_D = 1.985$, respectively (Fig. 3.8(a)).

For the angled device, there remain contributions from a secondary emitter in the collected counts. We therefore fit the spontaneous emission rates to a quadruple Lorentzian model. We determine that transition C(D) demonstrates a lifetime of 1.079 ± 0.002 ns , or emission rate 0.926 1/ns (8.109 ± 0.2 ns, or emission rate 0.123 1/ns) compared to the off-resonance lifetime of 10.507 ± 0.2 ns, or emission rate 0.095 1/ns (Fig. 3.8(d)). The fitted amplitude ratios are $\zeta_C = 12.230$ and $\zeta_D = 1.514$ (Fig. 3.8(b)).

Purcell factor analysis

From lifetime reduction measurements of the C and D transitions when each is resonant with the cavity, one can extract both the branching ratio and the respective Purcell factors associated with each transition. We further substantiate these analyses by comparing the interactions of emitters coupled to the parallel and angled devices and illustrate how our measured values are consistent with the known angular offsets of the emitter and the designed devices with respect to the crystallographic lattice.

We express the spontaneous emission dynamics of the full cavity-emitter system with the following expressions for spontaneous emission rates:

$$\Gamma_0 = \Gamma_C + \Gamma_D + \gamma_{\text{PSB}} \tag{3.1}$$

$$\Gamma_{\text{coupled}} = F_C * \Gamma_C + F_D * \Gamma_D + \gamma_{\text{PSB}}, \tag{3.2}$$

where Γ_0 is the uncoupled or bulk emission rate, and Γ_{coupled} is the cavity-coupled enhanced spontaneous emission rate. In our analysis, we neglect contributions from the A/B ZPL transitions of the SnV$^-$, as the two higher energy transitions are suppressed in cryogenic conditions [44]. Therefore, in the uncoupled case, the total spontaneous emission rate is given by the sum of Γ_C, the C transition emission rate, Γ_D, the D transition emission rate, and γ_{PSB}, the rate of emission into the phonon side band (PSB). In the cavity-coupled case, F_C and F_D represent the Purcell factor that enhances the emission into the two orthogonal ZPL transitions. F_C and F_D can also be expressed as $F_C = F\cos(\theta)$ and $F_D = F\sin(\theta)$, respectively, to take into account the orthogonal polarizations of the C and D transitions. F is comprised of all shared factors which determine the Purcell factor for the two transitions, including Q/V ratio and emitter spatial position. θ represents the angular offset between the emitter transition dipole and the cavity mode polarization (Fig. 3.8(e)). We can also express θ in terms of ϕ, the global angular offset of the fabricated pattern with respect to the $\langle 100\rangle$ crystal axis. Therefore we can write for the parallel cavity $\theta = 45 - \phi$, and for the angled

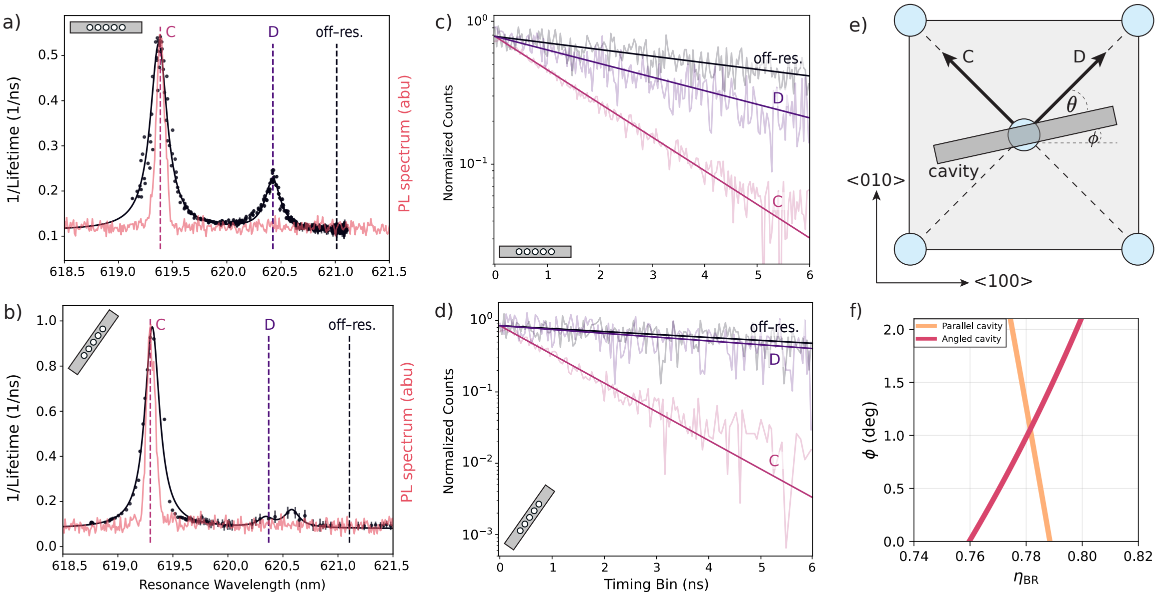

Figure 3.8: Lifetime reduction and branching ratio analysis.
(a) Spontaneous emission rate vs cavity resonance wavelength for the parallel device (black). The data are fit to a double Lorentzian model. The PL spectrum (red) is overlayed. We extract from this fit model the amplitude ratios $\zeta_C = 4.672$ and $\zeta_D = 1.985$. The three vertical dashed lines indicate the lifetime slices that are plotted separately, representing the traces with the C transition on resonance (pink), D transition on resonance (purple), and both transitions off resonance (black). **(b)** Spontaneous emission rate vs cavity resonance wavelength for the angled device (black). As in (a), the PL spectrum (red) is overlayed. For this device, we extract from this fit model the amplitude ratios $\zeta_C = 12.230$ and $\zeta_D = 1.514$. We note that due to filtering limitations, there are contributions from two separate emitters, and the data are thus fit to a quadruple Lorentzian model. The dashed lines indicate the lifetime slices of interest, as in panel (a). **(c)** Normalized lifetimes of the SnV^{-} with C/D transitions on and off resonance for the parallel device. We measure an off-resonance lifetime of 9.412 ± 0.09 ns. When the C(D) transition is on-resonance with the cavity, the lifetime is reduced to 1.847 ± 0.002 ns (4.570 ± 0.02 ns). The lifetimes are fit to amplitude normalized and background corrected single exponential models. **(d)** Normalized lifetimes of the SnV^{-} with C/D transitions on and off resonance for the angled device. We measure an off-resonance lifetime of 10.507 ± 0.2 ns. When the C(D) transition is on-resonance, the lifetime is reduced to 1.079 ± 0.002 ns (8.109 ± 0.2 ns). The lifetimes are fit to amplitude normalized and background corrected single exponential models. We note that due to the contributions of a second emitter transition, at longer timescales, the data begins to deviate slightly from a single exponential mode. However, within the fitting range, the observed fluorescence lifetime is primarily dominated by a single decay timescale. **(e)** Schematic description of the cavity orientation with respect to the lattice sites and dipole moments of the C and D transitions. θ represents the angle between one of the dipoles and the cavity mode, and ϕ represents the collective fabrication angular offset from the diamond $\langle 100 \rangle$ lattice axis. **(f)** Solution of the analysis in Section 3.2.2, resulting in a branching ratio η_{BR} of 0.7815 and fabrication offset ϕ of 1.1 ± 0.1 degrees.

cavity $\theta = 45 - (55 + \phi)$.

Dividing Γ_{coupled} by Γ_0 to analyze the emission enhancement ratios, we write:

$$\begin{aligned} \zeta = \frac{\Gamma_{\text{coupled}}}{\Gamma_0} &= F_C * \frac{\Gamma_C}{\Gamma_0} + F_D * \frac{\Gamma_D}{\Gamma_0} + \frac{\gamma_{\text{PSB}}}{\Gamma_0} \\ &= F_C * \eta_{\text{DW}}\eta_{\text{BR}} \\ &+ F_D * \eta_{\text{DW}}(1 - \eta_{\text{BR}}) + (1 - \eta_{\text{DW}}) \end{aligned} \tag{3.3}$$

where $\eta_{\text{DW}} = 0.57$ is the Debye-Waller factor, or coherent ZPL proportion of total radiative emission [29]. η_{BR} is the branching ratio between transitions C and D. We are able to write two separate ratios, ζ_C and ζ_D, for when the cavity is on resonance with transition C and D, respectively. For ratio ζ_C (ζ_D), we can set F_D (F_C) equal to 1.

We now recast these equations to solve for the Purcell factors:

$$F_C = F\cos(\theta) = \frac{\zeta_C + \eta_{\text{DW}}\eta_{\text{BR}} - 1}{\eta_{\text{DW}}\eta_{\text{BR}}} \tag{3.4}$$

$$F_D = F\sin(\theta) = \frac{\zeta_D + \eta_{\text{DW}}(1 - \eta_{\text{BR}}) - 1}{\eta_{\text{DW}}(1 - \eta_{\text{BR}})} \tag{3.5}$$

By taking the ratio of F_D to F_C, we can now write an equation for θ:

$$\tan(\theta) = \frac{\zeta_D + \eta_{\text{DW}}(1 - \eta_{\text{BR}}) - 1}{\zeta_C + \eta_{\text{DW}}\eta_{\text{BR}} - 1} * \frac{\eta_{\text{BR}}}{1 - \eta_{\text{BR}}} \tag{3.6}$$

Using Eq. 3.6 with ζ_C and ζ_D determined from lifetime measurements, we vary η_{BR} and plot the resulting ϕ for both the parallel and angled cavity cases (Fig. 3.8(f)). By identifying the intersection between the two functions, we solve for $\phi = 1.1 \pm 0.1$, and the branching ratio $\eta_{BR} = 0.7815$, which is consistent with literature values [48, 46, 61] (Fig. 3.8(f)).

From these values we determine Purcell factors of $F_C = 26.209 \pm 0.02$ and $F_D = 5.123 \pm 0.05$ ($F_C = 9.243 \pm 0.001$ and $F_D = 8.910 \pm 0.0001$) for the angled (parallel) cavity. Due to the bandwidth of the tunable optical filter (~0.3 nm), a small contribution from a second emitter is collected during lifetime measurements for the angled cavity. This contribution is visible when a PL spectrum is taken of the optically filtered collection spot with long integration times (Fig. 3.9(a)).

When the C(D) transition is on resonance, the secondary emitter demonstrates a reduced lifetime of 8.008 ± 0.07 ns (6.659 ± 0.2 ns). By extracting the amplitude fit parameters of the quadruple Lorentzian model, we determine amplitude ratios of $\gamma_c = 1.022 \pm 0.002$ and $\gamma_d = 1.971 \pm 0.006$. Given that the D transition demonstrates greater lifetime reduction than the C transition, we conclude that this secondary emitter is orthogonal in orientation to the other two SnV$^-$s of study, and therefore the angular offset between the emitter transition dipole and cavity mode is given by $\theta = 45 - (55 + \phi) + 90$.

Accounting for this second emitter, we can once again use Eq. 3.6 to solve for η_{BR} and ϕ. From

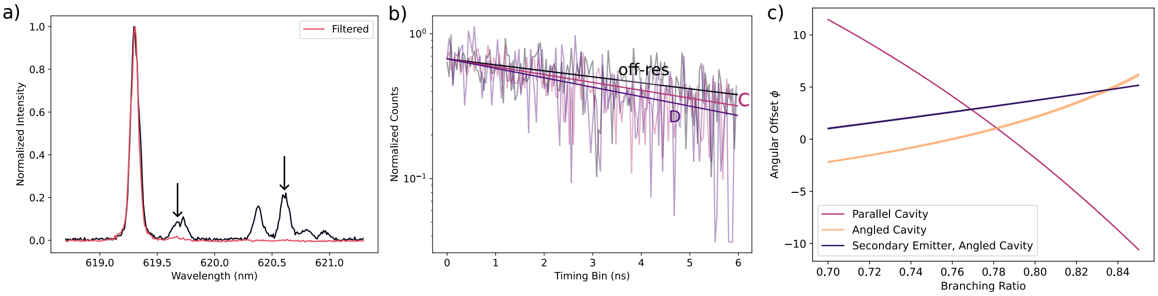

Figure 3.9: Lifetime reduction of secondary emitter.
(a) Filtered and unfiltered PL spectra of the collection spot for the angled device. Both are normalized in order to show degree of suppression of other transitions by the tunable filter. The arrows indicate the estimated C and D transitions of the second emitter. In the filtered spectrum, it is evident that a small contribution of the secondary C transition remains. **(b)** Lifetime reduction for when the secondary emitter is on/ off resonance. The C transition demonstrates a reduced lifetime of 8.008 ± 0.7 ns, and D demonstrates a reduced lifetime of 6.659 ± 0.2 ns. The off resonance lifetime is 10.507 ± 0.2 ns. **(c)** Solution for Purcell analysis for three emitters. Although the three functions fail to intersect, minimizing the average difference yields $\eta_{\mathrm{BR}} = 0.7815$, consistent with the value calculated in Section 3.2.2.

Fig. 3.9(c), we see that the three trend lines fail to fully intersect. This discrepancy is likely due to increased fitting errors, stemming from reduced SNR per lifetime measurement for this more weakly coupled emitter. Therefore, we instead minimize the averaged pairwise differences between for all trend lines, identifying the optimal value $\eta_{\mathrm{BR}} = 0.7815$, identical to that determined in Section 3.2.2. Therefore, we determine that this secondary emitter demonstrates Purcell factors of 1.048 ± 0.005 and 8.796 ± 0.05, for the C and D transitions, respectively.

We note that since the second emitter in the angled cavity demonstrates a larger Purcell factor for the D transition, we conclude that the emitter is oriented orthogonally to the other two emitters of study.

3.3 Discussion

Our results highlight the importance of analyzing the lifetime reduction for both the C and D transitions. By explicitly modeling the collective spontaneous emission dynamics and accounting for the orthogonal polarizations of the C and D transition dipole moments, we are able to extract not only the individual Purcell factors of each transition, but also the intrinsic C/D branching ratio of the SnV$^-$.

This contrasts with prior work where Purcell factor is reported per SnV$^-$ center and calculated by applying lump-sum correction factors [78, 46]. Furthermore, branching ratios were previously inferred from PL spectra or determined through quasi-resonant excitation [46, 91]. Distinguishing the Purcell enhancements of the C and D transitions provides a more faithful description of the underlying physics, which indicates the optimal emitter-cavity alignment for maximizing subsequent spin-state readout fidelity.

The asymmetry in cavity coupling between orthogonal transitions further serves as a sensitive probe of dipole orientation relative to the cavity field, allowing us to extract the angular alignment of the fabricated devices with respect to the crystal axes. If the collective lithography offset from the main lattice vector is known independently, for example via XRD measurements, the spontaneous emission equations for the C and D transitions in one cavity alone are sufficient to solve directly for both the branching ratio and Purcell factors. However, by investigating a second, angled cavity, we both validate our model and demonstrate the advantages of aligning the cavity mode polarization as closely as possible to the dipole orientation of a specific transition. Indeed, if the angled cavity had been oriented 45° from the lattice vector rather than 55°, from our analysis we would expect complete suppression of one transition and further increased enhancement of the other. However, by allowing for a controlled 10° of angular misalignment, we ensure that we to observe some degree of coupling between both C and D transitions of the emitter, allowing for greater accuracy in our Purcell factor analysis.

3.4 Conclusion

In this manuscript we report the fabrication of 1D photonic crystal cavity nanobeams from thin film diamond membranes. We achieve upwards of $\sim$6000 quality factors, and observe up to 10-fold PL enhancement from a select SnV$^-$ when on resonance with the cavity mode. To accurately quantify our Purcell factors, we take time-resolved measurements and determine the optical lifetime reduction of the emitter. Despite optically filtering to isolate the C transition in collection, we also observe lifetime reduction when the cavity is on resonance with the D transition of the same emitter.

From this picture, we construct a model describing the spontaneous emission dynamics of the system. By studying the cavity-emitter coupling behavior of two separate devices—one roughly parallel and the other at $\sim 55°$ to the diamond $\langle 100 \rangle$ lattice axis—we are able to extract a C/D branching ratio of $\eta_{\mathrm{BR}} = 0.7815$ and a collective fabrication angular offset of $\phi = 1.1 \pm 0.1°$. Using the determined value of η_{BR}, we determine Purcell factors of $F_C = 9.243 \pm 0.001$ and $F_D = 8.910 \pm 0.0001$ for the two transitions in the parallel cavity, and $F_C = 26.209 \pm 0.01$ and $F_D = 5.123 \pm 0.05$ for the angled device.

Our Purcell factor can be further increased through fabrication optimization, such as improving feature fidelity and minimizing device sidewall angles in the etch process (Appendix B.1.3). Furthermore, cavity-SnV$^-$ coupling can be improved through targeted and aligned implantation of Sn^{2+} into the cavity mode volume [78]. Implantation density can be reduced for future devices in order to produce cavities with single color centers in the mode volume, while also cutting down on general implantation damage of the material.

Our fabricated sample is compatible with microwave spin driving experiments. By enhancing the SnV^{-} ZPL emission, readout fidelity of SnV^{-} spins can be significantly enhanced [50, 92]. Photon extraction can also be further improved by incorporating grating couplers or adiabatic tapers, which would enable color center addressing and photon collection in either transmission or reflection [93, 61, 94, 41]. These developments would enable near-unity fidelity of single shot readout of the electron spin in the SnV^{-}, and pave the way for scalable quantum network nodes.

Chapter 4

Heterogeneous Integration of Diamond Color Centers and Thin-Film Lithium Niobate

$\mathcal{NB}$: Portions of this chapter are reproduced from the manuscript 'Efficient Photonic Integration of Diamond Color Centers and Thin-Film Lithium Niobate' [60] with permissions. Copyright 2023, American Chemical Society.

4.1 Introduction

The advantages of diamond as a quantum material hinge upon its large electronic band gap, high Debye temperature, and its relative lack of (or engineerable) nuclear spin environment. In addition, diamond is a highly symmetric crystal composed of only carbon atoms bonded in a tetrahedral structure. Although these properties position diamond as an excellent host material for coherent color center spin qubits, the material is lacking in other functionalities necessary for implementing scalable quantum networks. For instance, given stochastic variations in crystal lattice environment, color centers each have variable ZPL wavelength. Thus, the interference and entanglement of multiple defect spin qubits require either an exhaustive survey to find a pair of defect centers with overlapping ZPLs [95, 96] or tuning color center transitions on resonance with one another through applied DC electric fields or strain [86, 97, 98, 99, 100]. Another option involves tuning the frequency of emitted photons instead of the color center transitions themselves [101, 43]. This last option listed can be particularly attractive as group-IV color centers, with their inversion symmetric, frequency shift quadratically to DC electric fields, limiting their wavelength tunability [97, 99]; strain, although suitable for controlling optical transitions, hinders spin state readout when applied in excess [50, 52].

However, realizing a frequency modulator directly in diamond is precluded by the material's lack of a substantial electro-optic or acoustic-optic effect.

More critically, the majority of studied diamond color centers have ZPLs in the visible wavelength range. These wavelengths experience significant propagation loss in optical fibers (> 5 dB/km), impeding the implementation of long-distance, scalable quantum networks. For this purpose, visible wavelength photons would ideally be converted with high efficiency to telecommunication wavelengths (∼1550 nm, loss < 1 dB/km) while maintaining encoded quantum information [102, 103, 104, 105]—another capability that diamond lacks. Indeed, such functionalities require sufficiently strong optical nonlinearities. I now introduce this concept in brief by following along the formulation presented in [106]. The nonlinearity coefficients ($\chi^{(n)}$) can defined through expanding the dielectric polarization density ($P(t)$) in terms of a general input electric field ($E(t)$):

$$P(t) = \epsilon_o(\chi^{(1)}E(t) + \chi^{(2)}E^2(t) + \chi^{(3)}E^3(t) + \mathcal{O}(E^4(t))) \tag{4.1}$$

In this expression, the coefficients $\chi^{(n)}$ are scalars; when the equation is generalized to vectors ($\vec{\mathcal{P}}(t)$, $\vec{E}(t)$), $\chi^{(n)}$ then become $n+1$ rank tensors. This generalization is especially necessary for anisotropic crystals, whose refractive index vary along different lattice directions. In the case that the electric field input consists of components with multiple frequencies, we can express the field as:

$$E(t) = E_1 e^{-i\omega_1 t} + E_2 e^{-i\omega_2 t} + c.c. \tag{4.2}$$

upon which substitution into the second order term of 4.1 yields the following terms:

$$P^{(2)}(t) = \epsilon_o \chi^{(2)} E^2(t) = \epsilon_o \begin{cases} 2(|E_1|^2 + |E_2|^2) \\ E_1^2 e^{-i2\omega_1 t} \\ E_2^2 e^{-i2\omega_2 t} \\ 2E_1E_2e^{-i(\omega_1+\omega_2)t}, 2E_1^*E_2^*e^{i(\omega_1+\omega_2)t} \\ 2E_1E_2^*e^{-i(\omega_1-\omega_2)t}, 2E_1^*E_2e^{i(\omega_1-\omega_2)t} \end{cases} \tag{4.3}$$

From the inhomogeneous wave equation[1], the oscillating terms indicate generation of radiation at their given frequencies. For second order processes, input frequencies can be doubled ($2\omega_1, 2\omega_2$), added ($\omega_1 + \omega_2$), or subtracted ($\omega_1 - \omega_2$). A similar expansion can be performed for the third order expansion term $P^{(3)}(t)$, for which an even larger number of mixing processes emerge involving up to three frequency inputs. Therefore, optical nonlinearities are highly attractive as they provide a mechanism for optical frequency conversion.

Unfortunately for centrosymmetric materials, such as diamond, the even order terms in the $P(t)$ expansion vanish under symmetry arguments. Indeed, this does not completely bar the material

---

[1] $\nabla^2 E(t) - \frac{n^2}{c^2}\frac{\partial^2 E(t)}{\partial t^2} = \frac{1}{\epsilon_o c^2}\frac{\partial^2 P_{nonlinear}(t)}{\partial t^2}$

from displaying nonlinear effects. Any material can take advantage of the next highest nonlinear expansion coefficient, $\chi^{(3)}$. However, $\chi^{(3)}$ processes, which scale cubically with input field strength, are considerably weaker and less efficient that the second order processes which scale quadratically [69, 107, 108, 109]. Or, for a material such as diamond, an effective $\chi^{(2)}$ may be induced through the presence of hosted nonlinearities, such as in the form of a sufficiently high density of color centers, but this requires careful materials engineering [110, 111].

More scalable is to simply seek out another material platform which intrinsically possesses a second order optical nonlinearity. One such material that has garnered much excitement is the artificially synthesized, ferroelectric crystal lithium niobate ($LiNbO_3$, or as commonly notated, LN) [112]. By possessing a $\chi^{(2)}$ optical nonlinearity, LN is therefore able to facilitate all frequency conversion and mixing processes described above in 4.3. Realistically, the efficiency of one of these processes is selectively optimized through phase, or momentum, matching. The phase mismatch of a three-wave process, consisting of frequencies $\omega_1, \omega_2, \omega_3$, is given by:

$$\Delta k = k_1 + k_2 - k_3 \tag{4.4}$$

where $k_i = \frac{n_{eff}(\omega_i)\omega_i}{c}$ is the wave vector of a mode at frequency ω_i, guided by an effective refractive index $n_{eff}(\omega_i)$. True phase matching requires $\Delta k = 0$, which allows for the high efficiency transfer from the input pump frequency to the targeted output frequency or frequencies. Not satisfying the phase matching condition leads to oscillation in energy between input and output over the full device propagation length [113]. $\Delta k = 0$ can be achieved through either birefringent or intermodal phase matching, where one or more mode of the three propagates at a different polarization or spatial profile than the others, respectively [113]. However, by doing so, the efficiency of frequency conversion is limited as the overlap with either $\chi^{(2)}$ tensor elements or among the spatial profiles of interacting modes is reduced [113]. These limitations are therefore addressed through a technique available to a number of ferroelectric crystals: periodic poling. In periodic poling, strong voltage pulses are applied at controlled intervals in the material, reversing the ferroelectric domains of these targeted regions. Periodic poling is not true phase matching as $\Delta k \neq 0$, but instead a form of quasi-phase matching. By designing the length of inverted regions to be $\Lambda = 2\pi/|\Delta k|$, the oscillations in energy transfer between input and output modes are canceled out, leading to efficient energy transfer from input to output frequencies [113].

In addition to strong optical nonlinearities, LN also possesses a host of other material functionalities coupling numerous material degrees of freedoms. These include strong electro-optic, acousto-optic, piezo-electric effects. Moreover, similar to diamond, LN has a wide transparency window, ranging from 400 nm to ~5 μm, and a relatively high refractive index ranging from ~2.2-2.4 [112, 113, 114]. Additionally, thin-film LN (TFLN) membranes, bonded to low index or sacrificial substrates, have recently been commercialized, positioning this material as a premier and versatile platform to realize sophisticated photonic integrated circuits and active components which are impossible in diamond. Thankfully, as of now, no spin qubit candidates have been identified in LN [2]. Therefore, these two materials working in conjunction offers an avenue towards low loss routing of the coherent photons from diamond color centers for the purpose of scalable quantum networks.

As with any promising approach, utilizing LN for high efficiency quantum frequency conversion of diamond color center photons has already been demonstrated for NV$^-$, SiV$^-$, and SnV$^-$ centers [102, 103, 43, 105]. Indeed, with the SiV$^-$, as reported in [43], LN was used to both convert visible wavelength photons to telecommunication wavelengths and compensate for frequency discrepancies between different quantum nodes. However, heterogeneous integration of TFLN and diamond for the purpose of quantum frequency conversion has yet to be demonstrated. Direct integration of photonic devices on-chip offers an avenue for both higher frequency conversion efficiency by means of tighter mode confinement and lower loss coupling between the two materials. In collaboration with the Safavi-Naeini group here at Stanford, we demonstrate preliminary photonic integration between diamond and TFLN and report the optical addressing of the color centers through integrated channels. Due to material constraints, this work was performed with SiV$^-$ centers, which has as a ZPL at 737 nm instead of SnV$^-$'s 620 nm.

In this chapter, I will discuss efficient heterogeneous integration of a diamond nanobeam featuring incorporated SiV$^-$ color centers with a TFLN platform using a mechanical pick-and-place approach [115, 116, 117, 118]. By precisely placing double-tapered diamond nanobeams, we demonstrate the bridging of a gapped TFLN waveguide with a diamond-to-LN transmission efficiency of $92 \pm 11\%$ per facet at 737 nm, corresponding to the SiV$^-$ ZPL wavelength, averaged across multiple measurements. We find an approximately 2-fold improvement in ZPL photon extraction via integrated TFLN collection channels compared to out-of-plane collection from the same device. By taking into consideration measured grating coupler efficiencies, we can infer a more than 10-fold improvement in photon channeling into the TFLN waveguide compared to confocal collection channels. Our results demonstrate a crucial step towards the incorporation of high-quality diamond spin qubits into a scalable nonlinear photonics platform.

4.2 Results

4.2.1 Device Fabrication and Transfer

Our device consists of a diamond double-tapered nanobeam with incorporated SiV$^-$ centers bridging a gapped, undercut TFLN waveguide, imaged in Fig. 4.1(a). The SiV$^-$ color centers are generated during a chemical vapor deposition (CVD) overgrowth process on an electronic grade bulk single-crystalline diamond. We fabricate the diamond nanobeams using the well-established quasi-isotropic

---

[2] Otherwise diamond might be out of a job!

etching technique following the procedures outlined in [119, 120, 121, 115, 59] (see supporting information). Our diamond devices consist of a 10 μm long rectangular nanobeam with 10 μm tapers at each end, for a total length of 30 μm. The nanobeam has a target thickness of $\sim$ 200 nm and its width is tapered from $\sim$ 350 nm to $\sim$ 50 nm at the taper end. The device is anchored to the bulk substrate via a thin tether, around which the nanobeam is widened slightly to reduce scattering effects of the tether on optical transmission.

The TFLN waveguides are fabricated following the techniques demonstrated in [122]. We first pattern a negative resist mask atop a lithium niobate-on-insulator (LNOI) substrate using electron beam lithography. We then employ Ar ion milling to etch the waveguides. A second photolithography mask and ion mill step is used for additional removal of the TFLN slab to expose the buried oxide layer of the LNOI. An additional acid cleaning procedure partially etches this oxide, thereby undercutting the waveguide sockets. The completed TFLN waveguides are approximately 190 nm thick atop an approximately 60 nm thick slab and $\sim$ 1 μm wide, which assists in the placement of the diamond nanobeam by allowing for a larger margin of alignment error (Fig. 4.1(b)). The waveguides adiabatically taper down to $\sim$ 100 nm over a length of 5 μm. A 15 μm gap is left between the two waveguides to serve as a "socket" for a diamond nanobeam. Each waveguide ends in a grating optimized to couple 737 nm light to and from the device (see supporting information).

Following fabrication, the diamond nanobeam is transferred via pick-and-place to the TFLN socket. The mechanical transfer process is carried out using a home-built micro-manipulation setup equipped with confocal imaging capabilities and dual tungsten "cat-whisker" needles, each with a $\sim$ 70 nm tip radius. To assist with the mechanical break-off process, the holding tethers are partially cut via focused ion beam (FIB) etching. During transfer, precise orientation of the nanobeam can be controlled with the dual needles, while the LN chip is mounted on a combination of translation and rotation stages. After careful positioning, strong adhesion between the diamond nanobeam and the TFLN via Van der Waals forces allows us to remove the attached needle by pulling it down into the etched trench between the TFLN waveguides. Ultimately, the diamond nanobeam tapers are positioned inversely to the LN "socket" tapers, enabling high-efficiency adiabatic transfer of light between the TFLN waveguide and the diamond nanobeam, as shown in Figs. 4.1b,c. From the simulations presented in Fig. 4.1(c), we expect a theoretical upper bound on the single taper transmission efficiency of approximately 98%.

4.2.2 Optical Characterization of Devices

We characterize our device in a closed-cycle Montana cryostat at a temperature of $\sim$5 K utilizing a home-built confocal microscopy setup consisting of two distinct access arms. We refer to these collection arms as the confocal and transmission paths. The transmission path can be removed from the apparatus by withdrawing the dichroic just before the cryostat. The full measurement apparatus is schematically depicted in Fig. 4.2.

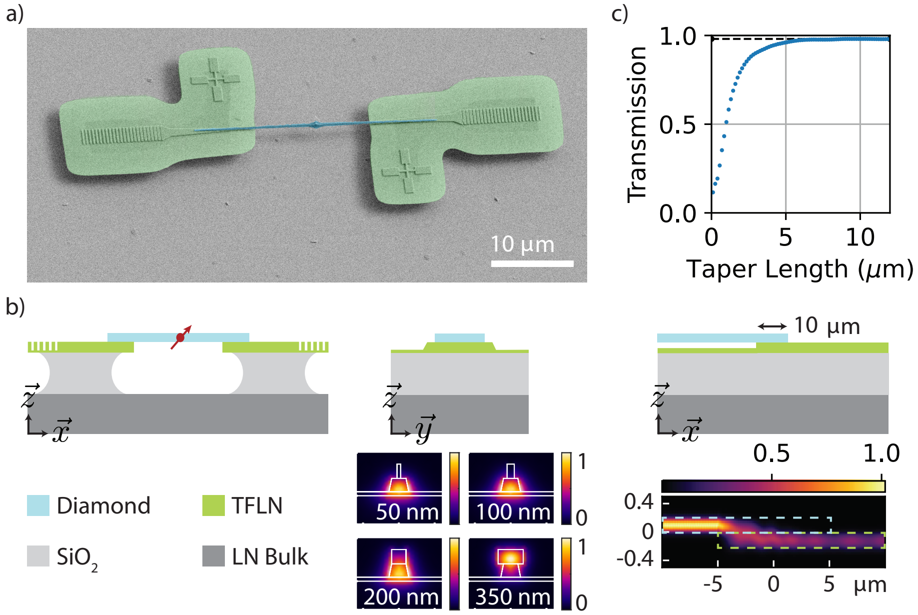

Figure 4.1: Structure for adiabatic transfer of light from diamond to thin-film lithium niobate. **(a)** False-colored SEM image of the fully-integrated nanobeam device, with a few nm of Au sputtered atop for charge dissipation. Green corresponds to the TFLN, while blue represents the diamond nanobeam. As evident from the image, the TFLN slab around the device has been etched, revealing the buried oxide layer, which is partially undercut, leaving a partially-suspended TFLN platform. **(b)** Schematics and simulations of the device. (Left) Side-profile. (Mid) Simulated cross-section of the inverse taper region. A diamond nanobeam rests on thin-film lithium niobate on insulator, with a buried oxide layer. The below four images depict COMSOL™ simulations of the fundamental TE mode of the hybridized waveguide, demonstrating adiabatic mode transfer between the diamond and TFLN. The width of the diamond waveguide is given in each inset, with the TFLN waveguide top width fixed at 200 nm. Each plotted region is 1.2 μm wide and 1 μm tall and depicts the electric field norm, normalized to its maximum. (Right) Length-wise cross-section schematic of the adiabatic taper simulation. The taper is simulated with a 10 μm overlap between the diamond nanobeam taper and the TFLN taper. The lower image depicts a Lumerical simulation of the normalized electric field intensity, with outlines indicating the approximate locations of the diamond and TFLN waveguides. All x- and y-axis dimensions are in microns. **(c)** Lumerical FDTD simulations of transmitted power between the diamond and TFLN with swept taper lengths. The maximum simulated taper transmission efficiency is $\sim 98\%$, indicated by the dashed black line.

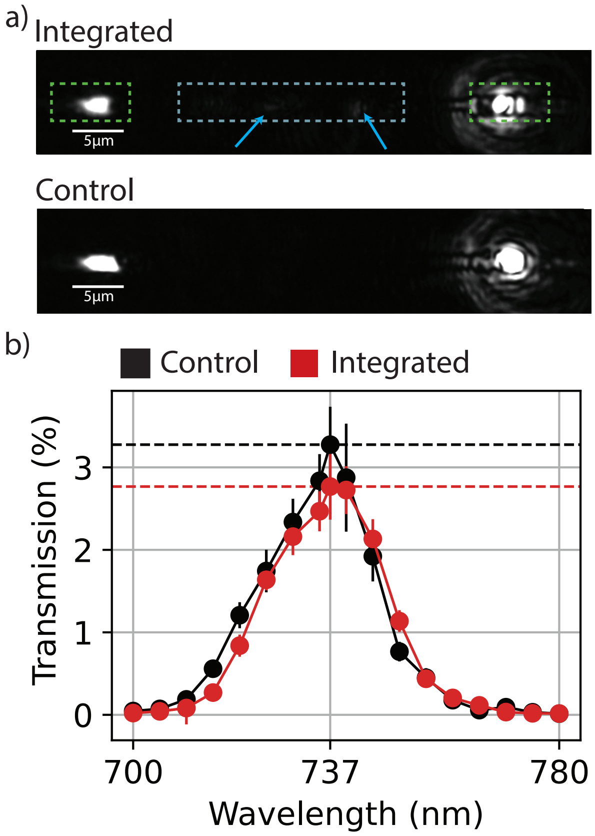

Figure 4.2: Schematic of measurement setup for optical characterizations. “PC” (polarization controller), “PD” (photodiode), “99 : 1” (99%: 1% beamsplitter), “4f” (4-f imaging path, lengths not to scale), “HWP” (half-wave plate), “FC” (fiber-to-free space coupler), “5 K” (5 Kelvin). The dashed box indicates the removable dichroic beamsplitter and transmission path. We achieve spatial separation of the two transmission collection spots via a D-shaped mirror.

Transmission

As a first step, we measure transmission through our device, using the TFLN grating couplers to characterize the single-taper transmission efficiency between the diamond and LN. Using the transmission measurement path, we send a narrow-band laser source through one grating coupler and measure the output power through the other. The input laser power is calibrated via a fiber beamsplitter and photodiode at the input. The output transmitted light is coupled into a single mode fiber and routed to a second photodiode. We sweep the Ti:Sapphire laser excitation from 700 nm to 780 nm in intervals of 5 nm, with a separate measurement performed at 737 nm, specifically, as demonstrated in Fig. 4.2(b). Direct transmission through the device at 737 nm is determined to be $2.8 \pm 0.4\%$ from single-mode fiber to single-mode fiber, averaged over four distinct measurements. We then shift the stage to a "control" device, consisting of a fully-connected (i.e., no taper or gap) TFLN waveguide with nominally identical grating couplers, while keeping the excitation and collection alignment fixed. Transmission through the control device (similarly averaged across four distinct measurements) is $3.3 \pm 0.5\%$. We optimize the transmission through this control device solely by translating the device around beneath the excitation/collection paths. These transmission values are not corrected for any additional losses such as the finite transmission efficiency of various optical elements (objective, silver mirrors) and non-perfect alignment. Measuring the control device yields a lower bound for the single-mode grating coupler efficiency of $17.3 \pm 1.2\%$, in agreement with grating coupler simulations (see supporting information). Comparing the transmission values of our device with the control device allows the diamond-LN transfer efficiency to be inferred. Importantly, the control device is measured during the same cooldown using the exact same external optical alignment of the excitation and collection arms; only the sample is displaced between measurements. Attributing all additional losses in the device to the adiabatic taper facets, we conclude that each diamond-LN taper has a transmission efficiency of $92 \pm 11\%$ at 737 nm assuming equal taper and grating efficiencies (Fig. 4.2(b) – see supporting information for additional details on the calibration procedure). This high efficiency is visualized by the lack of significant scattering at both taper contact points to the TFLN and along the diamond nanobeam in Fig. 4.2(a). Importantly, grating couplers are very sensitive to the angle and focal plane of incident light. Therefore, crosstalk and hysteresis in our stage motion can introduce error into this efficiency calibration. However, additional repeated measurements across multiple thermal cycles yield similarly consistent values for taper efficiency. Furthermore, while this is the highest-efficiency device we measured, a second device exhibits an estimated single-taper transmission efficiency of greater than 80% (see supporting information).

Optical Addressing of SiV^-

We next perform photoluminescence (PL) measurements on SiV^- color centers embedded in the diamond nanobeam. There are two measurement configurations: one with the excitation and collection co-localized via the confocal path (C/C), and one with confocal excitation but collection through

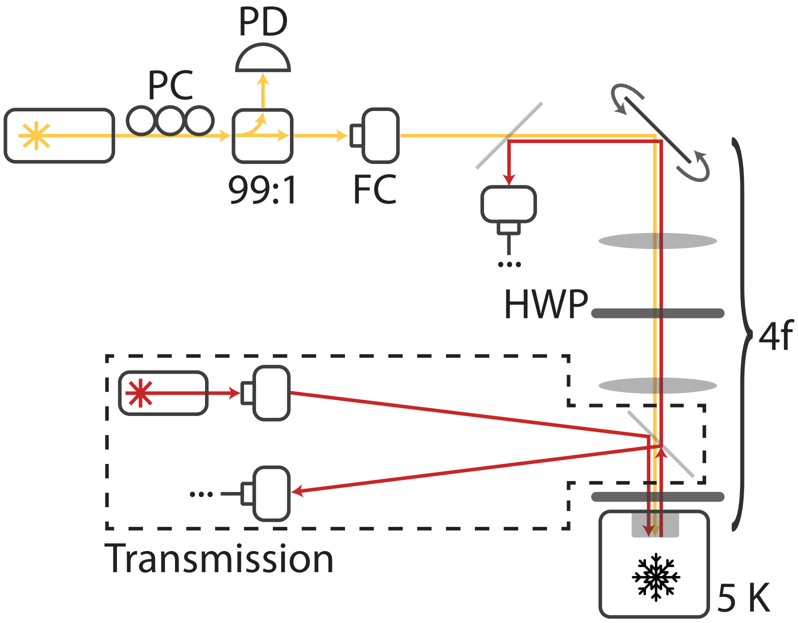

Figure 4.3: Transmission characterization through the integrated device.
(a) (top) Camera image of efficient transmission of narrowband laser light through the integrated device, indicating high taper efficiency at the diamond/TFLN interface. Minimal scattering (indicated by arrows) at the contact points and along the device further demonstrates efficient adiabatic transfer of light. The diamond nanobeam and grating coupler locations are indicated by the blue and green dashed boxes, respectively. (bot) Camera image for comparison of the fully-connected TFLN control device. Images taken at 20 ms camera exposure. **(b)** Average transmission through the integrated diamond-TFLN device (red) and a fully-connected TFLN "control" device (black). Error bars depict the standard deviation by averaging four measurements over two separate cooldowns of the devices. The dashed black and red lines indicate the transmission at 737 nm for the control and integrated devices respectively.

the grating couplers and transmission path (C/CP). Using a homebuilt confocal scanning microscope, we excite color centers off-resonantly at 710 nm and collect the ZPL emission at 737 nm. The resulting PL maps and spectra are presented in Fig. 4.3(a,b). After locating isolated bright spots in PL, we sweep the optical excitation power and record the PL spectra, comparing the efficiency of SiV^- emission collected confocally to that collected through the integrated, nanobeam channel. We toggle between confocal and grating coupler collection paths by removing the transmission path dichroic and adjusting only the half-wave plate just before the cryostat. We are careful to make minimal extraneous optical adjustments in order to maintain the validity of any comparisons of the collected signal.

From the PL spectra, we observe a small ensemble of emitters arising from the homogeneous distribution of SiV^-s throughout the diamond nanobeam. Therefore, for our specific device, we are unable to isolate a single emitter through off-resonant confocal excitation. To quantify photon extraction efficiencies, we measure PL spectra for different powers and integrate the signal within 6× the FWHM of a representative transition for an SiV^- center, demarcated by gray in Fig. 4.3(b). We note that we select a transition which couples favorably to the diamond nanobeam. Fig. 4.3(c) displays a fit to the saturation model $I(P) = I_\infty/(1 + P_{\mathrm{sat}}/P)$. Errors for photon counts are given by assuming Poissonian photon statistics. From the best fit, We determine saturation powers $\mathrm{P_{sat}}$ of 6.9 ± 0.2 mW (9.8 ± 0.7 mW, 9.3 ± 0.7 mW) and saturation count rates I_∞ of 116 ± 2 kcps (68 ± 2 kcps, 219 ± 8 kcps) for C/C configuration ($\mathrm{C/CP_1}$, $\mathrm{C/CP_2}$). The difference in signal between the two CP configurations can be attributed to preferential emission of the SiV^- in one direction of the nanobeam due to either angular dipole orientation or positioning in the nanobeam (see supporting information). The discrepancy between C/C and C/CP saturation powers can in part be ascribed to polarization adjustments made between the configurations to optimize the power delivery to the color center with the removal of the second dichroic mirror [115] (see supporting information). This effect is expected to be pronounced due to the extreme polarization sensitivity of the dichroics at 710 nm. Additionally, the excitation and collection efficiency of different color centers at the interrogated location depend strongly on the focus of the free space optics as shown in the supporting information. Therefore, any misalignment in the focal plane for each configuration may contribute further to discrepancies in determined saturation powers. Given that we need to reoptimize the alignment when switching between C/C and C/CP configurations this may contribute further to discrepancies in power delivery efficiency.

Since we cannot collect data for powers $P >> P_{\mathrm{sat}}$, we are unable to evaluate the impact of adding an additional background term to our saturation model fit. Hence, we estimate the enhancement factor for photon channeling into the TFLN waveguides by determining the signal ratio between C/C and the combined C/CP rates for the different measured powers and find an average enhancement factor of 2.05 ± 0.15.

As further evidence of emitter co-localization, we measure $g^{(2)}(\tau)$ auto-correlation of its emission

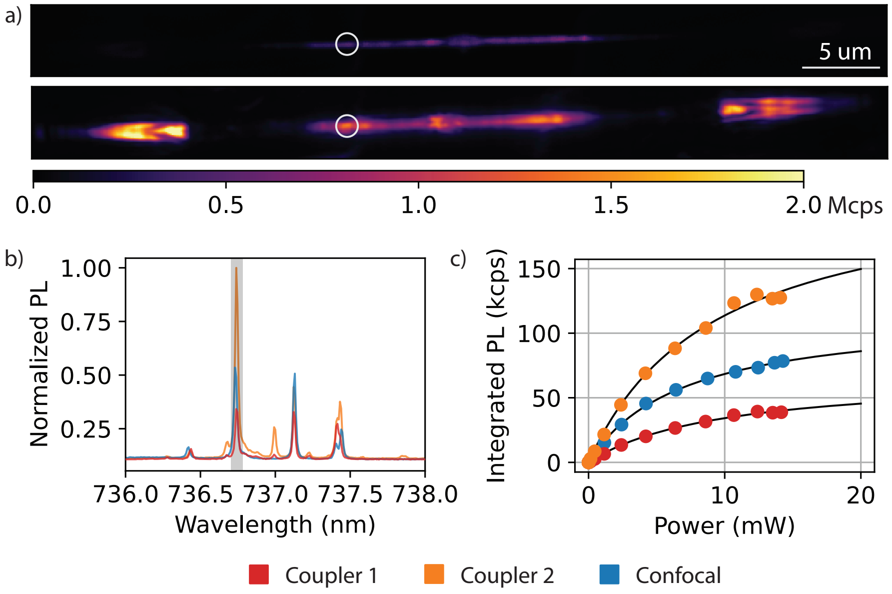

Figure 4.4: Color center PL characterizations.

(a) "Confocal laser scans with confocal collection (top) and stationary coupler collection (bottom). The coupler collection PL scan presented is obtained by counting photon arrivals from the couplers in parallel, with each avalanche photodiode collecting emission from one grating coupler. Over an integration period, these simultaneous counts are summed to yield the total photons collected from both grating couplers. Excitation for both were provided confocally, and scanning was performed utilizing a galvanometer mirror and 4f setup. The white circle in each scan indicates the location of confocal excitation for panels (b) and (c). **(b)** Normalized PL spectrum, overlaid with confocal and both coupler collected spectra. The grey region indicates the post-processed 'filtered' wavelength range, determined by fitting the spectra to multiple Lorentzian peaks and identifying the FWHM of the selected emission peak for a single emitter. **(c)** Saturation curves for each collection configuration. CPS for each power and configuration was determined by integrating the number of counts collected in a spectra within the FWHM ranges identified by Lorentzian fit. PL spectra were each integrated for 2.5 s. The black trend lines represent a standard power saturation fit. Error bars for each data point was calculated using Poissonian photon statistics but are smaller than data markers.

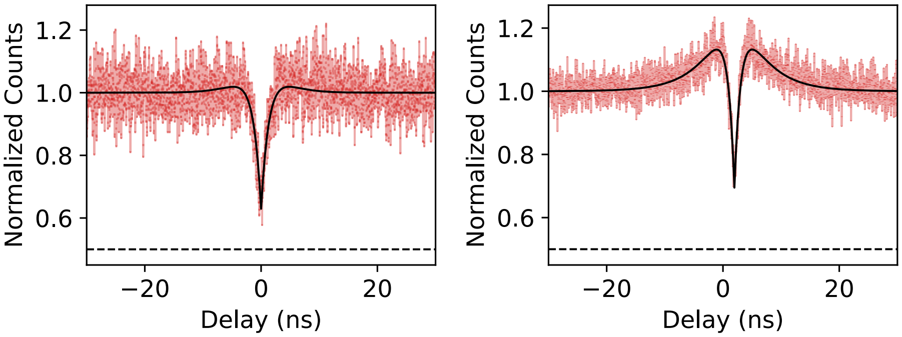

Figure 4.5: Photon autocorrelation measurements using confocal excitation and collected **(a)** confocally for an excitation power of 4.74 mW with $g^2(0) = 0.629 \pm 0.005$ and **(b)** through the grating coupler for an excitation power of 4.43 mW with $g^2(0) = 0.690 \pm 0.004$. The data is fitted using a bunched $g^2(\tau)$ function form, with counts far from the delay dip normalized to 1. The dashed line indicates the 0.5 threshold for single photon emitter characteristics. Error bars are calculated assuming Poissonian photon statistics.

in the C/C configuration using a 50 : 50 fiber beamsplitter. We isolate a single emission line with a series of filters (achieving roughly a 13 nm bandwidth at 740 nm, for more details see supporting information), and observe anti-bunching of $g^{(2)}(0) = 0.629 \pm 0.005$ for an excitation power of 4.74 mW, shown in Fig. 4.4(a).

We then repeat autocorrelation measurements in the C/CP configuration for an excitation power of 4.43 mW, utilizing our device as an integrated beamsplitter to correlate emission between the two grating couplers. We measure a similar $g^{(2)}(0) = 0.690 \pm 0.004$ with this approach, depicted in Fig. **??**(b). The determined autocorrelation values at zero delay indicate emission from a small ensemble of emitters within our filtered wavelength region. This is consistent with the existence of additional peak and broadband background features shown in Fig. **??**(b). We note that the bandwidth of our filter for the autocorrelation measurement is significantly larger than that imposed by post-measurement data filtering in the saturation measurement. Therefore the depth of the autocorrelation dip may be straightforwardly improved by increased spectral filtering.

Bunching in an auto-correlation measurement, observed for both C/C and C/CP configurations, is generally caused by telegraph noise due to either blinking or shelving into a long-lived metastable state. Since the degree of bunching depends on the excitation power [123], the different degrees of bunching present for the two measurements is an additional indication of discrepancy in the power delivery efficiency for the two configurations, caused by the factors discussed above.

Lastly, we consider the robustness of the integration to environmental factors. It should be noted that this particular device survived multiple partial and complete thermal cycles. Furthermore, during one such event, the nanobeam fully detached from the TFLN waveguide socket and the pick-and-place apparatus was used to re-position the nanobeam. In all cases, we observed similarly high transmission efficiency. Additional controlled thermal cycling and targeted testing will be necessary to formally characterize this robustness, but repeated transmission measurements suggest a lack of deterioration in device performance.

4.3 Discussion

Overall, we have demonstrated the photonic integration of diamond color centers with thin-film lithium niobate. Our integration yields a high coupling efficiency of $92 \pm 11\%$ per facet between the diamond and the TFLN. We determine an enhancement factor between confocal collection and the combined rates collecting through the TFLN grating couplers of 2.05 ± 0.15. Correcting for the determined grating coupler efficiency of $17.3 \pm 1.2\%$, we estimate that channeling of SiV^- photons into the TFLN waveguide is improved by more than 10-fold when compared to out-of-plane confocal collection through a high-NA objective. A significant boost could be achieved by enhancing and channeling the color center emission through resonant photonic structures [75, 41], enabling an overall waveguide coupling efficiency $> 60\%$ [124]. Furthermore, for realistic applications, bidirectional emission from the color center can be channeled into a singular direction by adding a retroreflector or purposefully weakening the mirror strength for one side of a photonic resonator.

The emission count rate in our experiment is potentially limited by random placement and non-ideal angular orientation of the SiV^- inside the nanobeam. The homogeneous distribution of color centers within the nanobeam also complicates the probing of single emitter properties in our device. These challenges can be overcome by delta doping and targeted implantation techniques, such as masked or focused ion beam implantation [40, 59, 125, 126].

A major advantage of selective integration is the possibility for large-scale pre-characterization of diamond nanobeams and emitters, enabling a more deterministic device yield [127]. The transfer process could potentially be fully automated using a combination of machine vision and *in situ* transmission measurements.

Our device paves the way for high-efficiency emitter collection on TFLN, enabling single-photon experiments that leverage TFLN's unique properties. We aim to utilize optical nonlinearities in LN for modulating color center emission, thereby demonstrate multi-emitter interference and multiplexing on chip [96]. We further aspire to add additional on-chip capabilities, such as on-chip filters [128] and detectors [129, 130]. On-chip photon routing would enable both the entanglement between several integrated quantum memories and coupling to the same external fiber channel. In combination with recently demonstrated high fiber packaging efficiencies [131], this would enable integrating a large number of quantum memories on the same chip. We also aim to leverage periodic poling in LN to achieve quantum frequency conversion of emitters to the infrared band for integration with the telecom band. These future directions would pave the way towards on-chip heterogeneous platforms linking the excellent optical and coherence properties of solid state spin qubits with the potential of a mature nonlinear photonics platform.

Chapter 5

Outlook

In Chapter 3, I discussed our work coupling the SnV^- to 1D PCCs fabricated in a thin-film diamond platform. From studying two varieties of devices we develop a model describing spontaneous emission dynamics of the cavity-emitter system, from which we can calculate Purcell factors more rigorously. This work paves the way to increasing optical spin-state readout from a SnV quantum node. Then, in Chapter 4, I noted the material limitations of diamond, including the lack of strong optical nonlinearities. The vanishing $\chi^{(2)}$ stemming diamond's centrosymmetric structure significantly limits the material's suitability for applications beyond acting as a host and nanophotonitc interface for color center spin qubits. To address this limitation, we heterogeneously integrate diamond with another mature photonic material platform, thin film lithium niobate. In this section we describe various extensions of the work presented in the previous two chapters.

5.1 Survey of the Field

Here, I provide a brief overview of current demonstrations of entanglement in multiple qubit platforms to serve as metrics for and basis of comparison to inform necessary improvements for the SnV^- center. In addition to color centers in diamond, distributed entanglement demonstrations have been performed in trapped ions, neutral atoms, quantum dots, and rare earth ions [4]. Relevant metrics for these platforms are summarized in Table 5.1; in general there is a tradeoff between entanglement rate and fidelity [132]. Quantum link efficiency is calculated as the product of the entanglement rate and qubit coherence time.

In Table 5.2, I then summarize some qubit operation metrics; for color center candidates, I also list the proportion of ZPL emission, given by the product of the quantum efficiency to the Debye-Waller factor (QE×DW). Furthermore, in Table 5.3, I summarize some demonstrations of quantum frequency conversion of diamond color centers. For all these reports, off-chip frequency converters are used. To this end, I have listed 'external' efficiencies, which take into account coupling losses in

Qubit Platform	Entanglement Rate	Distance	Fidelilty	Quantum Link Efficiency
SiV^- in diamond, electron spins [43]	1 Hz	20 m	0.86/0.74	125×10^{-6}
SiV^- in diamond, nuclear spins [43]*	N/A	35 km	0.69	N/A
NV^- in diamond [132]	22×10^{-3} Hz	10 km	0.534	3.63×10^{-6}
Trapped ions [133]†	5.5×10^{-3} Hz	2 m	0.94	$\sim5.5\times10^{-3}$
Neutral atoms [134]	6 Hz	60 m	0.883	$\sim2.4\times10^{-3}$
Quantum dots [135]	7.3 kHz	N/A	0.616	8.76×10^{-6}
Rare earth ions [136]	2 Hz	N/A	0.592	18.2×10^{-3}

Table 5.1: Summary of recent entanglement demonstrations across different qubit platforms.

For the starred entry (*), [43] notes that the nuclear spin entanglement can be preserved for 500 ms, which can be lengthened to ∼1 s with error detection, although explicit metrics for rate and nuclear spin coherence time were not presented. From [137], the Si^{29} nuclear spin is reported to have a coherence time of >2 s. For entry [133] (†), no explicit ion coherence time is presented, and therefore instead the coherence time reported in [138], is used to provide an estimate. In general, however, the coherence times reported for trapped ion qubits are extraordinarily long, ranging from 0.2 s to 600 s [139].

Qubit Platform	Qubit Operation Temperature or Apparatus	ZPL Emission (QE×DW)
SnV^- in diamond	1.7 K [50]	0.456 [44, 29]
SiV^- in diamond	60 mK [40]	0.234 [123, 140]
NV^- in diamond	4 K [132]	0.03 [15, 35, 36, 37]
Trapped Ions	Trap in vacuum [133, 141]	N/A
Neutral atoms	Optical trap in vacuum [134]	N/A
Quantum dots	∼4 K [142]	∼1 [143]
Rare earth ions	∼0.5 K [136]	N/A

Table 5.2: Summary of operating conditions and emission metrics for various qubit platforms.

the total system, in cases where the distinction is drawn [105, 103].

From these tables, one can notice that the rate of entanglement for quantum dots are remarkably high [135], in part due to their high ZPL emission rate, but are however constrained in their quantum link efficiency by a limited qubit coherence time. Therefore, the SnV^-, with a Debye-Waller factor of 0.57, would be naturally advantageous in achieving improved entanglement rates in comparison to other color center candidates while maintaining extended qubit coherence. Furthermore, in [43], the SiV^- was embedded in one-dimensional photonic crystal cavities, similar to the variety as described in Chapter 3; suggesting the potential of our approaches. Lastly, as discussed in [105, 103], the internal efficiency of the quantum frequency conversion process is much higher than the final system or 'external' efficiency due coupling losses. Indeed for the SnV^-, as reported by [105], the 'internal' quantum frequency conversion efficiency is 48%, indicating ∼20% of system losses.

Qubit	ZPL Wavelength	Converted Wavelength	Conversion Efficiency
SnV^- [105]	619 nm	1480 nm	28%
SiV^- [104]	737 nm	1550 nm	35.6%
SiV^- [103]	737 nm	1350 nm	12.2%
NV^- [102]	637 nm	1588 nm	17%

Table 5.3: Summary of quantum frequency conversion of color center ZPL single photons.

5.2 Cavity Assisted Spin State Readout for the SnV^-

In Chapter 2.1.3, I discussed the spin initialization, readout and control for the SnV^- via addressing an optical 'lambda' system formed from qubit spin states. High photon collection efficiencies are necessary to increase the contrast between 'bright' and 'dark' states. Nanophotonic interfaces address this issue by both channeling emitted photons to an engineered mode and enhancing the spontaneous emission rate via the Purcell effect.

However, what is more powerful is to probe the color spin state via dispersive, cavity assisted readout as has been done for the SiV^- [41, 40]. With sufficient coupling strength, the presence of the color center in the cavity modulates the cavity spectrum in the form of dipole induced transparency [144, 145]. As the two possible spin-preserving transitions have a slight frequency difference (Fig. 5.1(a)), the cavity spectrum differs depending on the qubit spin state and a frequency of maximum contrast can be identified [40]. The spin state is now read out by probing the cavity transmission or reflectance, and similar to before, the spin state therefore is determined through distinguishing 'bright' and 'dark' states of the system (Fig. 5.1(b)). However, in contrast to the protocol described above, no direct excitation of the color center is necessary. This readout scheme proves to faster, with readout times on the order $\sim 10\mu$s (compared to the $\sim$100μs reported in [52]). Furthermore, state differentiation fidelity is superior given improved collection efficiencies from the cavity. Simultaneously, necessary probe power is reduced. As the scheme no longer directly relies on the cyclicity of an optical lambda system, magnetic field alignment requirements can be relaxed [40]. Lastly, this modulation of the cavity spectrum occurs even at considerable cavity detunings of $\sim$100 GHz, which eases the experimental overhead necessary to tune and stabilize cavity resonances with that color center transitions [40]. Also to be noted is that these collected probe photons are effectively entangled with the qubit spin state, and therefore can be routed to entangle spatially separated quantum nodes for the purposes of long-distance quantum networks.

With all these attractive benefits, the natural question to ask is what is the threshold for dispersive readout, and how much the system studied in Chapter 3 needs to be improved. To do so, I introduce here the cooperativity ($\mathcal{C}$), a metric which describes the probability of coherent color center-cavity interaction [146]. Primarily, $\mathcal{C} > 1$ serves as the threshold for which interactions between the color center and cavity mode become deterministic, although not necessarily strongly coupled. $\mathcal{C}$ is related to the Purcell Factor (F) and is defined as:

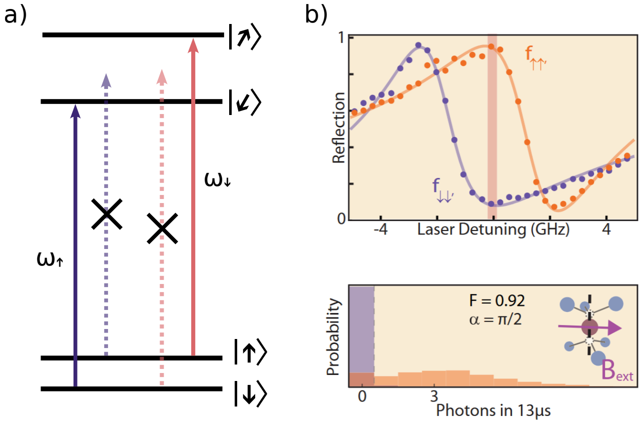

Figure 5.1: Schematic and example of dispersive readout.
(a) Schematic of frequency difference in spin-preserving transitions. As the ground and excited states have slightly different Zeeman spitting rates, the frequencies of the $|\uparrow\rangle$ and $|\downarrow\rangle$ spin-preserving transitions differ. **(b)** Example of dispersive readout of a cavity state. Figure adapted with permission from [40]. Copyright 2019 The American Physical Society. On top, an example of cavity reflectance spectra, modulated by the color center in either state $|\uparrow\rangle$ or $|\downarrow\rangle$. The shaded region indicates the frequency of maximum contrast. Bottom, demonstration of high fidelity single shot readout from the reported system.

$$\mathcal{C} = F_o \frac{\Gamma}{\gamma} = \frac{\Gamma_c}{\gamma} \tag{5.1}$$

where F_o is the Purcell factor, as defined in 2.14, Γ is the natural spontaneous emission rate of the color center, given by Equation 2.13, and γ is the total dephasing rate of the color center. γ consists of the non-enhanced spontaneous emission rate Γ, all other decay pathways (including non-radiative decay and decay into the PSB), and the dephasing rate, which considers all sources of linewidth broadening (for instance, spectral diffusion). Therefore, we can write this out explicitly as discussed in [78]:

$$\mathcal{C} = F_o \cdot \frac{\gamma_o}{\gamma_{exp}} \cdot DW \cdot QE \tag{5.2}$$

where DW is the Debye-Waller factor (~0.57 for the SnV$^-$), QE is the quantum efficiency (~0.8 for the SnV$^-$), and $\frac{\gamma_o}{\gamma_{exp}}$ is the ratio between the lifetime limited and experimentally measured linewidth. As discussed in Appendix B, the color center studied in the parallel device had a depressingly broadened linewidth of ~16 pm, or ~12.5 GHz. From our lifetime measurements, we can roughly estimate our lifetime limited linewidths in the sample to be ~100 Mhz. Therefore, for our highest measured Purcell factor, $\frac{\gamma_o}{\gamma_{exp}} \approx 0.008$, corresponding to $\mathcal{C} = 26.2 * 0.57 * 0.8 * 0.008 \approx 0.097$.

At first glance this number is quite disheartening, until one realizes that the device performance is entirely held back by this broadened linewidth. Indeed, with $F_o = 26$, $F_o{\cdot}DW{\cdot}QE \approx$12, indicating that the defect linewidth can be broadened by over an order of magnitude and we would maintain $\mathcal{C} > 1$—a linewidth of ∼16 pm is simply too much. Even more encouraging is that elsewhere on the sample there are color centers with linewidths just a factor of three broadened from lifetime limits (Appendix B.3). Furthermore, more careful addressing of these color centers alongside the adoption of charge-resonance-checks may be able to effectively stabilize color center and narrow linewidths [30, 52, 147].

However, of course any improvement to the coupling strength through either higher Purcell enhancement or increased spatial and angular alignment would aid in relaxing these stringent thresholds. As discussed thoroughly in Chapter 3, Purcell factors can be boosted by roughly 40% for all coupled emitters simply by rotating the cavities in line with the $\langle 110\rangle$ or $\langle\bar{1}\bar{1}0\rangle$ crystal axis. There has also been recent progress in developing the materials processing techniques to work with $\langle 111\rangle$ diamond, which suggests that in the future this angular misalignment can be further reduced via more advantageous diamond substrate orientations. Positional alignment of the color center can be improved through aligned implantation techniques, such as those reported in [78, 59]. The last and eternal option of course is further improvement of cavity design and fabrication in order to achieve higher Q/V ratios.

In addition to contributing to the implementation of long-distance quantum networks based on the SnV^-, improved photon emission and extraction from a single quantum node allows for cluster state generation [148]. The group-IV color centers are especially suitable to this task given their large fraction of coherent ZPL emission. Furthermore, given the density of SnV^- formation on our current sample, it may be of interest to probe multi-emitter CQED in the system [74].

5.3 Fabrication Improvements

In this section, I list a few ongoing improvements for the fabrication of 1D PCCs. Our measured quality factors are in large part limited by moderate sidewall angle of our etches (∼5-10°). In designing our devices, we surveyed reasonable device dimensions through a parameter sweep of hole diameter and lattice spacing (Fig. 5.2(a)), from which we identified that targeting a hole diameter of 115 nm and sweeping lattice spacing would yield us a high probability of resulting device resonances within the target wavelength range. However, these designs assume perfectly vertical sidewalls. With the introduction of a sidewall angle, all resonances are red-shifted by ∼20-30 nm, yielding fewer devices with resonances suitable for coupling SnV^- centers. Furthermore, a number of devices may have resulted in no measured resonances as the sidewall angle enlarged feature dimensions, causing the central cavity holes to connect (Fig. 5.3(a)). We also suspect that these extreme devices contributed to color center instability due to even greater proximity to fabricated surfaces that anticipated.

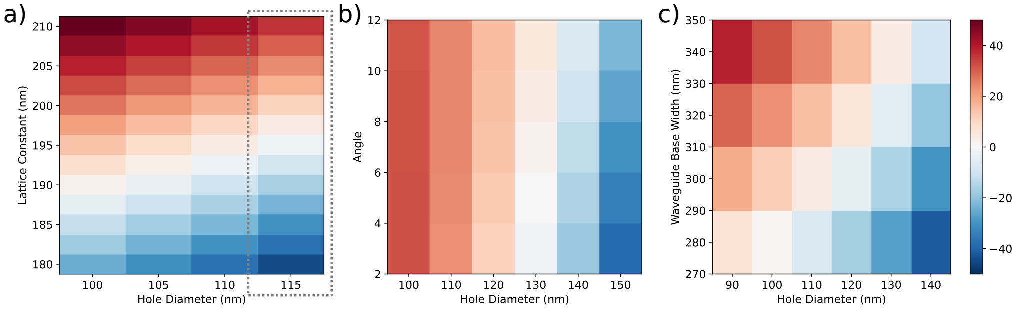

Figure 5.2: Parameter sweeps of 1D PCC design, demonstrating resonance wavelength offset from 620 nm.
(a) Parameter sweep for designing the 1D PCCs reported in Chapter 3. The final hole diameter was fixed at 150 nm and the lattice spacing varied between 180 nm and 210 nm in steps of 2.5 nm (demarcated by the gray box). **(b)** Effects of varying final device angle. Lattice spacing was fixed at 195 nm. From simulations, hole diameters would need to enlarged by ∼25-35 nm in order to compensate for the red-shift of resonances caused by the device sidewall angle. **(c)** Parameter sweep of 1D PCC beam widths. Lattice spacing was fixed at 195 nm and the sidewall angle at 10°. By compensating for the red-shift of the etch sidewall angle by narrowing the nanobeam width, the air hole diameter can be maintained at ∼115-120 nm.

To address this issue, there are two possible avenues. The first is to design the 1D PCCs to take these offsets into account. For instance, we identify that our hard mask etch contributes a roughly $\sim 1-2^\circ$ sidewall and the diamond etch recipe $\sim 10^\circ$ sidewall. Therefore, as an option, we can sweep the beam width instead of the lattice spacing to avoid extreme device dimensions (Fig. 5.2(c)). The other option is to tune the anisotropic etch recipes for greater verticality [1]. The Al_2O_3 hard mask etch was optimized in accordance to the suggestions in [149] and the current verticality likely suffices for our purposes. Therefore, further optimization may focus on the diamond device etch.

Lastly, to note, the current hard mask etch recipe leaves some amount of residue post etch (Fig. 5.3(f)). This residue therefore results in feature infidelity in the diamond device etch step. Therefore, a diligent cleaning procedure post Al_2O_3 etch would aid in final device performance.

5.4 Integration of SnV^- and Quantum Frequency Conversion

In Chapter 4, we discussed the preliminary integration of SiV^- color centers with TFLN passive components. There are two immediate extensions of this work: migrating to the heterogeneous integration with SnV^- and demonstrating quantum frequency conversion (QFC) of SnV^- ZPL emission to telecommunication wavelengths.

To this first point, we verify the feasibility of high efficiency transfer of 620 nm light from diamond nanobeams to TFLN waveguides (Fig. 5.4). Using similar device dimensions and simulation setup

---

[1] Thankfully, by working with diamond thin-films, only two etches need to be optimized.

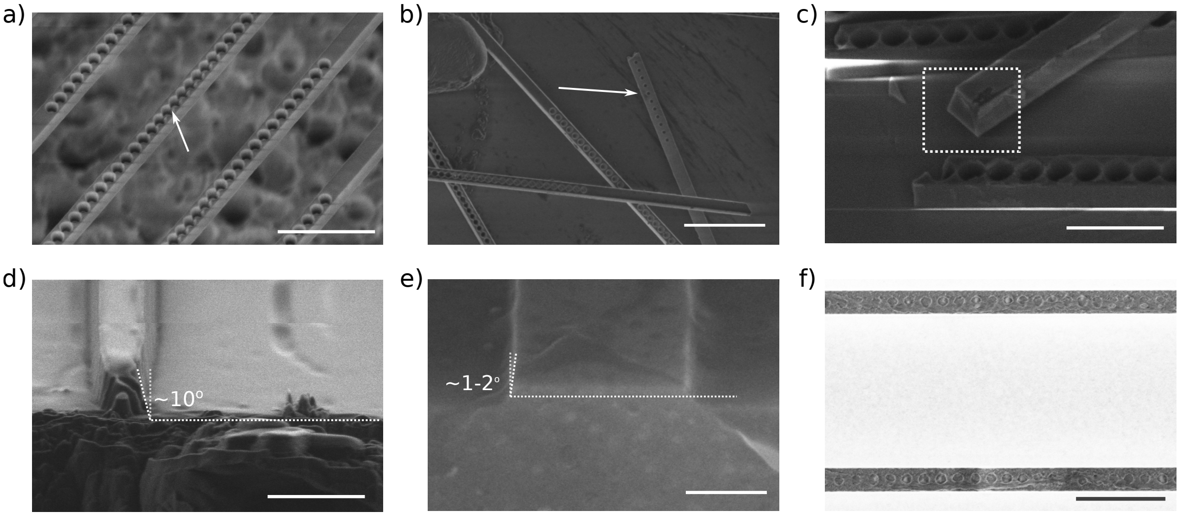

Figure 5.3: SEM images of possible fabrication improvement for 1D PCC.

(a) SEM of devices with connected center holes. The arrow indicates where the beam has become 'notched' by the size of the airholes expanding. The scale bar indicates 500 nm. **(b)** SEM of devices showing the degree of hole tapering in the devices. The arrow demarcates a broken device that has flipped over, showing the size discrepancy of the holes on the bottom surface of the 1D PCCs. This tapering of the air hole size stems from the angled sidewall resulting from the diamond device etch. The scale bar indicates 2 μm. **(c)** SEM of sidewall angle. From a broken device, we can observe the trapezoidal cross-section of the resulting devices. Scale bar indicates 200 nm. **(d)** Measurement of diamond etch sidewall angle. By imaging lines etched into the edge of a bulk diamond test chip, we estimate a $\sim$10°sidewall angle resulting from our current device etch recipe. The scale bar indicates 500 nm. **(e)** Measurement of Al_2O_3 hardmask etch sidewall angle. We estimate a $\sim$1-2°sidewall angle resulting from our current device etch recipe. The scale bar indicates 200 nm. **(f)** Example of post Al_2O_3 etch residue. The residue is reduced through O_2 etching and plasma ashing, however, thus far, is only fully removed via a brief Pirahna acid dip. The timing of the acid clean step is crucial as the acid erodes the Al_2O_3 layer.

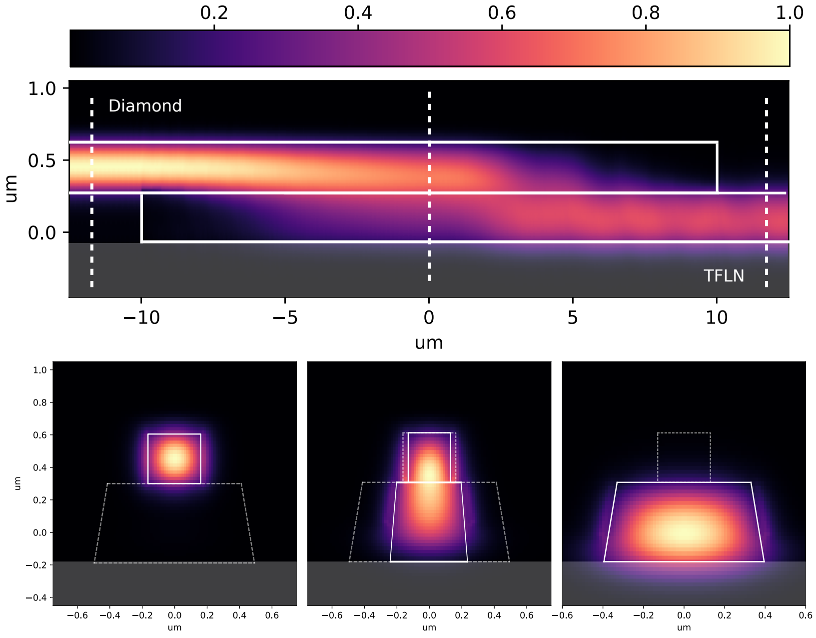

Figure 5.4: FDTD simulation of adiabatic transfer of light from diamond to TFLN. All simulation setup and dimensions are identical to those presented in Fig. 4.1. For an overlap length of 20 μm, the transmission of 620 nm light from the diamond waveguide to TFLB is 99.5%, effectively unity. The solid white lines indicate the outline of the integrated waveguides. The dashed lines in the top panel indicate there cross sections (bottom) have been recorded to monitor the transfer of the TE fundamental mode across the overlap length. For the bottom panels, the solid lines indicate the outline of the beam dimensions for the cross sectional slices; the transparent outlines indicate the maximum diamond and TLFN waveguide dimensions. The gray shaded region indicates the SiO_2 substrate. Colorbar represents normalized electric field intensity.

as that reported in Fig. 4.1, we simulate an adiabatic transfer efficiency of $> 99.5\%$, effectively unity. We note that due to the different ZPL wavelength of the SnV^- a longer interaction length (20 μm) is necessary for high efficiency transfers. Or, the device dimensions can be adjusted to reduce the necessary interaction length. However, from these simulations, the same device architecture is suitable for SnV^- color center integration as for SiV^- centers.

To demonstrate QFC of the SnV^-, we designed for the conversion of 620 nm to 1550 nm via difference-frequency generation (DFG), requiring a strong ~1030 nm pump. However, designing for DFG poses an extra challenge as lithium niobate can facilitate spontaneous parametric down conversion (SPDC). SPDC splits an input photon into two other energy-conserving photons, effectively generating broadband noise red-shifted of the pump wavelength. This noise would therefore lower the signal-to-noise ratio, and potentially obscure the converted 1550 nm signal altogether. Hence, careful filtering would be necessary to isolate the converted SnV^- signal.

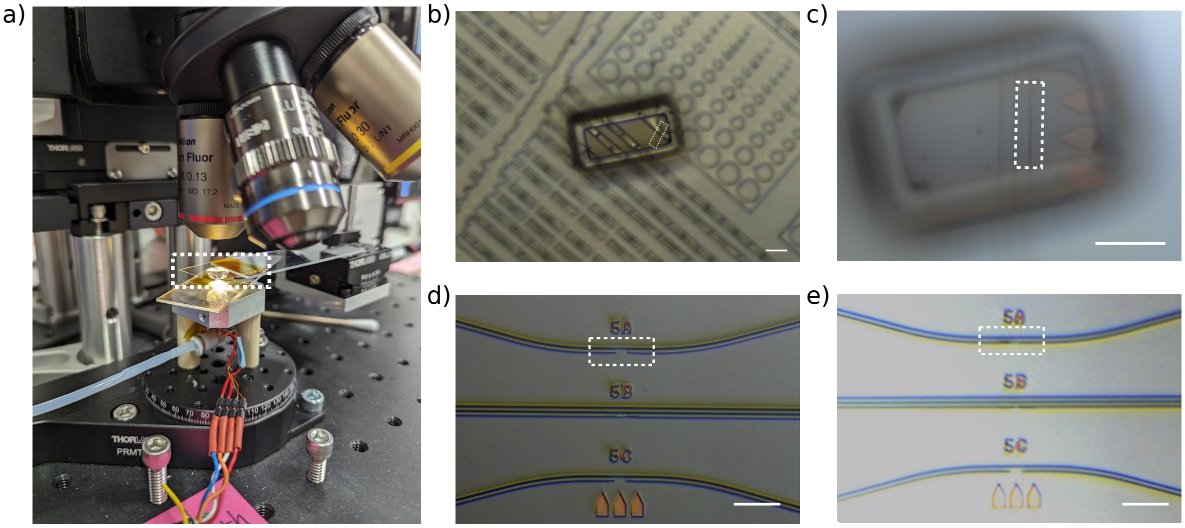

Figure 5.5: PDMS transfer printing for diamond-TFLN heterogeneous integration.
a Image of transfer printing and imaging setup. The dashed white box indicate the pdms stamp bonded to a glass coverslip, which is in turn taped to a glass slide. slide is clamped to a 3-axis piezo stack, and the sample stage is mounted to a rotation stage. **b** White light image of the device pick-up process. The targeted nanobeam is demarcated by the dashed white box. Scale bar indicates 10 μm. **c** White light image of the device alignment and placement process. As before, the targeted nanobeam is demarcated by the dashed white box and the scale bar indicates 10 μm. **d** White light image of the LN 'sockets.' The targeted placement position is marked by the box, and the scale bar represents 10 μm. **e** White light image of final device placement in position indicated in (d). Scale bar represents 10 μm.

As a further improvement, we have migrated away from using fine-tipped needles for pick-and-place. Although the setup described in Appendix C.3 offers excellent precision and flexibility, it is also prone to destructive human error. For instance, as all piezo placement is manually controlled, any mishandling can easily lead to the needle scratching across the surface of the chip, destroying the fabricated LN structures. For the demonstrations reported previously, these incidents are not too tragic, as the layout of passive devices was designed with redundancy in mind. However, in moving towards integration with periodically poled TFLN devices, each device now represents a vastly increased investment in resources and preparation time—a less destructive means towards integration is necessary.

The answer of course is to adapt the sort of PDMS transfer printing techniques that have long been reported, and in fact, adapted for SnV^- integration [118, 150]. Following discussions with the authors of the afore-cited papers, we developed a transfer technique using commercially available 'single-post' PDMS stamps (purchased from Celeprint^{TM}), ranging in size from $\sim 20\mu m^2$ to $\sim 600\mu m^2$. We then plasma activate these stamps and bond them to thin glass cover sheets, which are in turn taped to glass slides for ease of handling. The plasma activation recipe is as follows: 250 mTorr of chamber pressure, 15 sccm O2 flow, 30 seconds of gas flow, and 30 W RF power; the recipe runs for ∼60 seconds. It has been found that these are approximate parameters, and the process is quite robust to deviation.

The transfer-printing imaging system consists of a home-built white light microscope (Fig. 5.5). The stamp is mounted to a 3-axis piezo controlled stack, and the sample is mounted to heater stage. The objectives chosen are all glass-corrected, and allow for imaging through the relatively thick PDMS stamps. Devices are picked up from the diamond substrate by lowering the stamp and then quickly raising it [2]. A small drop of IPA or quick ozone clean can help increase the 'stickiness' of the stamp. The device is then carefully aligned and lowered onto the target TFLN structure; the stamp is then very gradually removed to prevent jostling or removing the device [3]. Heating the sample stage to ∼50-60° C may help facilitate device placement. Although this process can be taxing in its nondeterministic nature, device pick-up and placement can be repeatedly attempted without worry of damage to either the diamond or TFLN sample.

5.5 Summary and Conclusion

In this thesis I have discussed my work contributing to the development of nanophotonic interfaces for solid state defect centers in diamond, specifically the Snv^- and SiV^- centers. These color centers are promising spin qubits for realizing quantum nodes. However, defect centers suffer from limited photon extraction rate when embedded in bulk material, hindering high-fidelity optical spin-state readout and subsequent development of long-distance quantum networks. To this end, nanophotonic interfaces can help improve photon emission, collection and routing.

In Chapter 2, discussed briefly the characteristics and considerations regarding solid state color center defects and summarized various structures that may help with photon collection efficiencies. Then, I focused more specifically on optical cavities, which both channel emitted photons to a well engineered mode and increase the rate of emission itself through the Purcell effect. I described the fundamental model for CQED by analyzing the Jaynes-Cummings Hamiltonian, deriving the threshold for strong and weak coupling regimes of a model system. I ended the chapter by noting the different types of optical resonators utilized for coupling to diamond color centers, before discussing in a bit more detail photonic crystal cavities.

Chapter 3 delves into detail regarding my effort to couple SnV^- centers to 1D photonic crystal cavities, fabricated from a thin-film diamond platform. I start with a discussion of previous methods for fabricating nanophotonic interfaces for the SnV^- and how migrating to a bonded diamond membrane addresses all main failure modes. For our studied devices, we measure up to a 10-fold PL enhancement and up to a 12-fold lifetime reduction for selected SnV^- transitions. I also develop

---

[2] This process can take an hour.

[3] This process, on the other hand, can take multiple hours. A good long podcast can help preserve sanity.

a model for the spontaneous emission dynamics of our system. By considering the orthogonality of the C/D transitions of the SnV^-, we rigorously determine our Purcell factors and also extract the C/D branching ratio.

Next, in Chapter 4, I discuss some of the material limitations of diamond. For long-distance quantum networks, it is necessary to reduce photon loss through optical fiber networks, necessitating the conversion of visible wavelength ZPL photons from diamond color centers to telecommunication wavelengths. However, high efficiency frequency conversion in diamond is precluded by its lack of a second order optical nonlinearty. To this end, we heterogeneously integration SiV^- centers in diamond with thin-film LN, a strongly nonlinear and versatile photonics platform. We demonstrate high efficiency photon transmission between the two materials and pave the way for future demonstrations of quantum frequency conversion on chip.

The work presented in this thesis therefore serve to contribute to realization of quantum nodes based on group-IV color centers in diamond for the purpose of long-distance, distributed entanglement in quantum networks.

Appendix A

Additional Math

In this extraordinarily self-indulgent appendix I write out some supporting mathematical details for the certain equations given in the thesis.

A.1 The Jaynes-Cumming Hamiltonian Interaction Term and Rotating Wave Approximation

Here I write out the justification for the form of the interaction term in the Jaynes-Cummings Hamiltonian ($\hat{H}_{int}$). These calculations follow along those presented in the course EE340, Quantum Photonics, taught by Prof. Vučković [1]. To start the interaction is expressed as that of an atomic dipole ($-e\hat{\vec{r}}$) coupled to an the electric field ($\hat{\vec{E}}(\vec{r_a})$) at its position ($\vec{r_a}$) :

$$\hat{H}_{int} = -e\hat{\vec{r}} \cdot \hat{\vec{E}}(\vec{r_a}) \tag{A.1}$$

The dipole operator can therefore be expanded in the atomic energy levels basic, $|g\rangle, |e\rangle$:

$$\begin{aligned} e\hat{\vec{r}} &= (|g\rangle\langle g| + |e\rangle\langle e|)(-e\hat{\vec{r}})(|g\rangle\langle g| + |e\rangle\langle e|) \\ &= \vec{\epsilon_a}(|g\rangle\langle g| er |g\rangle\langle g| + |g\rangle\langle g| er |e\rangle\langle e| + |e\rangle\langle e| er |g\rangle\langle g| + |e\rangle\langle e| er |e\rangle\langle e|) \\ &= \vec{\epsilon_a}(|g\rangle\langle g| er |e\rangle\langle e| + |e\rangle\langle e| er |g\rangle\langle g|) \\ &= \vec{\epsilon_a}(|g\rangle \mu_{ge} \langle e| + |e\rangle \mu_e g \langle g|) \\ &= \vec{\epsilon_a}\mu_{ge}(\hat{\sigma_-} + \hat{\sigma_+}) \end{aligned} \tag{A.2}$$

where $\mu_{eg} = \mu_{ge} = \langle e| er |g\rangle = \langle g| er |e\rangle$ is the atomic transition dipole moment matrix element, $\vec{\epsilon_a}$ is the dipole orientation vector, and $\hat{\sigma_+}$ and $\hat{\sigma_-}$ are the atomic raising and lowering operators. The

---

[1] The lecture notes and materials from this course have saved me more times than I can count. I have all the pdf's backed up in 2+ places.

terms $\langle g|\, er\, |g\rangle$ and $\langle e|\, er\, |e\rangle$ vanish given symmetry arguments. The electric field operator can be expanded in terms of normal modes in the form:

$$\hat{\vec{E}}(\vec{r}) = i\sum_j \sqrt{\frac{\hbar\omega_j}{2\mathcal{V}_j \max\{\vec{r}\epsilon(\vec{r})|\vec{E}_j(\vec{r})|^2\}}}(\vec{E}_j(\vec{r})\hat{a}_j - \vec{E}_j^*(\vec{r})\hat{a}_j^\dagger) \tag{A.3}$$

We assume that the cavity sustains a single mode, allowing us to reduce the summation:

$$\begin{aligned} \hat{\vec{E}}(\vec{r}) &= i\sqrt{\frac{\hbar\omega_c}{2\mathcal{V}\max\{\varepsilon_M|\vec{E}(\vec{r})|^2\}}}(\vec{E}(\vec{r})\hat{a} - \vec{E}^*(\vec{r})\hat{a}^\dagger) \\ &= i\sqrt{\frac{\hbar\omega_c}{2\mathcal{V}\varepsilon_M}}\frac{E(\vec{r})}{|E(r_{\vec{Max}})|}(\hat{a} - \hat{a}^\dagger)\vec{\epsilon_c} \end{aligned} \tag{A.4}$$

ω_j is the cavity mode frequency, ε_M is the dielectric constant of the cavity medium, and $\mathcal{V}$ is the mode volume. $\vec{E}(\vec{r})$ is the electric field intensity at position $\vec{r}$ and $|E(r_{\vec{Max}})|$ is the electric field amplitude maximum. $\hat{a}^\dagger$ ($\hat{a}$) are the cavity mode raising (lowering) operators. Lastly, $\vec{\epsilon_c}$ is the polarization unit vector of the cavity mode.

Now assembling the interaction Hamiltonian and collecting all constants as g':

$$\begin{aligned} \hat{H}_{int} &= -g'(\hat{a} - \hat{a}^\dagger)\cdot(\hat{\sigma_-} + \hat{\sigma_+}) \\ &= -g'(\hat{a}\hat{\sigma_-} - \hat{a}^\dagger\hat{\sigma_-} + \hat{a}\hat{\sigma_+} - \hat{a}^\dagger\hat{\sigma_+}) \\ g' &= i\mu_{eg}\sqrt{\frac{\hbar\omega_c}{2\mathcal{V}\varepsilon_M}}\frac{E(\vec{r})}{|E(r_{\vec{Max}})|}(\vec{\epsilon_c}\cdot\vec{\epsilon_a}) \end{aligned} \tag{A.5}$$

To invoke the rotating wave approximation, we transform $\hat{H}_{int}$ into the Heisenberg picture. To do so, we use the time evolution operator ($\hat{\mathcal{U}}(t)$) constructed from the non-interacting Hamiltonian ($\hat{H}_o = \hbar\omega_c\hat{a^\dagger}\hat{a} + \frac{1}{2}\hbar\omega_a\hat{\sigma_z}$):

$$\begin{aligned} \hat{\mathcal{U}}(t) &= e^{\frac{-i\hbar}{t}\hat{H}_o} \\ &= e^{-it(\omega_c\hat{a^\dagger}\hat{a} + \frac{\omega_a}{2}\hat{\sigma_z})} \\ &= e^{-it(\omega_c\hat{a^\dagger}\hat{a})}e^{-it(\frac{\omega_a}{2}\hat{\sigma_z})} \end{aligned} \tag{A.6}$$

The final line is allowed for $[\hat{a^\dagger}\hat{a}, \hat{\sigma_z}] = 0$. Performing the transformation for the component operators in $\hat{H}_{int}$ via the Baker–Hausdorff relationship[2]:

$$\begin{aligned} \hat{\mathcal{U}}^\dagger(t)\hat{a}\hat{\mathcal{U}}(t) &= \hat{a}e^{-i\omega_c t} \\ \hat{\mathcal{U}}^\dagger(t)\hat{\sigma_-}\hat{\mathcal{U}}(t) &= \hat{\sigma_-}e^{-i\omega_a t} \\ \hat{\mathcal{U}}^\dagger(t)\hat{a}^\dagger\hat{\mathcal{U}}(t) &= (\hat{\mathcal{U}}^\dagger(t)\hat{a}\hat{\mathcal{U}}(t))^\dagger = \hat{a}^\dagger e^{i\omega_c t} \\ \hat{\mathcal{U}}^\dagger(t)\hat{\sigma_+}\hat{\mathcal{U}}(t) &= (\hat{\mathcal{U}}^\dagger(t)\hat{\sigma_-}\hat{\mathcal{U}}(t))^\dagger = \hat{\sigma_+}e^{i\omega_a t} \end{aligned} \tag{A.7}$$

---

[2] $e^{i\hat{G}\lambda t}\hat{A}e^{-i\hat{G}\lambda t} = \hat{A} + i\lambda[\hat{G},\hat{A}], \frac{(i\lambda)^2}{2!}[\hat{G}[\hat{G},\hat{A}]] + ...$

Substituting these into A.5:

$$\begin{aligned}\hat{\mathcal{U}}^\dagger(t)\hat{H}_{int}\hat{\mathcal{U}}(t) &= -g'(\hat{a}\hat{\sigma_-}e^{-i(\omega_a t+\omega_c)} - \hat{a}^\dagger\hat{\sigma_-}e^{i(\omega_a-\omega_c)t} + \hat{a}\hat{\sigma_+}e^{-i(\omega_a-\omega_c)t} - \hat{a}^\dagger\hat{\sigma_+}e^{i(\omega_a+\omega_c)t}) \\ &\approx g'(\hat{a}^\dagger\hat{\sigma_-}e^{i(\omega_a-\omega_c)t} - \hat{a}\hat{\sigma_+}e^{-i(\omega_a-\omega_c)t})\end{aligned} \tag{A.8}$$

for which we invoke the rotating wave approximation. We justify dropping the terms associated with $e^{\pm i(\omega_a+\omega_c)t}$ which rotate much faster than those associated with $e^{\pm i(\omega_a-\omega_c)t}$ when $\omega_a - \omega_c$ is small. Transforming back to the Schrodinger picture now returns the form of the interaction term used in 2.2. Furthermore, by arranging the terms in g', we recover the atom-cavity coupling factor given by Equation 2.3.

$$\begin{aligned}\hat{H}_{int} &= \frac{1}{2}i\hbar g(\hat{a}^\dagger\hat{\sigma_-} - \hat{a}\hat{\sigma_+}) \\ g &= \frac{2g'}{i\hbar}\end{aligned} \tag{A.9}$$

A.2 Jaynes-Cummings Dressed Eigenstates

From the main text, we solve the Jaynes-Cummings Hamiltonian for eigenenergies and states. In this appendix, I justify the recasting of the eigenstates using the relation $\tan(\theta) = g\sqrt{n+1}/\Delta$. To do so, $\hat{H}_{JC}$ is first expressed in matrix form with basis $|e,n\rangle, |g,n+1\rangle$ as follows:

$$\begin{aligned}\hat{H}_{JC} &= \begin{bmatrix} \langle e,n|\hat{H}_{JC}|e,n\rangle & \langle e,n|\hat{H}_{JC}|g,n+1\rangle \\ \langle g,n+1|\hat{H}_{JC}|e,n\rangle & \langle g,n+1|\hat{H}_{JC}|g,n+1\rangle \end{bmatrix} \\ &= \begin{bmatrix} \hbar\omega_c(n+1) - \frac{1}{2}\hbar\Delta & -i\frac{\hbar}{2}g\sqrt{n+1} \\ i\frac{\hbar}{2}g\sqrt{n+1} & \hbar\omega_c(n+1) + \frac{1}{2}\hbar\Delta \end{bmatrix} = \hbar\omega_c(n+1)\mathbb{I} + \frac{\hbar}{2}\begin{bmatrix} -\Delta & -ig\sqrt{n+1} \\ ig\sqrt{n+1} & \Delta \end{bmatrix}\end{aligned} \tag{A.10}$$

From diagonalization, we find, as written in the main text:

$$E_\pm = \hbar\omega_c(n+1) \pm \sqrt{\Delta^2 + g^2(n+1)} \tag{A.11}$$

And therefore to solve for the eigenstates, while defining $\Omega = g\sqrt{n+1}$,

$$(\hat{H}_{JC} - E_\pm\mathbf{I})\begin{bmatrix} c_e \\ c_g \end{bmatrix} = \frac{\hbar}{2}\begin{bmatrix} -\Delta \mp \sqrt{\Delta^2+\Omega^2} & -i\Omega \\ i\Omega & \Delta \mp \sqrt{\Delta^2+\Omega^2} \end{bmatrix}\begin{bmatrix} c_e \\ c_g \end{bmatrix} = 0 \tag{A.12}$$

From which the following expressions can be written:

$$\begin{cases} E_+ \to -i\Omega c_g = (\Delta + \sqrt{\Delta^2 + \Omega^2})c_e \\ E_+ \to -i\Omega c_g = (-\Delta + \sqrt{\Delta^2 + \Omega^2})c_e \end{cases} \tag{A.13}$$

Dividing by Δ and then recasting with $\tan(\theta) = \Omega/\Delta$:

$$\begin{cases} E_+ \to -i\tan(\theta)c_g = (1 + \sqrt{1 + \tan^2(\theta)})c_e = (1 + \sec(\theta))c_e \\ E_+ \to i\tan(\theta)c_g = (1 - \sqrt{1 + \tan^2(\theta)})c_e = (1 - \sec(\theta))c_e \end{cases} \tag{A.14}$$

Rearranging using the trigonometric relations $\tan(\theta/2) = \sqrt{(\sec(\theta) + 1)/(\sec(\theta) - 1)}$:

$$\begin{cases} E_+ \to -ic_g = \tan(\theta/2)c_e \\ E_+ \to c_g = i\tan(\theta/2)c_e \end{cases} \tag{A.15}$$

Therefore, we ultimately arrive at:

$$\begin{aligned} |+\rangle &= \cos(\theta/2)\,|e,n\rangle + i\sin(\theta/2)\,|g,n+1\rangle \\ |-\rangle &= \sin(\theta/2)\,|e,n\rangle - i\cos(\theta/2)\,|g,n+1\rangle \end{aligned} \tag{A.16}$$

A.3 CQED Time Domain Solution Form

In this section I write out the explicit form for the excited state population plotted in Fig. 2.11b.

In the case of a lossless system, we solve for the excited state population in the subspace $|e,0\rangle, |g,1\rangle$. We can write the general from of the time dependent state $|\psi(t)\rangle$ with initial state $|e,0\rangle = \frac{1}{\sqrt{2}}(|+\rangle + |-\rangle)$:

$$\begin{aligned} |\psi(t)\rangle &= \frac{1}{\sqrt{2}} e^{-it(\omega_c(n+1))} \left(e^{\frac{-it}{2}\sqrt{\Delta^2+\Omega^2}}\,|+\rangle + e^{\frac{it}{2}\sqrt{\Delta^2+\Omega^2})}\,|-\rangle \right) \\ &= \frac{1}{\sqrt{2}} \Big((e^{-it(\omega_c(n+1))}\cos(\theta/2) + e^{it(\omega_c(n+1))}\sin(\theta/2))\,|e\rangle \\ &+ i(e^{it(\omega_c(n+1))}\cos(\theta/2)) + e^{-it(\omega_c(n+1))}\sin(\theta/2))\,|g\rangle \Big) \end{aligned} \tag{A.17}$$

In the case that $\Delta = 0$, this reduces to:

$$|\psi(t)\rangle = \cos(\frac{it\Omega}{2})\,|e\rangle + \sin(\frac{it\Omega}{2})\,|g\rangle \tag{A.18}$$

For which the excited state population is given simply by:

$$P_e(t) = \cos^2(\frac{it\Omega}{2}) \tag{A.19}$$

Now, to plot the dynamics of a lossy system, I use equation 2.10 and set $\gamma = \sqrt{1 - 4g^2/\kappa^2}$. We can solve for eigenvectors and write out the general solution to the rate equations:

$$\begin{bmatrix} \rho_{11}(t) \\ \rho_{22}(t) \\ \rho_{12}(t)+\rho_{21}(t) \end{bmatrix} = e^{-\frac{\kappa}{2}t} \begin{bmatrix} a \\ a \\ \frac{\kappa}{g}a \end{bmatrix} + e^{-\frac{\kappa}{2}t} e^{\frac{\kappa\gamma}{2}t} \begin{bmatrix} b \\ \frac{\gamma-1}{\gamma+1}b \\ \frac{\kappa}{g}(1-\gamma)b \end{bmatrix} + e^{-\frac{\kappa}{2}t} e^{-\frac{\kappa\gamma}{2}t} \begin{bmatrix} c \\ -\frac{\gamma+1}{\gamma-1}c \\ \frac{\kappa}{g}(1+\gamma)c \end{bmatrix} \tag{A.20}$$

Finally, from normalization and enforcing $\rho_{11}(0) = 1$, the coefficients a, b, c are selected such that we can write for the excited state population:

$$P_e(t) = \rho_{11}(t) = \frac{1}{2}e^{-\frac{\kappa}{2}t}\left(1 + \frac{1}{2}e^{\frac{\kappa\gamma}{2}t} + \frac{1}{2}e^{\frac{-\kappa\gamma}{2}t}\right) \tag{A.21}$$

When $g < \kappa/2$, via the Taylor expansion written out in Equation 2.11 we can reduce this equation to:

$$P_e(t) = \rho_{11}(t) = e^{-\frac{g^2}{\kappa}t} \tag{A.22}$$

And in the case of strong coupling, $g > \kappa/2$:

$$P_e(t) = \rho_{11}(t) = \frac{1}{2}e^{-\frac{\kappa}{2}t}(1 + \cos(\frac{\kappa\gamma}{2}t)) \tag{A.23}$$

These are plotted in Fig. 2.11b.

Appendix B

Supplement for 'Quantum Nanophotonic Interface for SnV$^-$ Centers in Thin-Film Diamond'

B.1 Thin Film and Device Fabrication

B.1.1 Diamond Thin Film Preparation

The thin film diamond material used for these experiments was prepared using the 'smart cut' technique and subsequent membrane exfoliation, as reported in [88, 151, 62, 87].

Electronic grade, single crystal diamond material was sourced from Element 6 and polished by Syntek to a miscut angle of 1°. The substrate was then reactive ion etched with an O_2 chemistry to relieve any polishing-induced strain in the first several microns of material. Helium ions (He^{2+}) were implanted into the diamond with an implantation energy of 150 keV at a fluence of $5e^{16}$ ions/cm^2, and the chip was subsequently annealed at 850 °C in a high-vacuum chamber. The graphite layer formed from He^{2+} is ~100 nm thick and ~400 nm beneath the substrate surface [88].

Due to the high implantation energy and dosage, the material above the graphitization is rendered unsuitable for downstream color center formation and device fabrication. A new layer of diamond is thus grown homoepitaxially on the top surface using plasma-enhanced chemical vapor deposition (PECVD). Detailed information on the growth procedure is reported in [152].

To form tin vacancy centers, Sn^{2+} ions were implanted by a commercial vendor, Cutting Edge Ions, into the newly grown diamond layer with an implantation energy of 380 keV and a fluence of $2e^{11}$ ions/cm^2. The Sn-implanted chip was high-vacuum annealed at 800°C for 60 minutes then 1200°C for 60 minutes to promote color center formation, and then tri-acid cleaned to remove any

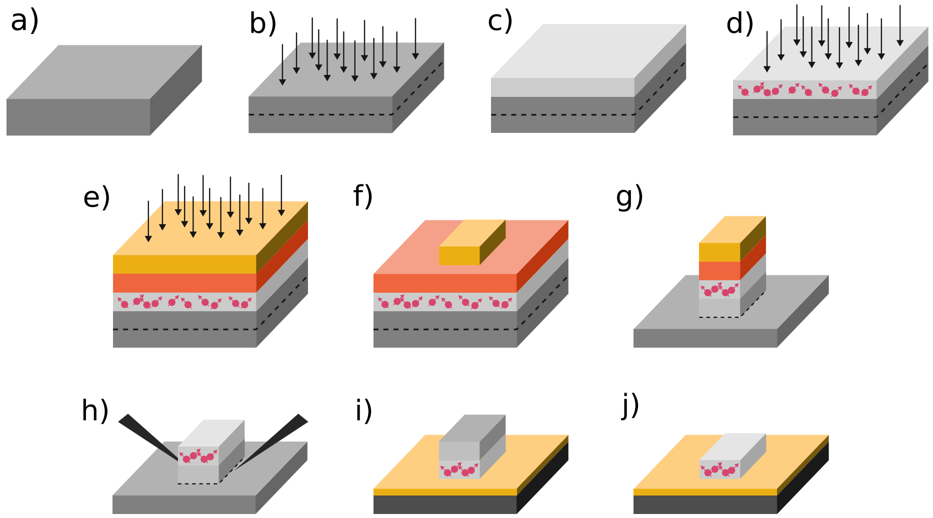

Figure B.1: Schematic of SnV$^-$ implanted thin-film diamond preparation.
The process starts with a bulk electronic grade diamond that is polished to a precise miscut angle (a). The sample is then heavily implanted with He^{2+} ions to form a vertically localized graphitized layer, around 400 nm below the sample surface (b). A pristine layer of single crystalline diamond is overgrown over the implantation damaged layer (c). Sn^{2+} is implanted $\sim$90 nm below the sample surface, and SnV$^-$ centers are formed after high temperature, vacuum annealing (d). Any surface graphitization is removed via a tri-acid clean. A SiN hard mask is then deposited via CVD, and spun with photoresist (e). 200 μm by 200 μm squares are patterned by photolithography; these squares define the final size of each membrane (f). The membranes are defined in the bulk diamond by an anisotropic RIE etch (g). Individual membranes are then released via electrochemical etch (h), and bonded to a Si carrier wafer with HSQ (i). Finally, the film thickness is tuned to 180 nm via RIE etching (j).

surface graphitization that may have developed during the anneal.

Membranes of size $200 \times 200\ \mu m$ are patterned using photolithography and then released from the bulk using an electrochemical etch. The released membranes are then bonded damaged side up to Si carrier pieces via HSQ. Details on membrane exfoliation and transfer are outlined in [88]. The transferred membranes have a starting total thickness of $1 \mu m$ and are thinned to the final desired thickness of 180 nm using reactive ion etching. We show a schematic of the full membrane preparation process in Fig. B.1.

B.1.2 Photonic Crystal Fabrication Procedures

Photonic crystal fabrication begins with the prepared 180 nm thin film membranes bonded to Si. A thin $\sim$ 25 nm Al_2O_3 hard mask is deposited via thermal ALD. The sample is spun with ZEP

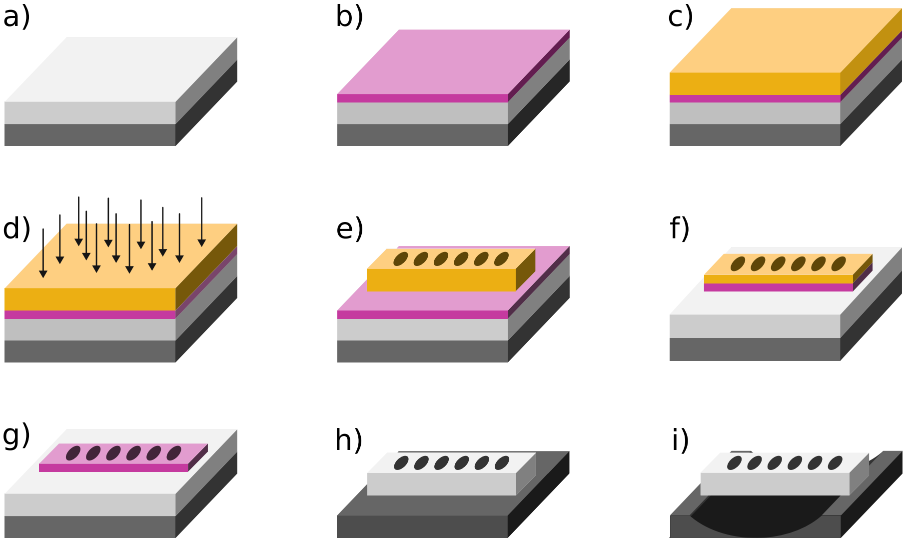

Figure B.2: Schematic of cavity fabrication procedure.
The starting material consists of thin film diamond bonded to a Si handling wafer via HSQ (a). A thin Al_2O_3 had mask is deposited by ALD (b). The sample is spun with ZEP (c) and patterned via ebeam lithography (d, e). The resist pattern is transferred into the hardmask by ICP-RIE etching (f). Any remaining ZEP is then stripped (g), and the pattern transferred into the diamond membrane (g). Lastly, the devices are suspended by HF vapor and XeF_2 dry etching (i).

and then the pattern exposed via e-beam lithography. The resist pattern is transferred into the hardmask with a BCl_3 chemistry ICP etch, and subsequently transferred into the diamond via a Cl_2O_2/O_2 2-step, cyclical ICP etch. The final devices are then released via HF and XeF_2 vapor dry etches. We show this process schematically in Fig. B.2.

B.1.3 Cavity Fabrication Yield and Fidelity

To account for fabrication uncertainties, the cavity lattice spacing was swept from 180 nm to 210 nm, in steps of 2.5 nm, for a total of 13 device designs. All other design parameters (beam width, hole diameter, cavity lattice tapering factor) were kept constant. From FDTD simulations, we expect resonance wavelengths to correspondingly vary from ∼575 nm to ∼684 nm, in steps of ∼4 nm for each lattice spacing step. In Fig B.4, we survey all devices across our sample to evaluate our fabrication yield and fidelity. Due to fabrication variation, we do not observe a clear trend between device lattice spacing and resonance wavelength. Quality factors seem to demonstrate a very slight increase with increased lattice spacings. We also note that we were unable to find any resonances for devices with the lowest four lattice spacings, ranging from 180 nm to 187.5 nm, most likely due to the overetching of cavity holes.

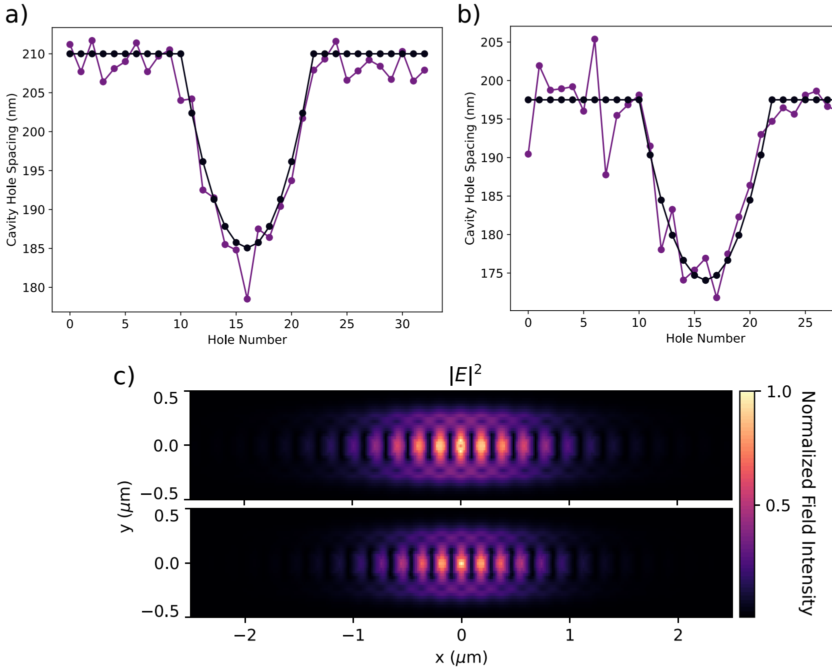

Figure B.3: Comparison of cavity lattice spacings.
(a) Lattice spacing deviations for the parallel device. On average the cavity holes deviated by 2.013 ± 1 nm from designed positions. **(b)** Lattice spacing deviations for the angled device. Cavity holes deviated by 2.796 ± 3 nm from designed positions. **(c)** Simulated normalized electric field inside the cavity region of the parallel device (top) and angled device (bottom).

We evaluated the fabrication fidelity in detail for the two devices of study in the manuscript. Using Genisys ProSEM software, we analyze the tapered lattice spacings of the cavity holes (Fig. B.3(a,b)). For the parallel device, we calculate a 2.013 ± 1 nm deviation from designed lattice spacings; for the angled device, we calculate 2.796 ± 3 nm deviation from designed spacings. Furthermore, we determine our device etch sidewall angle by fitting to both the top and bottom of the extracted beam width sigmoid. For the parallel device, we determine top (bottom) beam widths of 292.6 ± 15 nm (358.6 ± 14 nm); for the angled cavity, we extract 304.9 ± 2 nm (337.3 ± 13 nm). Given a consistent membrane thickness of 180 nm, we therefore determine sidewall angles of 10.389° and 5.143°, respectively, which are included in the simulations.

B.2 Characterization Setup

Here we describe the optical setup used for device and emitter studies (Fig. B.5). The optical setup consists of two separate access arms, referred to in the manuscript as the ‘PL’ and ‘cross polarized’ paths. Access between the two paths are controlled via a motorized mirror (Thorlabs, MFF101).

The sample is housed in a Montana Instruments Cryostation s50 at 5K, and positioned via a tripe Attocube piezo stack (X101/Z100). The sample is addressed with a 100 μm working distance, 100x magnification objective (Zeiss, EC Epiplan-NEOFLUOR 100x/0.9), which is mounted in a heater cryo-objective housing. The 4f confocal scanning microscope is constructed via a pair of 300 mm lenses(Thorlabs, AC254-300-A) and a galvo mirror (Newport, FSM-300-01). Polarization control is provided by the HWP (Thorlabs, AHWP10M-600).

In the cross polarized path, polarization filtering is provided by a polarizing beam splitter (Thorlabs, CCM1-PBS251). In the horizontally polarized collection path, the free space beam is coupled into a single mode (SM) fiber. In the horizontally polarized excitation arm, green and red wavelength splitting is achieved through a short-pass dichroic beamsplitter (Semrock, TSP01-561). The red excitation arm provides either resonant laser (Toptica, 1240 nm DL Pro, doubled via ADVR, frequency doubler) or broadband supercontinuum (superK, EVO EUL-10) light, coupled through a SM fiber. A Thorlabs, LP520-SF40 green diode laser is used for above band excitation. A HWP (Thorlabs, AHWP10M-600) and filter wheel is used to optimize and control power delivery, respectively.

In the PL path, we split green and red with via a longpass dicrhoic beamsplitter (Semrock, DMLP550). Subsequently, we split ZPL and PSB via a shortpass dichroics (Semrock, FF625-SDi01). Pulsed, 520 nm excitation is provided by a Thorlabs, GSL52A laser. Either resonant excitation or signal can be launched or collected from the ZPL path.

Collected signal is either routed to single photon counting modules (Excelitas, SPCM-AQRH-24) or a hybrid spectrometer (Acton, SpectraPro 2750 gratings and Andor, iDus416 CCD). For lifetime measurements, the parallel device lifetimes were collected on a Picoquant, Picoharp 300, while the angled device lifetimes were collected on a Swabian, Timetagger Ultra. Pulse sequences

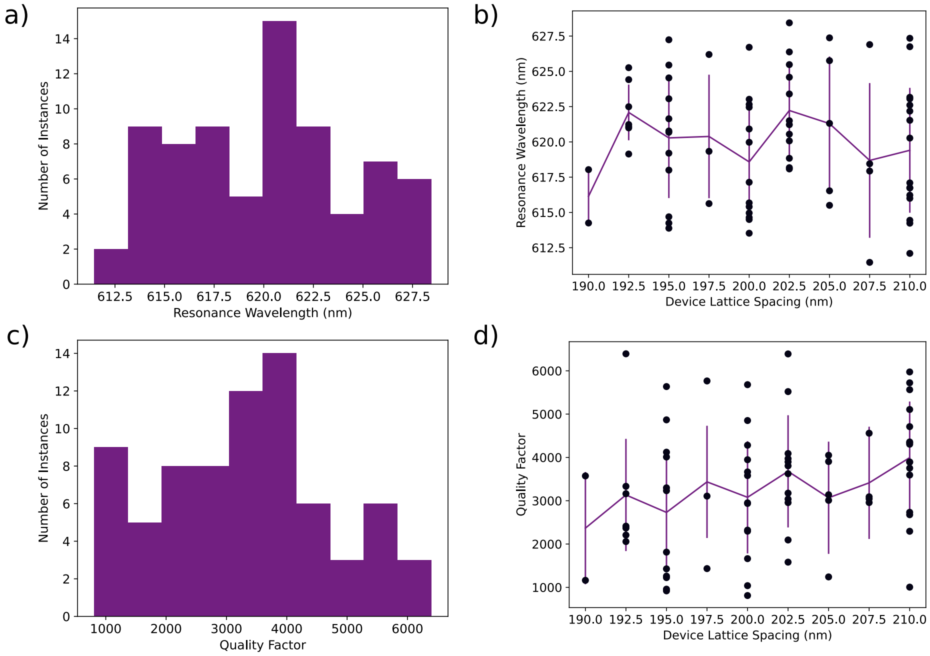

Figure B.4: Summary of cavity fabrication yield across the sample.
(a) Histogram of resonance wavelengths for devices. Across all identified resonances, the average resonance wavelength is 620±4 nm. **(b)** Resonance wavelengths of all devices, summarized by the device lattice spacing. The black markers are data points from individual devices, while the purple line and errorbars indicate the average and standard deviation of of resonances wavelengths for devices of specific lattice spacings. From simulation we expect resonance wavelengths to red shift with increasing cavity lattice spacing; however, we do not observe a clear trend across our sample due to fabrication infidelities. **(c)** Histogram of quality factors for devices. Across all identified resonances, the average quality factor is 3335±1428. **(d)** Quality factors of all devices, summarized by the device lattice spacing.The black markers are data points from individual devices, while the purple line and errorbars indicate the average and standard deviation of of quality factors for devices of specific lattice spacings. Quality factors are expected to remain roughly constant across all device designs. For our sample, quality factor very slightly increases with increased lattice spacings.

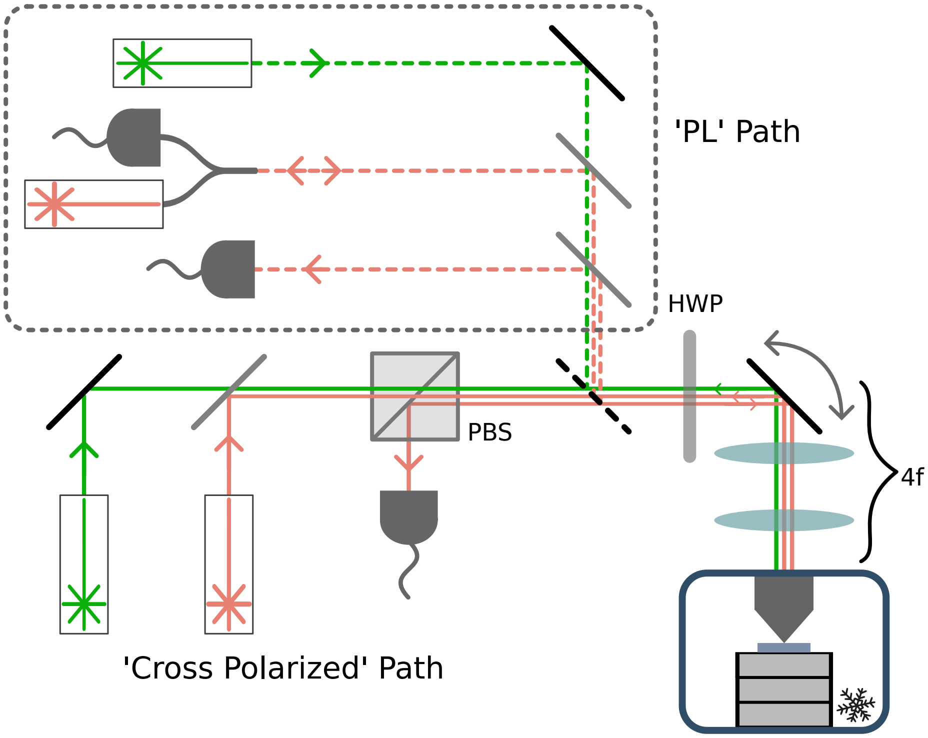

Figure B.5: Schematic of the measurement setup.
The optical setup primarily consists of a home built, 4f confocal microscope with scanning enabled by a galvo mirror (4f). A half wave plate (HWP) is inserted right before the galvo mirror, allowing for simultaneous polarization rotation of all excitation and collection paths. The optical setup incorporates two discrete optical paths, referred to in this manuscript as the 'PL' and the 'cross polarized' paths. Access to either of these two paths are controlled via a flip mirror (dashed diagonal line). In the cross polarized path, the excitation is horizontally polarized, and collection vertically polarized, with the two paths mixed via a PSB. Green diode and broadband supercontinuum excitation are separately fed into the optics setup, with the two paths mixed via a shortpass dichroic beamsplitter. For the PL path, collection is first split between green and red via a longpass diocrhoic beamsplitter, and then further split between ZPL and PSB via a shortpass dichroic beamsplitter. When addressing emitters resonantly, the resonant laser is launched from the ZPL collection fiber coupler.

are programmed and applied by a Swabian, Pulse Streamer 8/2. Pulsing and attenuation of the resonant excitation laser is provided by a G&H, Fiber-Q 633 nm AOM.

Fiber fluorescence from the green excitation sources are cleaned up with Thorlabs, FBH520-10 520/10 nm bandpass filters. Green scattering is further filtered from collection paths via Semrock, BLP01-594R 594 nm longpass filters. ZPL signal is isolated through Semrock, FBP01-620/14 620/14 nm bandpass filters. Filtering for isolating single SnV^- transition lines was achieved using a custom ordered Rapid Spectral Solutions, 622/0.3 nm bandpass filter, designed to have ~ 5 nm of tuning range.

B.3 Resonant Color Center Addressing

Prior to patterning photonic devices, optical characterization was performed to verify formation of color centers in the thin film material. Using 4f confocal microscopy, 2D PL spatial maps were obtained using an above-resonant (green, 520 nm) diode laser and bright spots probed with spectroscopy (Fig. B.6(a)). From Fig. B.6(b), the large density of SnV^-s formed is evident from the PL spectra. This high emitter density is also evident when resonantly addressing the SnV^- candidates. Within ~40 GHz of laser scanning range, we can address on the order of 3-4 color centers (Fig. B.6(d)).

To study the coherence of these color centers, we perform PLE spectroscopy via the PL optical path. We excite the SnV^- with alternating pulsed green and red excitation; SPCM collection is gated with red excitation to reduce signal background. The full pulse sequence is 20 μs, with 4 μs of green excitation, 4 μs of offset, and 12 μs of red excitation and SPCM collection. Pulsing for the green diode is provided by direct modulation of the laser diode, while pulsing for the red is provided by an AOM. The red laser is scanned across ~40 GHz with a frequency of 0.2 Hz. We are also able to identify SnV^- transitions with down to a ~320 MHz linewidth, stable for ~30 minutes (Fig. B.6(e)). Estimating from the off-resonance lifetimes as reported in Section 3.2.2, the Fourier limit linewidth would be on the order of 100 MHz. However, color centers of higher coherence in both bulk and thin-film diamond have been reported [28, 51]. We attribute our measured linewidth to insufficient optimization of PLE experimental parameters, lack of an exhaustive survey of emitters, and the high Sn^{2+}implantation density.

Post-device fabrication, we first attempt PLE for the emitter of study in the parallel device. Although the PLE is consistent over ~30 minutes, the emitter demonstrates significant linewidth broadening, with an averaged linewidth of 15.382 pm (Fig. B.7(a,d)). We also probe a secondary emitter in the device which is much more weakly coupled to the cavity mode. This emitter instead demonstrates an averaged linewdith of 1.368 pm; the PLE signal is stable over ~30 minutes. The further linewidth broadening of the emitters in fabricated devices likely stemmed from the proximity

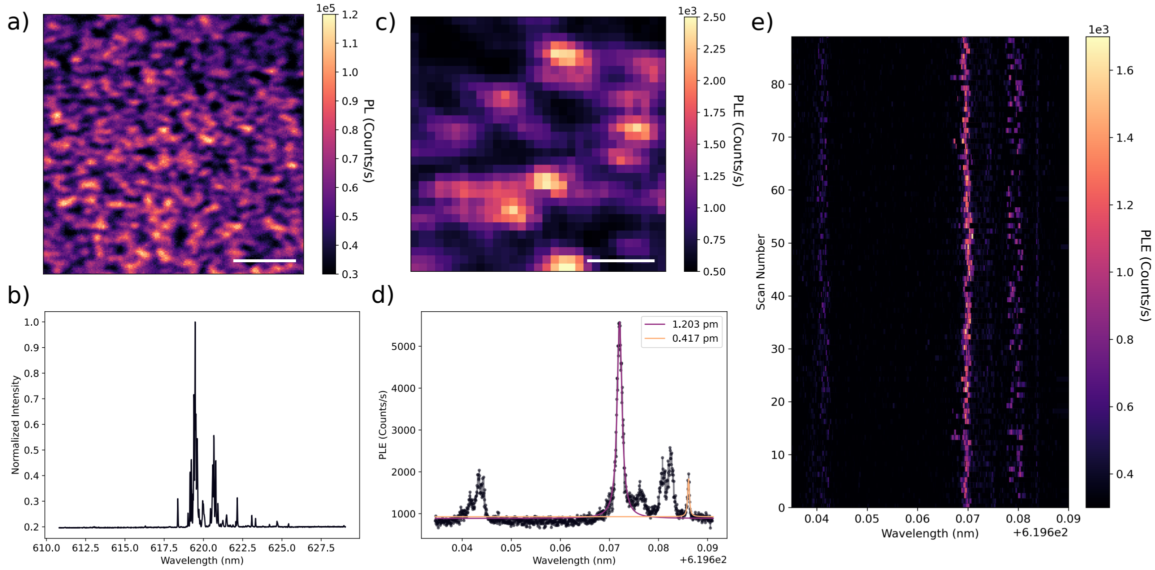

Figure B.6: Color center characterization in thin film, pre device fabrication. **(a)** PL confocal scan of the thin film pre device fabrication. The density of bright spots indicates the larger number of SnV$^-$s formed during implantation. The scale bar indicates 3μm. **(b)** Representative PL spectrum for a probed emitter cluster, demonstrating SnV$^-$ formation density. **(c)** PLE confocal scan. A full PLE scan is taken and count rates summed per pixel of the 2D spatial map. All emitters which show up are addressable within the laser scanning range of ~40 GHz. The scale bar indicates 1μm. **(d)** Averaged PLE. Two representative transitions are fit with a Lorentzian model to estimate the linewidths. The more prominent transition demonstrates a 1.236 pm or ~1 GHz linewidth. The other transition demonstrates a 0.417 pm or ~320 MHz linewidth, around 3 times larger that our estimated Fourier limit of ~100 MHz. **(e)** PLE traces over 30 minutes. The stability of the PLE indicates prolonged SnV$^-$ coherence in the thin film.

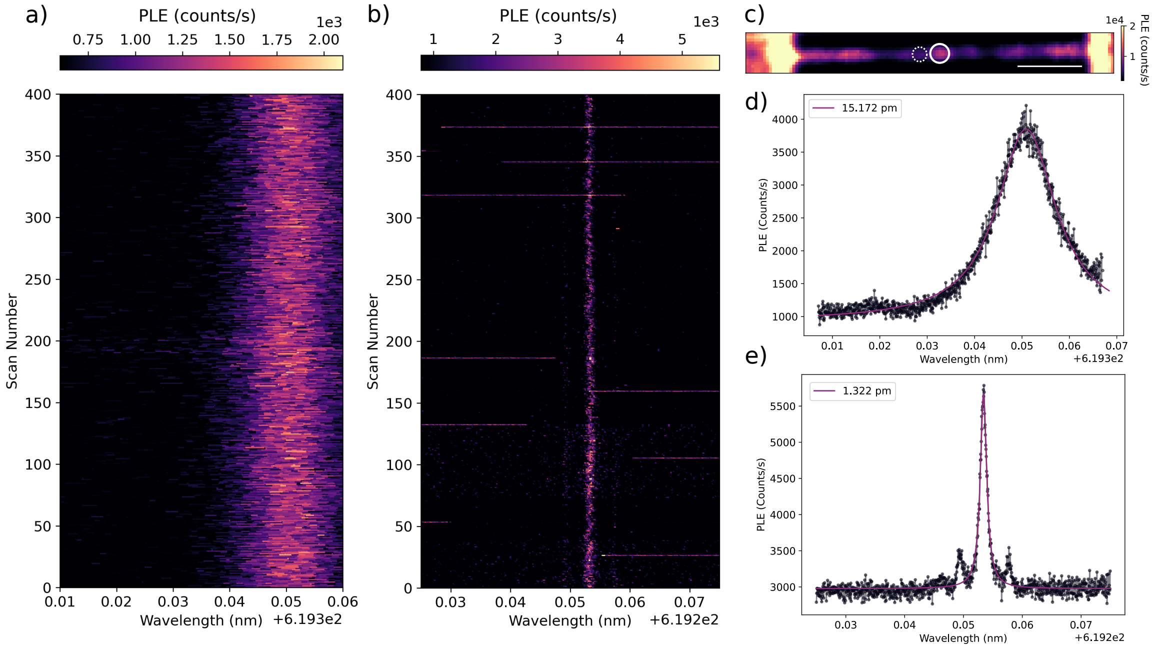

Figure B.7: Resonant color center addressing in fabricated devices.
(a) PLE traces for ∼30 minutes on the color center of focus in the parallel device. **(b)** PLE traces for ∼30 minutes for a secondary emitter in the parallel device. **(c)** PLE confocal scan of the parallel device. The main emitter of study in this manuscript is indicated by the solid circle, while the dashed circle notates the secondary emitter of study. **(d)** Averaged PLE of the traces from (a). A Lorentzian fit yields a linewidth of 15.382 pm. **(e)** Averaged PLE of the traces from (b). A Lorentzian fit yields a 1.386 pm linewidth. We note that the side lobes of the mean PLE peak feature was due to laser instability and multimodedness.

of etched surfaces. To mitigate these effects, inspiration can be taken from efforts to improve near-surface NV coherence via surface passivation or chemical termination [153, 154].

Appendix C

Supplement for ‘Heterogeneous Integration of Diamond Color Centers and Thin-Film Lithium Niobate’

C.1 Additional Methods and Calibrations

The sample was maintained at 5 K in a Montana Instruments Cryostation s50. We position the sample using a three-axis stage consisting of an Attocube piezo stack (X101/Z100). We use a heated cryo-objective inside the Cryostation to address the sample. For grating coupler transmission measurements in Fig. 3, light couples in and out of the path via single-mode fibers. These are coupled into the path using fiber couplers with f=8.00 mm aspheric lenses (Thorlabs, C240TMD-B). For confocal excitation and collection, we again couple light into the path via fiber couplers, installed with f=18.4 mm aspheric lenses (Thorlabs, C280TMD-B). Our input and output collection fibers for all paths are 630 nm polarization-maintaining single mode fibers (Thorlabs, P3-630PM-FC-2). The excitation laser light (MSquared, Solstis) is first routed through a 3-paddle polarization controller (Thorlabs, FPC560) fitted with a single mode 630 nm fiber (Thorlabs, P3-630Y-FC-2). From here it is passed through a 99:1 single mode fiber beamsplitter (Thorlabs, TW670R1A2), which is used to monitor input power.

We filter extraneous fiber fluorescence on the excitation path with a 711/25 nm (Semrock Brightline 711/25) bandpass filter and on all collection paths with 740/13 nm (Semrock Brightline 740/13) bandpass filters.

Our confocal excitation/collection path consists of a 4f lens setup containing a fast steering mirror (Newport, FSM-300-01) and two f=300 mm achromatic doublets (Thorlabs, AC254-300-A) and are combined via a 720 nm-shortpass dichroic beamsplitter (Semrock, FF720-SDi01-25x36). The confocal and coupler transmission paths are mixed via another, identical 720nm - shortpass dichroic beamsplitter. These beamsplitters exhibits a strongly polarization-dependent transmission at the non-resonant excitation wavelength of 710 nm. To compensate for polarization misalignment between the two dichroics, we use a 400-800 nm half-wave plate (Thorlabs, AHWP10M-600) to optimize power delivery. Final polarization control before the Montana window is achieved by a 690-1200 nm half-wave plate (Thorlabs, AQWP05M-980). All mirrors in the optical setup are broadband silver mirrors (Thorlabs, PF10-03-P01). Color center emitter signal is either routed to avalanche photodiode single photon counting modules (Excelitas, SPCM-AQRH-24) or a hybrid spectrometer with Acton, SpectraPro 2750 gratings and an Andor, iDus416 CCD. Power measurements are performed with photodiode sensors (Thorlabs, S120C) moved between parts of the optical path.

For $g^{(2)}$ autocorrelation measurements collected via the confocal channel, the signal is routed to a 50:50 fiber beamsplitter. Each arm is subsequently routed to a separate SPCM unit. For coupler-collected autocorrelation measurements, the output from each LN grating coupler is directly routed to separate SPCM, utilizing the TFLN waveguide intrinsically as a beamsplitter. SPCM outputs are then routed to a Picoharp 300 timetagging system. For spectrometer measurements, we route the optical signal through a 750/10 nm bandpass (Thorlabs FBH750-10) and a 750 nm shortpass (Thorlabs FES0750) in series, thereby filtering out the specific SiV- optical transitions we would like to measure. We tilt both filters to tune the filtering range and effectively isolate a single transition for PL detection.

From manufacturer-provided specifications of the cryostat, cryo-objective, and mirrors, we assume a 95% transmission of the cryostat window, 90% through the cryo-objective, and 98% reflection for each silver mirror. Lenses are assumed to have a transmission of 99.75% each. SPCMs are assumed to have 65% efficiency at operating wavelengths.

C.2 Diamond Nanobeam Fabrication

We begin sample preparation with a 2 by 2 mm^2 electronic grade diamond from Element 6. The sample is cleaned with a refluxing triacid mixture, followed by soaking in acetone and isopropanol (IPA). We remove 500 nm of the strained diamond surface with an anisotropic, oxygen plasma etch. We incorporate SiV centers by growing back 200 nm of diamond, while placing a silicon substrate alongside the diamond in the CVD chamber.

A hardmask consisting of 200 nm of $\mathrm{Si}_x\mathrm{N}_y$ is then deposited via low pressure CVD. The nanobeam pattern is defined in ZEP 520A positive ebeam resist with a 100keV ebeam writer (JEOL 6300) and developed in a three step process (ortho-xylene, MIBK:IPA 1:3, and IPA). We use an anisotropic etch with SF_6, CH_4, and N_2 to transfer the pattern from the resist to the hardmask, which is subsequently transferred into diamond with a 500 nm anisotropic oxygen plasma etch. Approximately 25 nm of Al_2O_3 is then deposited with atomic layer deposition (ALD) to protect the device sidewalls. A breakthrough etch of the alumina is performed with an ICP metal etcher tool (Plasma Therm Versaline LL ICP Metal Etcher). An additional 200 nm anisotropic diamond etch then exposes material, enabling continuation of a quasi-isotropic etch.

The quasi-isotropic etch process is performed at an elevated temperature of 300 C using high density oxygen plasma in an ICP dielectric etch tool (Plasma Therm Versaline LL ICP Dielectric Etcher). We periodically remove the sample from the etcher and image with an SEM in order to monitor the progress of the undercut. Upon completion, we strip the masking layers with an HF soak. We then rinse the sample in water followed by IPA and allow it to dry by letting the solvent evaporate gradually.

C.3 Pick and Place Details

In Fig. **??**, we present a photo of the pick and place setup. In order to monitor the transfer process *in situ*, we use a long working distance object with WD$\sim$ 30mm (Mitutoyo 100x M Plan APO NIR Objective - 378-826-15).

One needle is a piezo-controlled (Thorlabs PCS-6300CL) tungsten "cat whisker" needles with $\sim 70\,\text{nm}$ tip radius (Ted Pella 99-15864) for initial break-off picking. To assist with the mechanical break-off process, some waveguides are detached from their diamond holding structures on the diamond substrate through a fixed ion beam (FIB) cut.

In addition to a fine-controlled needle, a secondary cat whisker needle is mounted on a micrometer-controlled stage to provide an extra point of contact that enables mid-transfer control and adjustment of the diamond waveguide. Orientation prior to attachment of the diamond waveguide is optimized with the two needles and a rotation stage. The waveguide is transferred to the fine-controlled needle and lowered to the LN substrate. After making contact with the LN gratings, the diamond attaches electrostatically more strongly to the LN than to the needle, and the needle is further pulled down into an etched trench between the LN gratings as it detaches from the diamond. Further fine position and alignment adjustment can be done with the needle while taking care not to apply force sufficient to break the diamond from LN.

C.4 Efficiency Calculations

We indicate the taper facet transfer efficiency to be η_{taper}, the grating coupler efficiency to be η_{coupler}, and all other optical losses lumped together to be η_{losses}. Therefore, our measured transmissions (T)

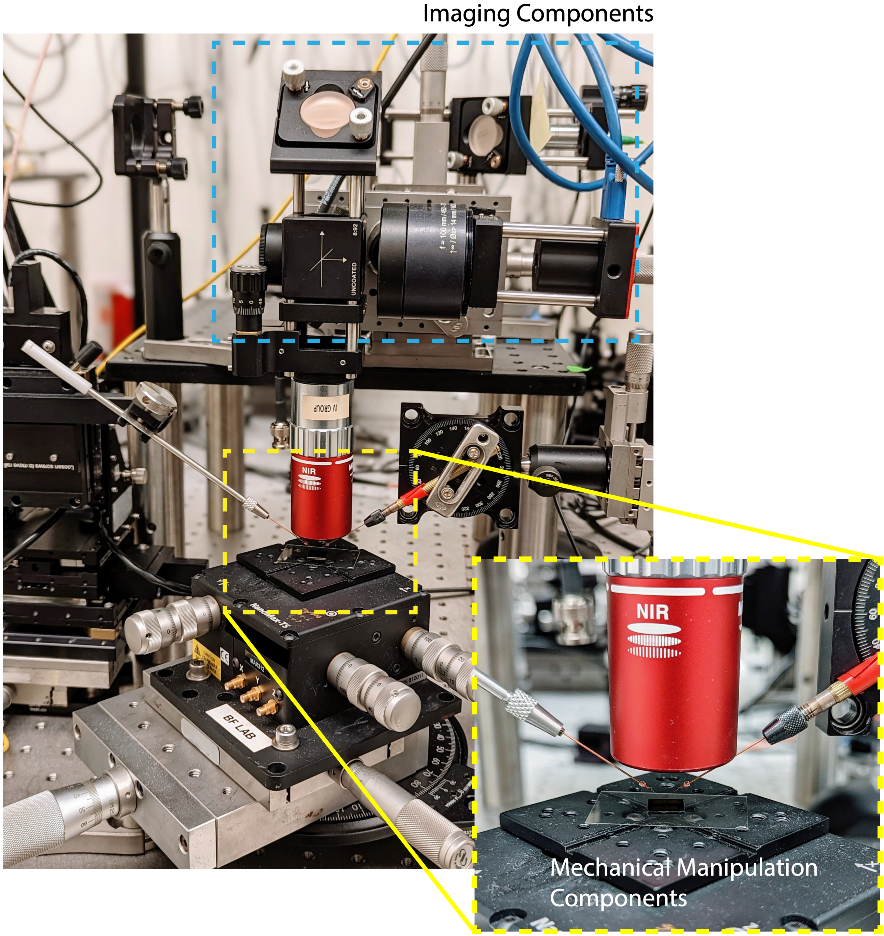

Figure C.1: Photo of pick and place setup.
The mechanical manipulation components are highlighted by the yellow box, with the inset showing the components in more detail. The blue box indicates the imaging optic components.

can be expressed as:

$$T = \eta_{\text{taper1}}\eta_{\text{taper2}}\eta_{\text{coupler1}}\eta_{\text{coupler2}}\eta_{\text{losses}} \tag{C.1}$$

We then make the reasonable assumption:

$$\eta_{\text{taper1}} \simeq \eta_{\text{taper2}} = \eta_{\text{taper}} \tag{C.2}$$

We lump the grating coupler input and output efficiencies into a single term (see supplemental section ’Grating Coupler Simulations’ for a discussion of the expected in- and out-coupling efficiencies):

$$\eta_{\text{coupler1}}\eta_{\text{coupler2}} = \eta_{\text{coupler}} \tag{C.3}$$

Which simplifies our transmission to:

$$T \simeq \eta_{\text{taper}}^2\eta_{\text{coupler}}\eta_{\text{losses}} \tag{C.4}$$

We now make the approximation that the grating coupler efficiencies are roughly constant across the chip and therefore, $\eta_{\text{coupler,integrated}} \simeq \eta_{\text{coupler,control}}$. This assumption is supported by the SEM measurements, presented in the supplemental section ’SEM Imaging of Device.’ Additionally, as the two measurements were using identical optical paths, both are affected by the same η_{losses}. Given that the control device consists of a continuous TFLN waveguide, $\eta_{\text{taper,control}} = 1$. Therefore, by comparing transmissions:

$$T_{\text{integrated}}/T_{\text{control}} \simeq \eta_{\text{taper,integrated}}^2 \tag{C.5}$$

$$\eta_{\text{taper,integrated}} \simeq \sqrt{T_{\text{integrated}}/T_{\text{control}}} \tag{C.6}$$

C.5 Measurement Calibrations

We fabricated two control devices for calibrating grating coupler efficiency on the TFLN sample consisting of TFLN grating couplers connected by constant-width waveguides. Transmission statistics are taken multiple times over two months for all control devices as well as the heterogeneously integrated device. Transmission values are relatively consistent across multiple measurements, with any variance attributed to alignment or thermal fluctuation, as well as gradual condensation in the cryosystem. For measurements performed in the main text, we use connected device “Control 1” as the control device. Connected device “Control 2” was damaged during early measurements and could not be used to calibrate transmission measurements reliably. By measuring both devices, we can estimate the total grating coupler in-to-out-coupling transmission at 737 nm to range between 2.69% and 4.92%, for an average of $3.55 \pm 0.44\%$ (we assume negligible loss in the waveguide). This

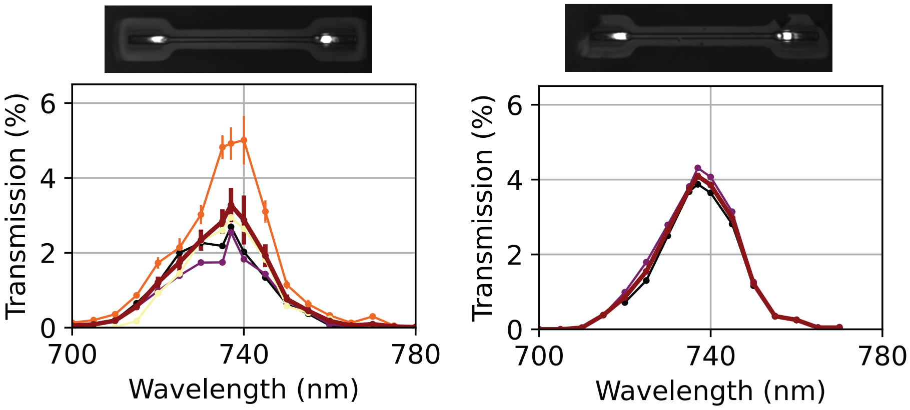

Figure C.2: Transmission measurements for control devices.
Transmission measurements for the 2 control devices present on the TFLN chip, referred to as “Control 1” (left) and “Control 2” (right). Different thin-line transmission traces are data from separate measurements, while the bold overlaid trace is the average across all measurements. We present data from multiple separate characterizations, taken over 2 months. Error bars indicate one standard deviation. For some data points, error bars are smaller than data markers. White light illuminated images of each device and its visible transmission are displayed above each transmission spectrum.

is pictured in Fig. C.2. These values reasonably match the simulated in-to-out-coupling efficiencies of the grating couplers simulated via FDTD in the section ’Grating Coupler Simulations.’

From these transmission measurements, we determine the taper efficiency of a second fully-integrated device (different from that presented in the main text) to be 84.1 ± 1.6% per taper facet at 737 nm, demonstrating the repeatability of our pick and place transfer procedure. These measurements are illustrated in Fig. C.3.

We additionally verify the operation of our devices at room temperature by performing identical transmission measurements as those reported in the main text. Room temperature measurements are performed with a separate, greatly simplified transmission setup. To evaluate variability between devices, calibrations at room temperature are performed with 2 distinct control devices, the first being“Control 1” and the other which is further away spatially from the integrated device and therefore not used for our reported results, henceforth referred to as “Control A”.

For “Device 1”, using the “Control 1”, we determine an adiabatic taper efficiency of 99.8 ± 14.1% (94.4 ± 17.5%). For “Device 2” we observe at room temperature a taper efficiency of 65.5 ± 9.8% (61.2±9.8%). Both of these determined efficiencies are comparable to that observed at 5K, indicating that our devices are robust towards large fluctuations in temperature and ambient conditions. These measurements are illustrated in Fig C.4.

From both cryo and room temperature measurements, we verify the validity of our calibration methods. By comparing to control devices, we are able to extract away all optical losses and greatly

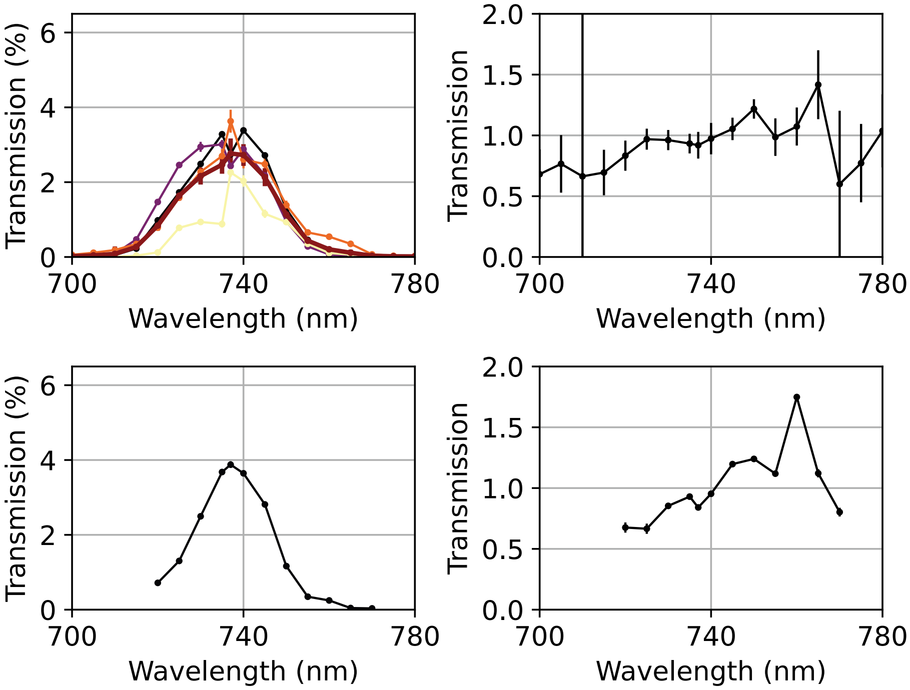

Figure C.3: Statistical evaluation of transmission measurements.
Transmission data for the device reported in the manuscript ("Device 1", top), and from an additional integrated device ("Device 2", bottom) are presented. Transmission for "Device 1" was taken 4 separate times, over 2 months. For "Device 1", the thin transmission traces indicate data for each separate measurement, while the bold trace is the average across all measurements (left). The averaged "Device 1" transmission is normalized to the average transmission for "Control 1", generating the adiabatic taper efficiency response across wavelengths (right). Error bars for this measurement indicate one standard deviation. Given very small transmission values at the extremities of the grating response for both integrated and control devices, taper efficiency error bars are observed to increase dramatically at these wavelengths. A similar measurement is taken for "Device 2."

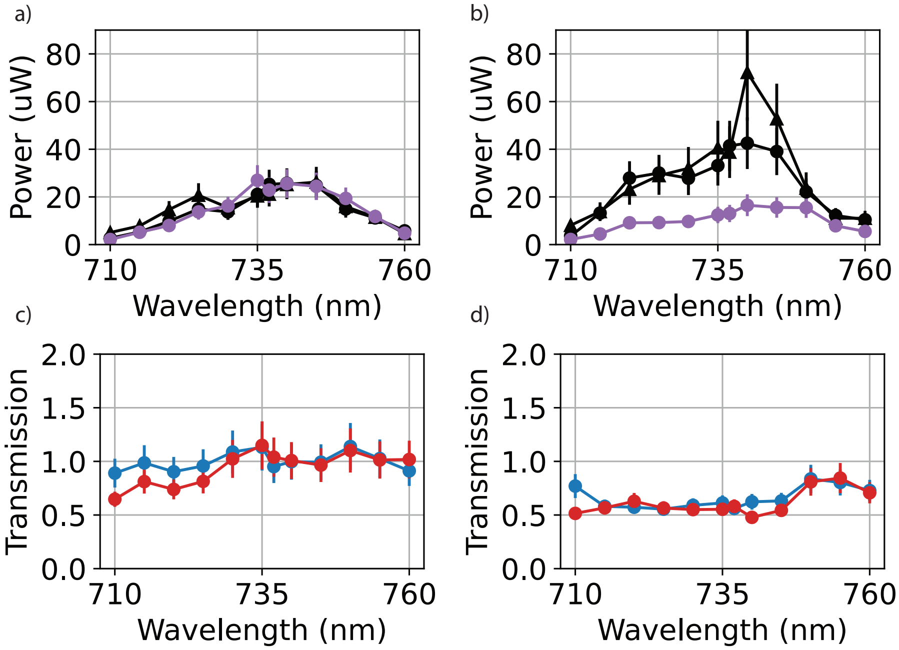

Figure C.4: Room temperature transmission measurements.
Raw transmitted powers for "Device 1" (a) and "Device 2" (b). Black curves are for the control devices used. Circle markers indicate measurements for "Control 1" and a separate control device, "Control A" not presented in Fig. C.4. This other control device is located spatially separated from the integrated devices and therefore not used for measurements in the main text, but provides information about the uniformity of device performance across the chip. Purple is for the integrated device. Taper efficiencies are presented for "Device 1" (c) and "Device 2" (d). The blue curve indicates taper efficiencies determined with the former device, and red with the latter device. Error bars for all panels indicate one standard deviation.

reduce the number of component-by-component calibrations required for the setup. Each of these calibration steps would introduce a sizable amount of uncertainty depending on alignment details, leading ultimately to greater error in our reported results.

C.6 Emitter-Nanobeam Coupling Simulations

$\mathcal{NB}$: As a subtlety that was identified after the fact [1], the FDTD simulations were set up with a slight error such that the simulation region did not fully terminate the simulated waveguide, which causes some small reflection at the end of the facets. If instead, the simulation region is adjusted for proper termination, the coupling efficiency at each waveguide end is symmetric, regardless of emitter positioning and angular alignment. This however does not significantly change the discussion presented in this section. Instead, it simply informs us that there is some amount of reflection in our system, either stemming from the non-unity transfer efficiency per taper facet or the TFLN grating couplers.

To verify the validity of our confocal versus coupler collection channel count rates, we use Lumerical FDTD to perform simulated sweeps of dipole emitter orientation and position while monitoring transmission through the different collection channels. We simulate a nanobeam with 300 nm width and 200 nm thickness, modeling the single mode region of our tapered diamond devices. We place a monitor at the end of each nanobeam to observe transmission coupled into the TFLN waveguide, and a monitor directly above the emitter to collect out-of-plane, confocal scattering.

To investigate the effects of dipole orientation, we sweep the polar angle, θ, of the dipole from 50°to 60°to account for slight crystalline misalignment out of plane. We sweep the azimuthal angle, ϕ, between 0°and 180°, accounting for misalignment stemming from both the cut of the bulk crystal and lithography. For $\langle 100\rangle$ cut diamond with devices perfectly aligned to the cubic axes, we expect both θ and ϕ to be $\sim 55°$, given diamond's tetrahedral structure. Taking slices at both $\theta \approx 55°$and $\phi \approx 55°$and summing the transmitted power at both ends of the nanobeam, we see that in-nanobeam transmission (coupler channels) is greater than out-of-plane confocal collection, as shown in Fig. C.5 [2].

For sweeps of dipole position in the nanobeam cross-section, we maintain $\phi = 55°$. We vary θ between 0°and 90°only, given these two angles correspond to maximum and minimum contrast between confocal and integrated transmission. Again, we observe that integrated collection channels consistently perform equally to or outperform the out-of-plane collection consistently across all emitter positions by nearly 5-fold (Fig. C.6 and Fig C.7). We stress that because of realistic losses from optics and the angular dependence of the collection objective, we see instead an increased

---

[1] Read: during the writing of this thesis

[2] Erratum: for a group-IV color center aligned with the $\langle 111\rangle$ diamond lattice axis, ϕ would be $\approx 45°$. However, our fabrication isn't perfectly aligned with the diamond $\langle 100\rangle$, axis, so a $\approx 5-10°$angular misalignment would not be out of the question.

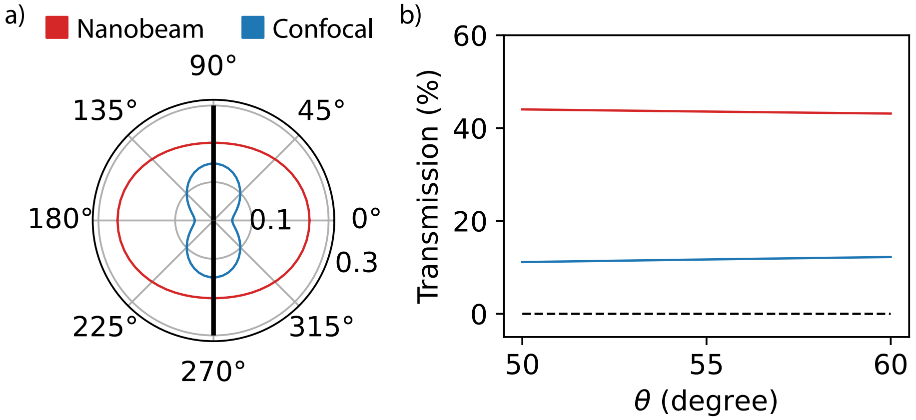

Figure C.5: Angular dipole orientation and nanobeam coupling.
(a) Transmission variance with fixed $\theta \approx 55°$and sweeping full range of ϕ. Red corresponds to transmission collected through integrated channels, and blue confocal. In order to optimize photon extraction through integrated channels, we see that it is ideal to orient our dipole perpendicular to the nanobeam. **(b)** Transmission variance with fixed $\phi \approx 55°$and sweeping full range of θ. A small range of θ is swept to take into account misalignment of cut of starting bulk crystals. We see that such small fluctuations in orientation do not cause great variation in either confocal or integration collection efficiencies, and that integrated collection channels consistently outperform confocal channels by nearly five-fold.

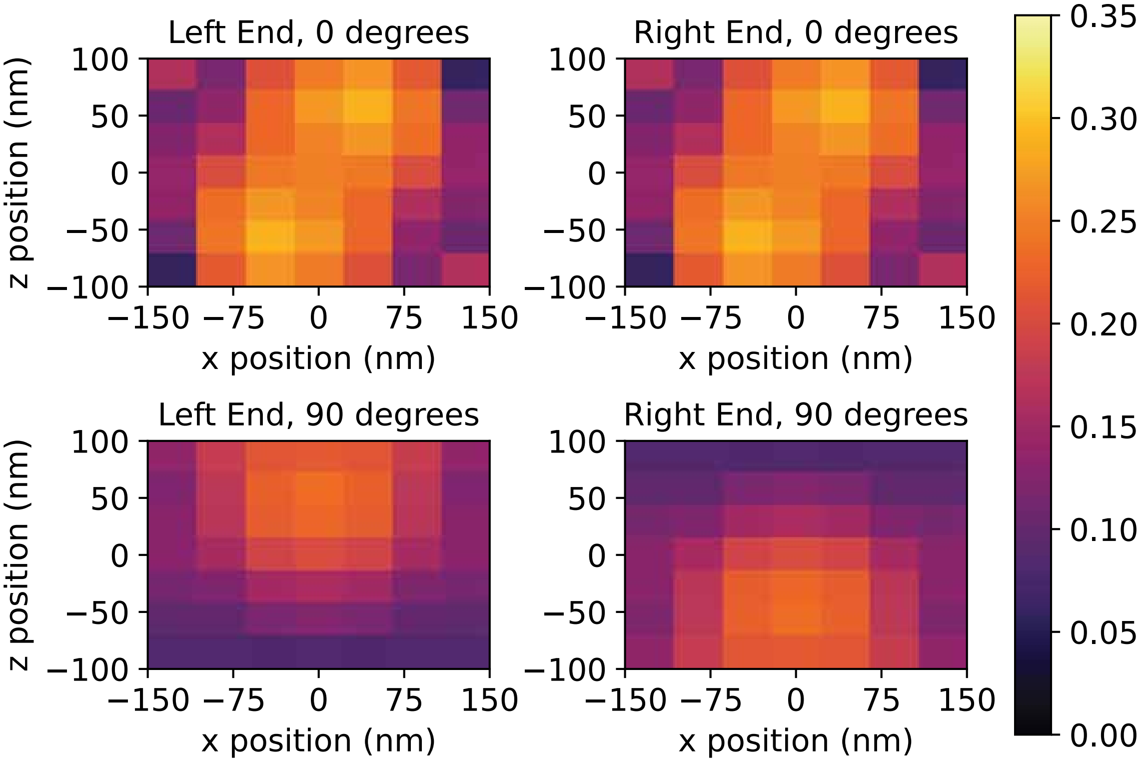

Figure C.6: Transmission efficiency for varied emitter position.
Transmission is simulated for each nanobeam end as emitter position is varied in the device cross-section. Notably, depending on emitter positioning in the nanobeam, we observe an asymmetry in transmission efficiency at each device end.

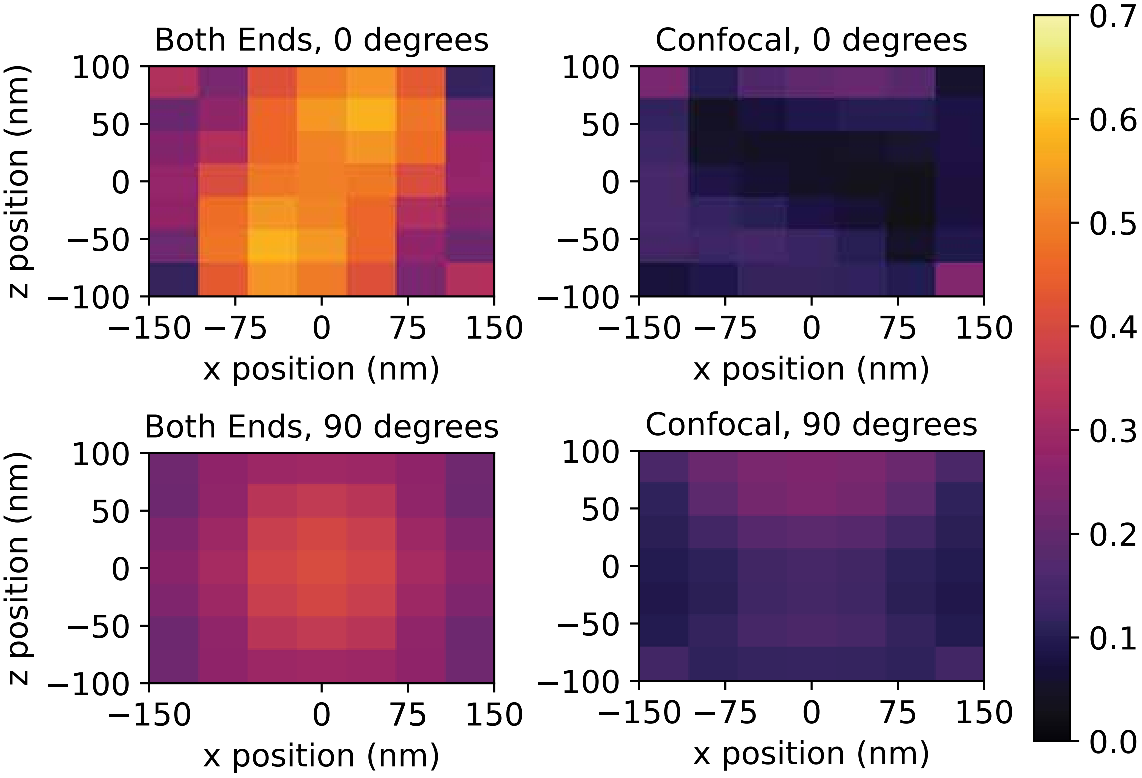

Figure C.7: Transmission efficiency for varied emitter angle
Transmission is simulation as emitter position is varied in the nanobeam cross-section, comparing total signal collected through integrated channels to that confocally. We see that consistently across nearly all emitter positions, the integrated channels demonstrate improved photon collection rates.

10-fold improvement in experimental device demonstration.

C.7 Grating Coupler Simulations

In Fig. C.8, we demonstrate simulated design parameters for our grating couplers. Our couplers are approximately 2 μm wide and 10 μm long with a designed pitch in CAD of 425 nm. The duty cycle is swept from 0.8 to 0.3 to improve coupling bandwidth and reduce reflections from the grating into the waveguide. In practice, our actual devices and grating pitch differ a bit due to fabrication discrepancies from CAD. For these parameters, we simulate an expected out-coupling efficiency from a single-mode source in the waveguide of approximately 50.07%, depicted in Fig. C.8(a). In-coupling of the light is more difficult, due to the multimoded behavior of the TFLN waveguide at 737 nm. Fig. C.8(b) displays a map of the simulated in-coupling efficiency into the waveguide fundamental mode as a function of the incident beam placement and focal plane. For the source placement corresponding to the maximum transmission from free space into the waveguide, we simulate an expected transmission into the fundamental waveguide mode of approximately 25.46%. Multiplying the single-mode input and output efficiencies together indicates that we can expect a single-mode in-to-out coupling through the simulated control device of approximately 12.75%, similar to our demonstrated experimental coupling. The full multimode transmission is expected to be slightly greater, and we expect these numeric results to upper-bound our experimentally measured grating efficiencies.

Importantly, our experimental grating couplers differ from the demonstrated simulations in a few ways, leading to differences in the observed coupling spectra. First, for simplicity, we simulate lithium niobate structures as isotropic with the ordinary refractive index. As the device is cooled, however, the refractive index will shift. Following the results of references [155, 156], we expect a small shift in the lithium niobate bulk refractive index at cold temperatures. While these references suggest only an extremely small shift, we observe in experiment that the grating coupler spectrum actually changes a lot between room temperature and cryogenic measurements. Fig. C.9(a) depicts a set of simulated spectra as the refractive index is swept, demonstrating that the peak grating response red-shifts as the lithium niobate index increases. Furthermore, we observe in Fig. C.9(b) that the simulated out-coupling spectrum of the grating changes dramatically with the duty cycle of the grating. We can therefore expect a shift in the grating coupler spectral response as we adjust our in-coupling and out-coupling alignment to the grating in experiment, or if the fabricated duty cycle differs from the simulated intended design. Lastly, out-scattering from the grating couplers occurs at various angles. If any of these angles are clipped by the optical collection path we would observe a discrepancy between the simulated results and experimental measurements.

For all simulations presented in this section and the main text Fig. 4.1, we use refractive indices for TFLN, diamond, and oxide of 2.26 [157], 2.40 [158], and 1.45 [159], respectively. These are the

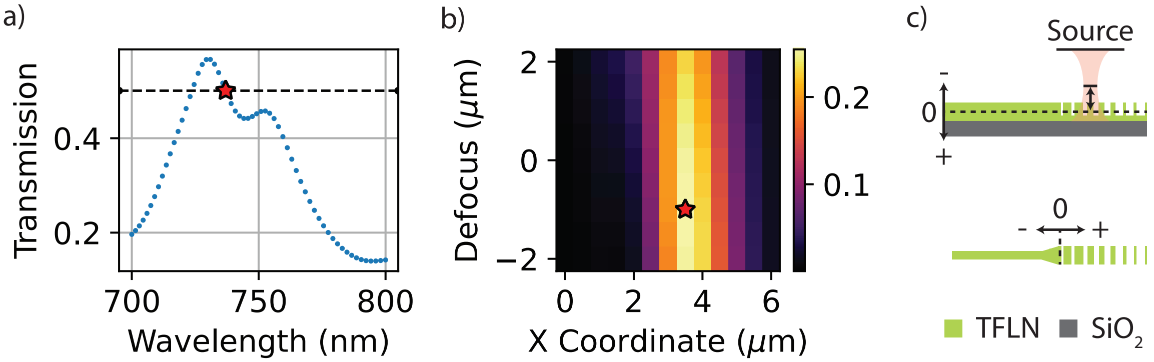

Figure C.8: Simulated grating coupler response with refractive index 2.26. **(a)** Simulated spectrum of the TFLN grating couplers used in the device. The simulation consists of a single-mode source in a waveguide and measures the transmitted power out of the grating into free space. The red star indicates an interpolated datapoint of transmission at 737 nm. **(b)** Simulated map of the single-mode in-coupling efficiency from a Gaussian source into the TFLN waveguide. The “x coordinate” corresponds to position of the beam relative to the start of the grating, while the “defocus” parameter corresponds to vertical position relative to the center of the TFLN stack. The red star indicates the source position and defocus yielding maximum transmission into the waveguide fundamental mode. **(c)** Schematic of the device geometry used in simulation. (Top) Defocus parameter, indicating the distance of the source focus from the middle of the TFLN stack. (Bot) “X Coordinate,” indicating distance of the source focus from the start of the grating.

refractive indices at 737 nm and approximately room temperature.

C.8 Power-Dependent Autocorrelation

Each autocorrelation measurement presented in the main text is extracted from a series of power-dependent g^2 measurements. The full series of measurements are provided here, demonstrating how for both collection schemes, $g^2(0)$ does not fall below 0.5, the single emitter threshold, but still demonstrates predominantly single emitter behavior of the interrogated spot C.10.

C.9 Focus-Dependent PL

We compare the integrated device’s emission into a confocal collection channel to emission into the TFLN waveguide channel by varying the confocal excitation and collection foci and recording the resulting photoluminescence (PL) spectra measured via each collection channel.

For the confocal excitation and collection scheme (C/C configuration), we step the foci in tandem, while localized to the same coordinate and plot the results in Fig. C.11(a). While we observe emerging transitions at different foci, they mostly overlap in the C/C collection, maintaining the

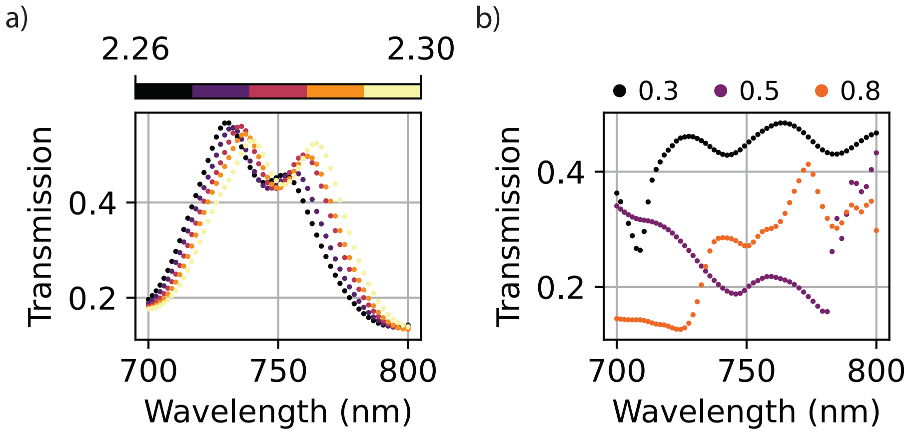

Figure C.9: Simulated grating coupler parameter sweeps.
(a) Simulated spectral response as the refractive index of the TFLN is varied from 2.26 up to 2.30. We observe a red-shift of the peak spectral response. **(b)** Simulated spectral response as the duty cycle is varied between 0.3, 0.5, and 0.8, with TFLN refractive index 2.26. The duty cycle is fixed for the length of the grating coupler. The experimental device has a swept duty cycle.

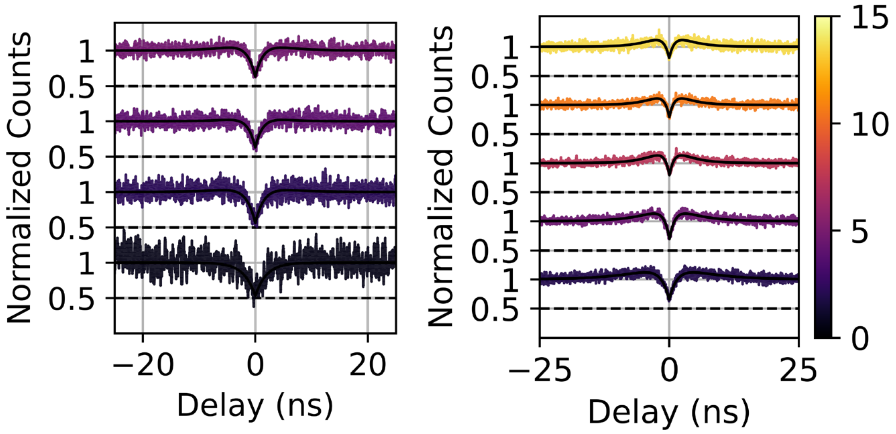

Figure C.10: Power-dependent autocorrelation series for confocal collection (left), and coupler collection (right).
All $g^{(2)}(0)$ dips fail to fall below the 0.5 threshold, marked by a dashed line, which indicates that we are in fact probing a small ensemble of emitters. The color of the curves indicates the power at which they were taken at.

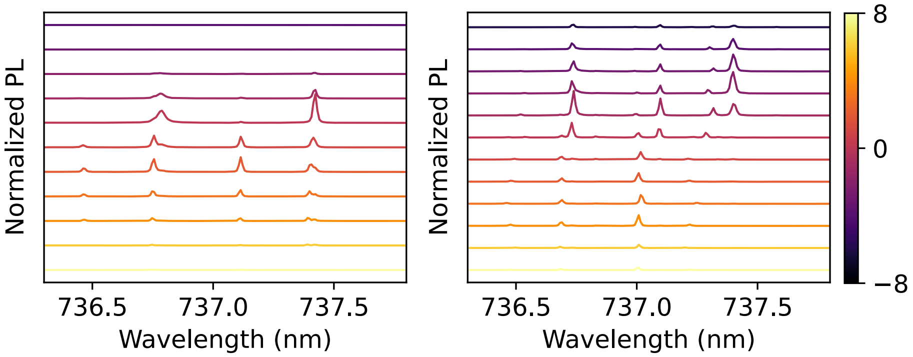

Figure C.11: Focus-dependent PL spectra.
PL spectra obtained in the C/C configuration if displayed on left, and PL spectra obtained in the C/CP configuration, on right. The colorbar indicates the number of rotations of the focal knob that is taken. As the excitation/collection plane is swept, the emitter transitions merge together on the spectrometer for the C/C configuration, appearing as a single emitter signature at certain focal planes. For C/P, we observe the spectral signatures of a greater number of emitters compared to the data for C/C.

appearance of a "single" emitter at multiple focal planes. We predominantly observe a decrease in collected light as the device is moved out of focus.

We repeat this measurement for the confocal excitation with the C/CP configuration. In this configuration, only the confocal excitation plane is stepped, while the collection plane is fixed on the TFLN grating couplers. We plot the results in Fig. C.11(b). Here, we more clearly observe multiple emitter transitions appearing at different foci, including a number not captured at all through confocal channels.

We also collect full PL maps in the X-Y plane at each interrogated focal plane. For each collection configuration, we overlay this data, with the z axis corresponding to focal plane shifts, thereby generating a 3D map of suspected emitter locations. The results, shown in Fig. C.12, further accentuate the differences between the two collection configurations. First, by comparing Fig. C.12(a) and Fig. C.12(b), we observe greater background signal and increased blurring of predicted emitter locations in the C/C configuration (Fig. C.12(c)). However, in the C/CP configuration, we more clearly identify what we believe to be small clusters of emitters (Figure C.12(d)). Overall, the data suggests that the TFLN waveguide collection channels are less sensitive to background fluorescence as compared to the confocal collection channels. This difference might be useful in future studies for resolving emitters in 3D space. However, the waveguide collection channels may be more susceptible to collecting in-nanobeam scattering and coupling to un-targeted emitters. Furthermore, our collection here must be calibrated to the in/out-coupling of the gratings.

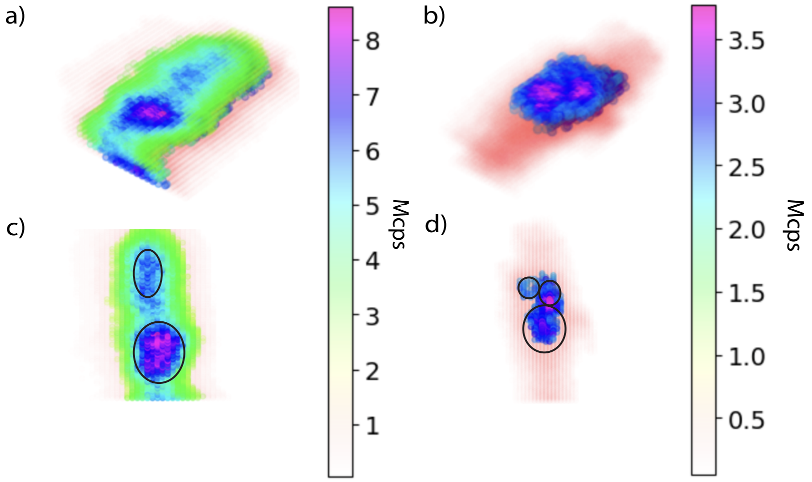

Figure C.12: Focus-dependent 3D PL Maps.

Opaque blue coloring corresponds to high counts, while transparent red corresponds to low counts. **(a)** PL map obtained in the C/C configuration. Steps in the focal plane are reflected in the plot by different z-axis locations. PL maps in 2D are stacked along the z-axis to produce a 3D image. We threshold the data to make lower count areas more transparent for visualization purposes. **(b)** PL map obtained in the C/CP configuration. Configuration of data and thresholding are identical to that used to produce the map in (a). **(c)** Top-down view of two focal plane steps from (a). We circle the suspected clusters of emitters for visualization purposes. **(d)** Top-down view of two focal plane steps from (b) (same focal steps as in (c)). We circle the suspected clusters of emitters for visualization purposes.

Grating	Average Pitch (nm)	Minimum Duty Cycle	Maximum Duty Cycle
Device	429 ± 11	0.313	0.809
Control 1	425 ± 3	0.331	0.814
Control A	425 ± 5	0.338	0.816

Table C.1: Table of fabricated grating parameters, derived from ProSEM analyses.

C.10 SEM Imaging of Device

To illustrate the structure of the device more clearly, we have included several SEM images in this section. To reduce sample charging, 2-3 nm of Au is sputtered on the sample surface prior to imaging.

First, we present SEMs of the integrated device and two control devices in Fig. C.13. Details of the integrated device, including the adiabatic taper points and the extra structure observed in the central nanobeam broadening are shown in Fig. C.14. Analysis of the lithium niobate gratings for each is performed using GenISys's ProSEM software. The results of the analysis are summarized in Table C.1 and a visual comparison is presented in Fig. C.15. The observed parameters for the grating couplers match well with the intended design, which is a duty cycle sweep from 80% to 30% with a grating pitch of 425 nm. Overall, the SEM imaging supports the assumption that the TFLN grating couplers share similar coupling to free space, so that the differences observed between the control devices and the integrated device can be largely attributed to the taper efficiency of the diamond to TFLN, with some difference in alignment accounting for additional variation.

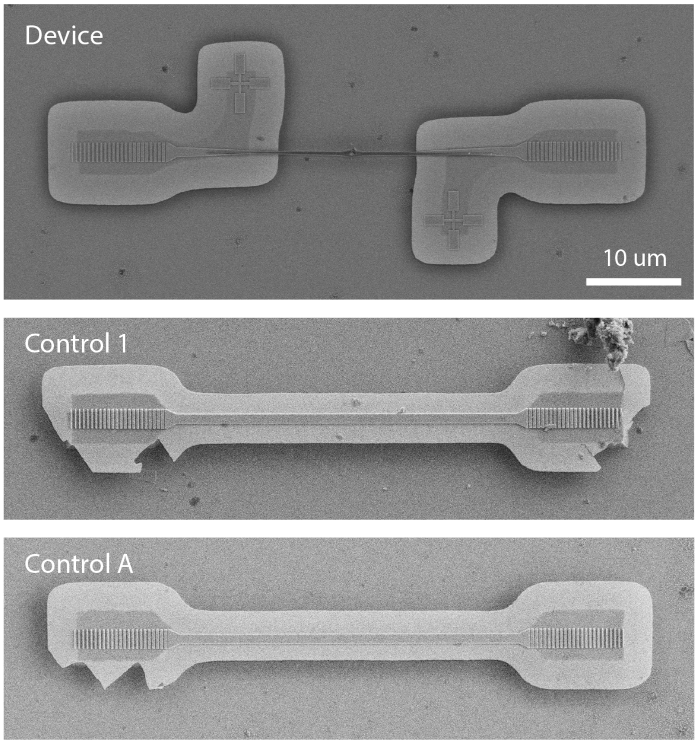

Figure C.13: SEMs of integrated (”Device 1“) and control devices (”Control 1“ and ”Control A“).

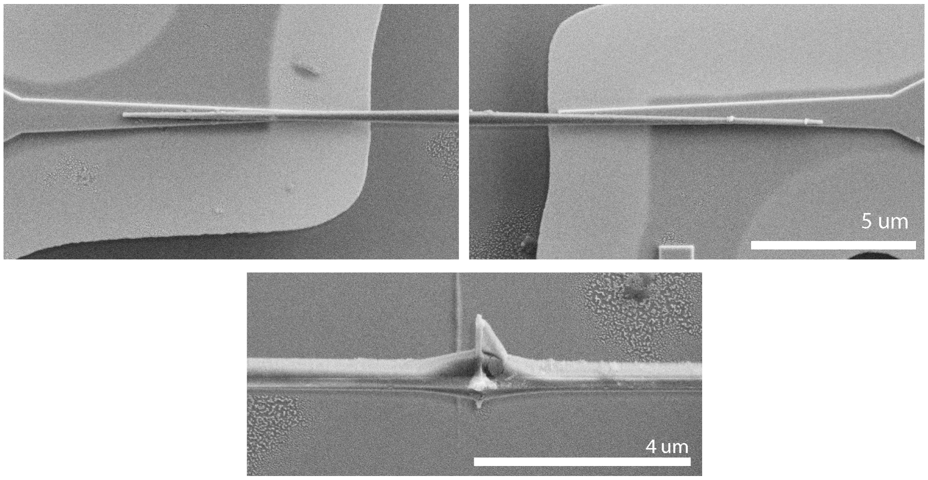

Figure C.14: SEMs of integrated device details.

The top panels display both adiabatic taper contacts for the integrated device. The bottom panel presents the fabrication structure that is found in the central broadened region of the diamond nanobeam.

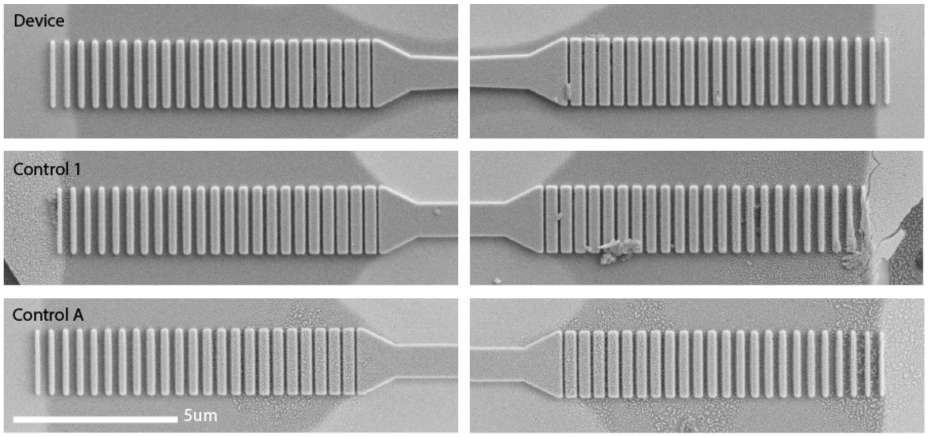

Figure C.15: SEMs of TFLN grating couplers.

Both left and right side grating couplers for the integrated device socket and both control devices are shown here. By visual inspection, we conclude that the grating coupler dimensions, and therefore performance, is comparable for all devices. ProSEM quantitative analyses provides additional evidence for this assumption.

Bibliography

[1] H. Kragh. *Quantum Generations: A History of Physics in the Twentieth Century*. Book collections on Project MUSE. Princeton University Press, 2002.

[2] Richard P Feynman. Simulating physics with computers. In *Feynman and computation*, pages 133–153. cRc Press, 2018.

[3] P.W. Shor. Algorithms for quantum computation: discrete logarithms and factoring. In *Proceedings 35th Annual Symposium on Foundations of Computer Science*, pages 124–134, 1994.

[4] Maximilian Ruf, Noel H. Wan, Hyeongrak Choi, Dirk Englund, and Ronald Hanson. Quantum networks based on color centers in diamond. *Journal of Applied Physics*, 130(7):070901, 08 2021.

[5] Prasoon K. Shandilya, Sigurd Flågan, Natalia C. Carvalho, Elham Zohari, Vinaya K. Kavatamane, Joseph E. Losby, and Paul E. Barclay. Diamond integrated quantum nanophotonics: Spins, photons and phonons. *Journal of Lightwave Technology*, 40(23):7538–7571, 2022.

[6] C. L. Degen, F. Reinhard, and P. Cappellaro. Quantum sensing. *Rev. Mod. Phys.*, 89:035002, Jul 2017.

[7] David P DiVincenzo. Topics in quantum computers. In *Mesoscopic electron transport*, pages 657–677. Springer, 1997.

[8] Alexandre Blais, Arne L. Grimsmo, S. M. Girvin, and Andreas Wallraff. Circuit quantum electrodynamics. *Rev. Mod. Phys.*, 93:025005, May 2021.

[9] P. Krantz, M. Kjaergaard, F. Yan, T. P. Orlando, S. Gustavsson, and W. D. Oliver. A quantum engineer's guide to superconducting qubits. *Applied Physics Reviews*, 6(2):021318, 06 2019.

[10] Guido Burkard, Thaddeus D. Ladd, Andrew Pan, John M. Nichol, and Jason R. Petta. Semiconductor spin qubits. *Rev. Mod. Phys.*, 95:025003, Jun 2023.

[11] Nathalie P. de Leon, Kohei M. Itoh, Dohun Kim, Karan K. Mehta, Tracy E. Northup, Hanhee Paik, B. S. Palmer, N. Samarth, Sorawis Sangtawesin, and D. W. Steuerman. Materials challenges and opportunities for quantum computing hardware. *Science*, 372(6539):eabb2823, 2021.

[12] D. Leibfried, R. Blatt, C. Monroe, and D. Wineland. Quantum dynamics of single trapped ions. *Rev. Mod. Phys.*, 75:281–324, Mar 2003.

[13] F Pelayo García de Arquer, Dmitri V Talapin, Victor I Klimov, Yasuhiko Arakawa, Manfred Bayer, and Edward H Sargent. Semiconductor quantum dots: Technological progress and future challenges. *Science*, 373(6555):eaaz8541, 2021.

[14] Gary Wolfowicz, F Joseph Heremans, Christopher P Anderson, Shun Kanai, Hosung Seo, Adam Gali, Giulia Galli, and David D Awschalom. Quantum guidelines for solid-state spin defects. *Nature Reviews Materials*, 6(10):906–925, 2021.

[15] A. Gruber, A. Dräbenstedt, C. Tietz, L. Fleury, J. Wrachtrup, and C. von Borczyskowski. Scanning confocal optical microscopy and magnetic resonance on single defect centers. *Science*, 276(5321):2012–2014, 1997.

[16] Tim Schröder, Sara L. Mouradian, Jiabao Zheng, Matthew E. Trusheim, Michael Walsh, Edward H. Chen, Luozhou Li, Igal Bayn, and Dirk Englund. Quantum nanophotonics in diamond. *J. Opt. Soc. Am. B*, 33(4):B65–B83, Apr 2016.

[17] Tetsuya Tohei, Akihide Kuwabara, Fumiyasu Oba, and Isao Tanaka. Debye temperature and stiffness of carbon and boron nitride polymorphs from first principles calculations. *Phys. Rev. B*, 73:064304, Feb 2006.

[18] C. E. Bradley, S. W. de Bone, P. F. W. Möller, S. Baier, M. J. Degen, S. J. H. Loenen, H. P. Bartling, M. Markham, D. J. Twitchen, R. Hanson, D. Elkouss, and T. H. Taminiau. Robust quantum-network memory based on spin qubits in isotopically engineered diamond. *npj Quantum Information*, 8(1):122, Oct 2018.

[19] J Walker. Optical absorption and luminescence in diamond. *Reports on Progress in Physics*, 42(10):1605, oct 1979.

[20] G. Davies and M. F. Hamer. Optical studies of the 1.945 ev vibronic band in diamond. *Proceedings of the Royal Society of London. A. Mathematical and Physical Sciences*, 348(1653):285–298, 1976.

[21] Hannes Bernien, Bas Hensen, Wolfgang Pfaff, Gerwin Koolstra, Machiel S Blok, Lucio Robledo, Tim H Taminiau, Matthew Markham, Daniel J Twitchen, Lilian Childress, et al. Heralded

entanglement between solid-state qubits separated by three metres. *Nature*, 497(7447):86–90, 2013.

[22] B. Hensen, H. Bernien, A. E. Dréau, A. Reiserer, N. Kalb, M. S. Blok, J. Ruitenberg, R. F. L. Vermeulen, R. N. Schouten, C. Abellán, W. Amaya, V. Pruneri, M. W. Mitchell, M. Markham, D. J. Twitchen, D. Elkouss, S. Wehner, T. H. Taminiau, and R. Hanson. Loophole-free bell inequality violation using electron spins separated by 1.3 kilometres. *Nature*, 526(7575):682–686, Oct 2015.

[23] Peter C. Humphreys, Norbert Kalb, Jaco P. J. Morits, Raymond N. Schouten, Raymond F. L. Vermeulen, Daniel J. Twitchen, Matthew Markham, and Ronald Hanson. Deterministic delivery of remote entanglement on a quantum network. *Nature*, 558(7709):268–273, 2018.

[24] Matteo Pompili, Sophie LN Hermans, Simon Baier, Hans KC Beukers, Peter C Humphreys, Raymond N Schouten, Raymond FL Vermeulen, Marijn J Tiggelman, Laura dos Santos Martins, Bas Dirkse, et al. Realization of a multinode quantum network of remote solid-state qubits. *Science*, 372(6539):259–264, 2021.

[25] S. L. N. Hermans, M. Pompili, H. K. C. Beukers, S. Baier, J. Borregaard, and R. Hanson. Qubit teleportation between non-neighbouring nodes in a quantum network. *Nature*, 605(7911):663–668, may 2022.

[26] Sungkun Hong, Michael S Grinolds, Linh M Pham, David Le Sage, Lan Luan, Ronald L Walsworth, and Amir Yacoby. Nanoscale magnetometry with nv centers in diamond. *MRS bulletin*, 38(2):155–161, 2013.

[27] Jared Rovny, Sarang Gopalakrishnan, Ania C Bleszynski Jayich, Patrick Maletinsky, Eugene Demler, and Nathalie P de Leon. Nanoscale diamond quantum sensors for many-body physics. *Nature Reviews Physics*, pages 1–16, 2024.

[28] Matthew E. Trusheim, Benjamin Pingault, Noel H. Wan, Mustafa Gündoğan, Lorenzo De Santis, Romain Debroux, Dorian Gangloff, Carola Purser, Kevin C. Chen, Michael Walsh, Joshua J. Rose, Jonas N. Becker, Benjamin Lienhard, Eric Bersin, Ioannis Paradeisanos, Gang Wang, Dominika Lyzwa, Alejandro R-P. Montblanch, Girish Malladi, Hassaram Bakhru, Andrea C. Ferrari, Ian A. Walmsley, Mete Atatüre, and Dirk Englund. Transform-limited photons from a coherent tin-vacancy spin in diamond. *Phys. Rev. Lett.*, 124:023602, Jan 2020.

[29] Johannes Görlitz, Dennis Herrmann, Gergő Thiering, Philipp Fuchs, Morgane Gandil, Takayuki Iwasaki, Takashi Taniguchi, Michael Kieschnick, Jan Meijer, Mutsuko Hatano, Adam Gali, and Christoph Becher. Spectroscopic investigations of negatively charged tin-vacancy centres in diamond. *New Journal of Physics*, 22(1):013048, jan 2020.

[30] Julia M. Brevoord, Lorenzo De Santis, Takashi Yamamoto, Matteo Pasini, Nina Codreanu, Tim Turan, Hans K.C. Beukers, Christopher Waas, and Ronald Hanson. Heralded initialization of charge state and optical-transition frequency of diamond tin-vacancy centers. *Physical Review Applied*, 21, 5 2024.

[31] Keita Ikeda, Yiyang Chen, Peng Wang, Yoshiyuki Miyamoto, Takashi Taniguchi, Shinobu Onoda, Mutsuko Hatano, and Takayuki Iwasaki. Charge state transition of spectrally stabilized tin-vacancy centers in diamond. *ACS Photonics*, 12:2972–2981, 6 2025.

[32] Disheng Chen, Zhao Mu, Yu Zhou, Johannes E. Fröch, Abdullah Rasmit, Carole Diederichs, Nikolay Zheludev, Igor Aharonovich, and Wei-bo Gao. Optical gating of resonance fluorescence from a single germanium vacancy color center in diamond. *Phys. Rev. Lett.*, 123:033602, Jul 2019.

[33] Disheng Chen, Johannes E. Fröch, Shihao Ru, Hongbing Cai, Naizhou Wang, Giorgio Adamo, John Scott, Fuli Li, Nikolay Zheludev, Igor Aharonovich, and Weibo Gao. Quantum interference of resonance fluorescence from germanium-vacancy color centers in diamond. *Nano Letters*, 22(15):6306–6312, 2022.

[34] Jesús Arjona Martínez, Ryan A. Parker, Kevin C. Chen, Carola M. Purser, Linsen Li, Cathryn P. Michaels, Alexander M. Stramma, Romain Debroux, Isaac B. Harris, Martin Hayhurst Appel, Eleanor C. Nichols, Matthew E. Trusheim, Dorian A. Gangloff, Dirk Englund, and Mete Atatüre. Photonic indistinguishability of the tin-vacancy center in nanostructured diamond. *Phys. Rev. Lett.*, 129:173603, Oct 2022.

[35] Ilya P. Radko, Mads Boll, Niels M. Israelsen, Nicole Raatz, Jan Meijer, Fedor Jelezko, Ulrik L. Andersen, and Alexander Huck. Determining the internal quantum efficiency of shallow-implanted nitrogen-vacancy defects in bulk diamond. *Opt. Express*, 24(24):27715–27725, Nov 2016.

[36] Paul E. Barclay, Kai-Mei C. Fu, Charles Santori, Andrei Faraon, and Raymond G. Beausoleil. Hybrid nanocavity resonant enhancement of color center emission in diamond. *Phys. Rev. X*, 1:011007, Sep 2011.

[37] Daniel Riedel, Immo Söllner, Brendan J. Shields, Sebastian Starosielec, Patrick Appel, Elke Neu, Patrick Maletinsky, and Richard J. Warburton. Deterministic enhancement of coherent photon generation from a nitrogen-vacancy center in ultrapure diamond. *Physical Review X*, 7(3):031040, sep 2017.

[38] Philipp Fuchs, Thomas Jung, Michael Kieschnick, Jan Meijer, and Christoph Becher. A cavity-based optical antenna for color centers in diamond. *APL Photonics*, 6(8):086102, 08 2021.

[39] Ruffin E. Evans, Alp Sipahigil, Denis D. Sukachev, Alexander S. Zibrov, and Mikhail D. Lukin. Narrow-linewidth homogeneous optical emitters in diamond nanostructures via silicon ion implantation. *Physical Review Applied*, 5(4):044010, apr 2016.

[40] C. T. Nguyen, D. D. Sukachev, M. K. Bhaskar, B. Machielse, D. S. Levonian, E. N. Knall, P. Stroganov, C. Chia, M. J. Burek, R. Riedinger, H. Park, M. Lončar, and M. D. Lukin. An integrated nanophotonic quantum register based on silicon-vacancy spins in diamond. *Physical Review B*, 100(16):165428, oct 2019.

[41] C. T. Nguyen, D. D. Sukachev, M. K. Bhaskar, B. Machielse, D. S. Levonian, E. N. Knall, P. Stroganov, R. Riedinger, H. Park, M. Lončar, and M. D. Lukin. Quantum network nodes based on diamond qubits with an efficient nanophotonic interface. *Physical Review Letters*, 123(18):183602, oct 2019.

[42] M. K. Bhaskar, R. Riedinger, B. Machielse, D. S. Levonian, C. T. Nguyen, E. N. Knall, H. Park, D. Englund, M. Lončar, D. D. Sukachev, and M. D. Lukin. Experimental demonstration of memory-enhanced quantum communication. *Nature*, 580(7801):60–64, apr 2020.

[43] Can M Knaut, Aziza Suleymanzade, Y-C Wei, Daniel R Assumpcao, P-J Stas, Yan Qi Huan, Bartholomeus Machielse, Erik N Knall, Madison Sutula, Gefen Baranes, et al. Entanglement of nanophotonic quantum memory nodes in a telecom network. *Nature*, 629(8012):573–578, 2024.

[44] Takayuki Iwasaki, Yoshiyuki Miyamoto, Takashi Taniguchi, Petr Siyushev, Mathias H. Metsch, Fedor Jelezko, and Mutsuko Hatano. Tin-vacancy quantum emitters in diamond. *Phys. Rev. Lett.*, 119:253601, Dec 2017.

[45] Christian Hepp, Tina Müller, Victor Waselowski, Jonas N. Becker, Benjamin Pingault, Hadwig Sternschulte, Doris Steinmüller-Nethl, Adam Gali, Jeronimo R. Maze, Mete Atatüre, and Christoph Becher. Electronic structure of the silicon vacancy color center in diamond. *Phys. Rev. Lett.*, 112:036405, Jan 2014.

[46] Alison E. Rugar, Constantin Dory, Shuo Sun, and Jelena Vučković. Characterization of optical and spin properties of single tin-vacancy centers in diamond nanopillars. *Phys. Rev. B*, 99:205417, May 2019.

[47] Lachlan J. Rogers, Kay D. Jahnke, Mathias H. Metsch, Alp Sipahigil, Jan M. Binder, Tokuyuki Teraji, Hitoshi Sumiya, Junichi Isoya, Mikhail D. Lukin, Philip Hemmer, and Fedor Jelezko. All-optical initialization, readout, and coherent preparation of single silicon-vacancy spins in diamond. *Phys. Rev. Lett.*, 113:263602, Dec 2014.

[48] Gergő Thiering and Adam Gali. Ab initio magneto-optical spectrum of group-iv vacancy color centers in diamond. *Physical Review X*, 8(2):021063, 2018.

[49] Romain Debroux, Cathryn P. Michaels, Carola M. Purser, Noel Wan, Matthew E. Trusheim, Jesús Arjona Martínez, Ryan A. Parker, Alexander M. Stramma, Kevin C. Chen, Lorenzo de Santis, Evgeny M. Alexeev, Andrea C. Ferrari, Dirk Englund, Dorian A. Gangloff, and Mete Atatüre. Quantum control of the tin-vacancy spin qubit in diamond. *Phys. Rev. X*, 11:041041, Nov 2021.

[50] Eric I Rosenthal, Christopher P Anderson, Hannah C Kleidermacher, Abigail J Stein, Hope Lee, Jakob Grzesik, Giovanni Scuri, Alison E Rugar, Daniel Riedel, Shahriar Aghaeimeibodi, et al. Microwave spin control of a tin-vacancy qubit in diamond. *Physical Review X*, 13(3):031022, 2023.

[51] Xinghan Guo, Alexander M. Stramma, Zixi Li, William G. Roth, Benchen Huang, Yu Jin, Ryan A. Parker, Jesús Arjona Martínez, Noah Shofer, Cathryn P. Michaels, Carola P. Purser, Martin H. Appel, Evgeny M. Alexeev, Tianle Liu, Andrea C. Ferrari, David D. Awschalom, Nazar Delegan, Benjamin Pingault, Giulia Galli, F. Joseph Heremans, Mete Atatüre, and Alexander A. High. Microwave-based quantum control and coherence protection of tin-vacancy spin qubits in a strain-tuned diamond-membrane heterostructure. *Phys. Rev. X*, 13:041037, Nov 2023.

[52] Eric I Rosenthal, Souvik Biswas, Giovanni Scuri, Hope Lee, Abigail J Stein, Hannah C Kleidermacher, Jakob Grzesik, Alison E Rugar, Shahriar Aghaeimeibodi, Daniel Riedel, et al. Single-shot readout and weak measurement of a tin-vacancy qubit in diamond. *Physical Review X*, 14(4):041008, 2024.

[53] Ioannis Karapatzakis, Jeremias Resch, Marcel Schrodin, Philipp Fuchs, Michael Kieschnick, Julia Heupel, Luis Kussi, Christoph Sürgers, Cyril Popov, Jan Meijer, Christoph Becher, Wolfgang Wernsdorfer, and David Hunger. Microwave control of the tin-vacancy spin qubit in diamond with a superconducting waveguide. *arXiv preprint arXiv:2403.00521*, 2024.

[54] Hans K. C. Beukers, Christopher Waas, Matteo Pasini, Hendrik B. van Ommen, Zarije Ademi, Mariagrazia Iuliano, Nina Codreanu, Julia M. Brevoord, Tim Turan, Tim H. Taminiau, and Ronald Hanson. Control of solid-state nuclear spin qubits using an electron spin-1/2. *Phys. Rev. X*, 15:021011, Apr 2025.

[55] Kay D Jahnke, Alp Sipahigil, Jan M Binder, Marcus W Doherty, Mathias Metsch, Lachlan J Rogers, Neil B Manson, Mikhail D Lukin, and Fedor Jelezko. Electron–phonon processes of the silicon-vacancy centre in diamond. *New Journal of Physics*, 17(4):043011, apr 2015.

[56] Alison E. Rugar. *Quantum Photonics with the Tin-Vacancy Center in Diamond.* Phd thesis, Stanford University, Stanford, CA, June 2022. Available at `https://web.stanford.edu/group/nqp/jv_files/thesis/rugar_thesis.pdf`.

[57] Mohammad Jamali, Ilja Gerhardt, Mohammad Rezai, Karsten Frenner, Helmut Fedder, and Jörg Wrachtrup. Microscopic diamond solid-immersion-lenses fabricated around single defect centers by focused ion beam milling. *Review of Scientific Instruments*, 85(12):123703, 12 2014.

[58] Marina Radulaski, Matthias Widmann, Matthias Niethammer, Jingyuan Linda Zhang, Sang-Yun Lee, Torsten Rendler, Konstantinos G. Lagoudakis, Nguyen Tien Son, Erik Janzén, Takeshi Ohshima, Jörg Wrachtrup, and Jelena Vučković. Scalable quantum photonics with single color centers in silicon carbide. *Nano Letters*, 17(3):1782–1786, 2017.

[59] Alison E. Rugar, Constantin Dory, Shahriar Aghaeimeibodi, Haiyu Lu, Shuo Sun, Sattwik Deb Mishra, Zhi-Xun Shen, Nicholas A. Melosh, and Jelena Vučković. Narrow-linewidth tin-vacancy centers in a diamond waveguide. *ACS Photonics*, 7(9):2356–2361, 2020.

[60] Daniel Riedel, Hope Lee, Jason F. Herrmann, Jakob Grzesik, Vahid Ansari, Jean-Michel Borit, Hubert S. Stokowski, Shahriar Aghaeimeibodi, Haiyu Lu, Patrick J. McQuade, Nicholas A. Melosh, Zhi-Xun Shen, Amir H. Safavi-Naeini, and Jelena Vučković. Efficient photonic integration of diamond color centers and thin-film lithium niobate. *ACS Photonics*, 10(12):4236–4243, 2023.

[61] Matteo Pasini, Nina Codreanu, Tim Turan, Adrià Riera Moral, Christian F. Primavera, Lorenzo De Santis, Hans K. C. Beukers, Julia M. Brevoord, Christopher Waas, Johannes Borregaard, and Ronald Hanson. Nonlinear quantum photonics with a tin-vacancy center coupled to a one-dimensional diamond waveguide. *Phys. Rev. Lett.*, 133:023603, Jul 2024.

[62] Yufan Li, Fabian A. Gerritsma, Samer Kurdi, Nina Codreanu, Simon Gröblacher, Ronald Hanson, Richard Norte, and Toeno van der Sar. A fiber-coupled scanning magnetometer with nitrogen-vacancy spins in a diamond nanobeam. *ACS Photonics*, 10(6):1859–1865, 2023.

[63] Jelena Vuckovic. Quantum optics and cavity qed with quantum dots in photonic crystals, 2014.

[64] Serge Haroche and Jean-Michel Raimond. *Exploring the Quantum: Atoms, Cavities, and Photons.* Oxford University Press, 08 2006.

[65] Yanik Herrmann, Julius Fischer, Julia M. Brevoord, Colin Sauerzapf, Leonardo G. C. Wienhoven, Laurens J. Feije, Matteo Pasini, Martin Eschen, Maximilian Ruf, Matthew J. Weaver, and Ronald Hanson. Coherent coupling of a diamond tin-vacancy center to a tunable open microcavity. *Phys. Rev. X*, 14:041013, Oct 2024.

[66] Yanik Herrmann, Julius Fischer, Stijn Scheijen, Cornelis F. J. Wolfs, Julia M. Brevoord, Colin Sauerzapf, Leonardo G. C. Wienhoven, Laurens J. Feije, Martin Eschen, Maximilian Ruf, Matthew J. Weaver, and Ronald Hanson. A low-temperature tunable microcavity featuring high passive stability and microwave integration. *AVS Quantum Science*, 6(4):041401, 12 2024.

[67] Andrei Faraon, Paul E Barclay, Charles Santori, Kai-Mei C Fu, and Raymond G Beausoleil. Resonant enhancement of the zero-phonon emission from a colour centre in a diamond cavity. *Nature Photonics*, 5(5):301–305, 2011.

[68] Birgit J. M. Hausmann, Brendan Shields, Qimin Quan, Patrick Maletinsky, Murray McCutcheon, Jennifer T. Choy, Tom M. Babinec, Alexander Kubanek, Amir Yacoby, Mikhail D. Lukin, and Marko Loncar. Integrated diamond networks for quantum nanophotonics. *Nano Letters*, 12(3):1578–1582, 2012.

[69] B. J. M. Hausmann, I. Bulu, V. Venkataraman, P. Deotare, and M. Lončar. Diamond nonlinear photonics. *Nature Photonics*, 8(5):369–374, May 2014.

[70] Behzad Khanaliloo, Matthew Mitchell, Aaron C. Hryciw, and Paul E. Barclay. High-q/v monolithic diamond microdisks fabricated with quasi-isotropic etching. *Nano Letters*, 15(8):5131–5136, 2015.

[71] Tamiko Masuda, J. P. E. Hadden, David P. Lake, Matthew Mitchell, Sigurd Flågan, and Paul E. Barclay. Fiber-taper collected emission from nv centers in high-q/v diamond microdisks. *Opt. Express*, 32(5):8172–8188, Feb 2024.

[72] Xinghan Guo, Mouzhe Xie, Anchita Addhya, Avery Linder, Uri Zvi, Stella Wang, Xiaofei Yu, Tanvi D. Deshmukh, Yuzi Liu, Ian N. Hammock, Zixi Li, Clayton T. DeVault, Amy Butcher, Aaron P. Esser-Kahn, David D. Awschalom, Nazar Delegan, Peter C. Maurer, F. Joseph Heremans, and Alexander A. High. Direct-bonded diamond membranes for heterogeneous quantum and electronic technologies. *Nature Communications*, 15(1):8788, Oct 2024.

[73] John D. Joannopoulos, Steven G. Johnson, Joshua N. Winn, and Robert D. Meade. *Photonic Crystals: Molding the Flow of Light (Second Edition)*. Princeton University Press, 2 edition, 2008.

[74] Daniil M. Lukin, Bennet Windt, Miguel Bello, Dominic Catanzaro, Melissa A. Guidry, Eran Lustig, Souvik Biswas, Giovanni Scuri, Trung Kien Le, Joshua Yang, Arina A. Nikitina, Misagh Ghezellou, Hiroshi Abe, Takeshi Ohshima, Jawad Ul-Hassan, and Jelena Vučković. Mesoscopic cavity quantum electrodynamics with phase-disordered emitters in a kerr nonlinear resonator. *arXiv preprint arXiv:2504.09324*, 2025.

[75] Alison E. Rugar, Shahriar Aghaeimeibodi, Daniel Riedel, Constantin Dory, Haiyu Lu, Patrick J. McQuade, Zhi Xun Shen, Nicholas A. Melosh, and Jelena Vučković. Quantum photonic interface for tin-vacancy centers in diamond. *Physical Review X*, 11, 9 2021.

[76] Janine Riedrich-Möller, Laura Kipfstuhl, Christian Hepp, Elke Neu, Christoph Pauly, Frank Mücklich, Armin Baur, Michael Wandt, Sandra Wolff, Martin Fischer, et al. One-and two-dimensional photonic crystal microcavities in single crystal diamond. *Nature nanotechnology*, 7(1):69, 2012.

[77] Parag B. Deotare, Murray W. McCutcheon, Ian W. Frank, Mughees Khan, and Marko Lončar. High quality factor photonic crystal nanobeam cavities. *Applied Physics Letters*, 94(12):121106, 03 2009.

[78] A. Sipahigil, R. E. Evans, D. D. Sukachev, M. J. Burek, J. Borregaard, M. K. Bhaskar, C. T. Nguyen, J. L. Pacheco, H. A. Atikian, C. Meuwly, R. M. Camacho, F. Jelezko, E. Bielejec, H. Park, M. Lončar, and M. D. Lukin. An integrated diamond nanophotonics platform for quantum-optical networks. *Science*, 354(6314):847–850, 2016.

[79] Kazuhiro Kuruma, Benjamin Pingault, Cleaven Chia, Dylan Renaud, Patrick Hoffmann, Satoshi Iwamoto, Carsten Ronning, and Marko Lončar. Coupling of a single tin-vacancy center to a photonic crystal cavity in diamond. *Applied Physics Letters*, 118(23):230601, 06 2021.

[80] Sophie W. Ding, Michael Haas, Xinghan Guo, Kazuhiro Kuruma, Chang Jin, Zixi Li, David D. Awschalom, Nazar Delegan, F. Joseph Heremans, Alexander A. High, and Marko Loncar. High-q cavity interface for color centers in thin film diamond. *Nature Communications*, 15, 12 2024.

[81] Amnon Yariv and Pochi Albert Yeh. *Optical Waves in Crystals: Propagation and Control of Laser Radiation.* Wiley, 1983.

[82] Michael J. Burek, Nathalie P. de Leon, Brendan J. Shields, Birgit J. M. Hausmann, Yiwen Chu, Qimin Quan, Alexander S. Zibrov, Hongkun Park, Mikhail D. Lukin, and Marko Lončar. Free-standing mechanical and photonic nanostructures in single-crystal diamond. *Nano Letters*, 12(12):6084–6089, 2012.

[83] Behzad Khanaliloo, Matthew Mitchell, Aaron C. Hryciw, and Paul E. Barclay. High-q/v monolithic diamond microdisks fabricated with quasi-isotropic etching. *Nano Letters*, 15(8):5131–5136, 2015.

[84] Constantin Dory, Dries Vercruysse, Ki Youl Yang, Neil V Sapra, Alison E Rugar, Shuo Sun, Daniil M Lukin, Alexander Y Piggott, Jingyuan L Zhang, Marina Radulaski, et al. Inverse-designed diamond photonics. *Nature communications*, 10(1):3309, 2019.

[85] B. Machielse, S. Bogdanovic, S. Meesala, S. Gauthier, M. J. Burek, G. Joe, M. Chalupnik, Y. I. Sohn, J. Holzgrafe, R. E. Evans, C. Chia, H. Atikian, M. K. Bhaskar, D. D. Sukachev,

L. Shao, S. Maity, M. D. Lukin, and M. Lončar. Quantum interference of electromechanically stabilized emitters in nanophotonic devices. *Phys. Rev. X*, 9:031022, Aug 2019.

[86] Srujan Meesala, Young-Ik Sohn, Benjamin Pingault, Linbo Shao, Haig A. Atikian, Jeffrey Holzgrafe, Mustafa Gündoğan, Camille Stavrakas, Alp Sipahigil, Cleaven Chia, Ruffin Evans, Michael J. Burek, Mian Zhang, Lue Wu, Jose L. Pacheco, John Abraham, Edward Bielejec, Mikhail D. Lukin, Mete Atatüre, and Marko Lončar. Strain engineering of the silicon-vacancy center in diamond. *Phys. Rev. B*, 97:205444, May 2018.

[87] Xinghan Guo, Nazar Delegan, Jonathan C. Karsch, Zixi Li, Tianle Liu, Robert Shreiner, Amy Butcher, David D. Awschalom, F. Joseph Heremans, and Alexander A. High. Tunable and transferable diamond membranes for integrated quantum technologies. *Nano Letters*, 21(24):10392–10399, 2021.

[88] Hyunseok Oh, Viraj Dharod, Carl Padgett, Lillian B Hughes, Jayameenakshi Venkatraman, Shreyas Parthasarathy, Ekaterina Osipova, Ian Hedgepeth, Jeffrey V Cady, Luca Basso, et al. A spin-embedded diamond optomechanical resonator with mechanical quality factor exceeding one million. *arXiv preprint arXiv:2508.05906*, 2025.

[89] Kelley Rivoire, Andrei Faraon, and Jelena Vuckovic. Gallium phosphide photonic crystal nanocavities in the visible. *Applied Physics Letters*, 93(6):063103, 08 2008.

[90] Yiyang Gong and Jelena Vučković. Photonic crystal cavities in silicon dioxide. *Applied Physics Letters*, 96(3):031107, 01 2010.

[91] Jingyuan Linda Zhang, Shuo Sun, Michael J. Burek, Constantin Dory, Yan-Kai Tzeng, Kevin A. Fischer, Yousif Kelaita, Konstantinos G. Lagoudakis, Marina Radulaski, Zhi-Xun Shen, Nicholas A. Melosh, Steven Chu, Marko Lončar, and Jelena Vučković. Strongly cavity-enhanced spontaneous emission from silicon-vacancy centers in diamond. *Nano Letters*, 18(2):1360–1365, 2018.

[92] R. E. Evans, M. K. Bhaskar, D. D. Sukachev, C. T. Nguyen, A. Sipahigil, M. J. Burek, B. Machielse, G. H. Zhang, A. S. Zibrov, E. Bielejec, H. Park, M. Lončar, and M. D. Lukin. Photon-mediated interactions between quantum emitters in a diamond nanocavity. *Science*, 362(6415):662–665, 2018.

[93] Michael J. Burek, Charles Meuwly, Ruffin E. Evans, Mihir K. Bhaskar, Alp Sipahigil, Srujan Meesala, Bartholomeus Machielse, Denis D. Sukachev, Christian T. Nguyen, Jose L. Pacheco, Edward Bielejec, Mikhail D. Lukin, and Marko Lončar. Fiber-coupled diamond quantum nanophotonic interface. *Phys. Rev. Appl.*, 8:024026, Aug 2017.

[94] Ryan A. Parker, Jesús Arjona Martínez, Kevin C. Chen, Alexander M. Stramma, Isaac B. Harris, Cathryn P. Michaels, Matthew E. Trusheim, Hayhurst Appel, Purser Martin, Roth Carola M., William G., Dirk Englund, and Mete Atatüre. A diamond nanophotonic interface with an optically accessible deterministic electronuclear spin register. *Nature Photonics*, 18:156–161, Feb 2024.

[95] A. Sipahigil, K. D. Jahnke, L. J. Rogers, T. Teraji, J. Isoya, A. S. Zibrov, F. Jelezko, and M. D. Lukin. Indistinguishable photons from separated silicon-vacancy centers in diamond. *Phys. Rev. Lett.*, 113:113602, Sep 2014.

[96] Yasuyuki Narita, Peng Wang, Keita Ikeda, Kazuki Oba, Yoshiyuki Miyamoto, Takashi Taniguchi, Shinobu Onoda, Mutsuko Hatano, and Takayuki Iwasaki. Multiple tin-vacancy centers in diamond with nearly identical photon frequency and linewidth. *Phys. Rev. Appl.*, 19:024061, Feb 2023.

[97] Shahriar Aghaeimeibodi, Daniel Riedel, Alison E. Rugar, Constantin Dory, and Jelena Vučković. Electrical tuning of tin-vacancy centers in diamond. *Physical Review Applied*, 15(6):064010, jun 2021.

[98] Julia M. Brevoord, Leonardo G. C. Wienhoven, Nina Codreanu, Tetsuro Ishiguro, Elvis van Leeuwen, Mariagrazia Iuliano, Lorenzo De Santis, Christopher Waas, Hans K. C. Beukers, Tim Turan, Carlos Errando-Herranz, Kenichi Kawaguchi, and Ronald Hanson. Large-range tuning and stabilization of the optical transition of diamond tin-vacancy centers by in situ strain control. *Applied Physics Letters*, 126(17):174001, 04 2025.

[99] Manuel Rieger, Nori N. Chavira Leal, Rubek Poudel, Tobias Waldmann, Lina M. Todenhagen, Stefan Kresta, Viviana Villafane, Martin S. Brandt, Kai Müller, and Jonathan J. Finley. Second-order stark shifts exceeding 10 ghz in electrically contacted siv$^-$ centers in diamond. *arXiv preprint arXiv:2510.25543*, 2025.

[100] Vladislav Bushmakin, Oliver von Berg, Colin Sauerzapf, Sreehari Jayaram, Andrej Denisenko, Cristina Tarín, Jens Anders, Vadim Vorobyov, Ilja Gerhardt, Di Liu, and Jörg Wrachtrup. Two-photon interference of photons from remote tin-vacancy centers in diamond. *arXiv preprint arXiv:2412.17539*, 2025.

[101] D. S. Levonian, R. Riedinger, B. Machielse, E. N. Knall, M. K. Bhaskar, C. M. Knaut, R. Bekenstein, H. Park, M. Lončar, and M. D. Lukin. Optical entanglement of distinguishable quantum emitters. *Phys. Rev. Lett.*, 128:213602, May 2022.

[102] Anaïs Dréau, Anna Tchebotareva, Aboubakr El Mahdaoui, Cristian Bonato, and Ronald Hanson. Quantum frequency conversion of single photons from a nitrogen-vacancy center in diamond to telecommunication wavelengths. *Phys. Rev. Appl.*, 9:064031, Jun 2018.

[103] Eric Bersin, Madison Sutula, Yan Qi Huan, Aziza Suleymanzade, Daniel R. Assumpcao, Yan-Cheng Wei, Pieter-Jan Stas, Can M. Knaut, Erik N. Knall, Carsten Langrock, Neil Sinclair, Ryan Murphy, Ralf Riedinger, Matthew Yeh, C.J. Xin, Saumil Bandyopadhyay, Denis D. Sukachev, Bartholomeus Machielse, David S. Levonian, Mihir K. Bhaskar, Scott Hamilton, Hongkun Park, Marko Lončar, Martin M. Fejer, P. Benjamin Dixon, Dirk R. Englund, and Mikhail D. Lukin. Telecom networking with a diamond quantum memory. *PRX Quantum*, 5:010303, Jan 2024.

[104] Marlon Schäfer, Benjamin Kambs, Dennis Herrmann, Tobias Bauer, and Christoph Becher. Two-stage, low noise quantum frequency conversion of single photons from silicon-vacancy centers in diamond to the telecom c-band. *Advanced Quantum Technologies*, 8(2):2300228, 2025.

[105] Julia M. Brevoord, Jan Fabian Geus, Tim Turan, Miguel Guerrero Romero, Daniel Bedialauneta Rodríguez, Nina Codreanu, Alexander M. Stramma, Ronald Hanson, Florian Elsen, and Bernd Jungbluth. Quantum frequency conversion of single photons from a tin-vacancy center in diamond, 2025.

[106] Robert W. Boyd. *Nonlinear Optics, Third Edition*. Academic Press, Inc., USA, 4th edition, 2008.

[107] Parisa Behjat, Peyman Parsa, Natalia C. Carvalho, Prasoon K. Shandilya, and Paul E. Barclay. Kerr–optomechanical spectroscopy of multimode diamond resonators. *ACS Photonics*, 10(11):4014–4021, 2023.

[108] Prasoon K. Shandilya, Vinaya K. Kavatamane, Sigurd Flågan, David P. Lake, Denis Sukachev, and Paul E. Barclay. Nonlinear optical pumping to a diamond nv center dark state. *arXiv preprint arXiv:2411.10638*, 2024.

[109] Joe Itoi, Elham Zohari, Nicholas J. Sorensen, Waleed El-Sayed, Joseph E. Losby, Gustavo O. Luiz, Sigurd Flågan, and Paul E. Barclay. Non-volatile photorefractive tuning and green light generation in a diamond cavity. *arXiv preprint arXiv:2507.19583*, 2025.

[110] Aizitiaili Abulikemu, Yuta Kainuma, Toshu An, and Muneaki Hase. Second-harmonic generation in bulk diamond based on inversion symmetry breaking by color centers. *ACS Photonics*, 8(4):988–993, 2021.

[111] Sigurd Flågan, Joe Itoi, Prasoon K. Shandilya, Vinaya K. Kavatamane, Matthew Mitchell, David P. Lake, and Paul E. Barclay. Optical switching of $\chi^{(2)}$ in diamond photonics, 2025.

[112] RS Weis and TK Gaylord. Lithium niobate: Summary of physical properties and crystal structure. *Applied Physics A*, 37(4):191–203, 1985.

[113] Di Zhu, Linbo Shao, Mengjie Yu, Rebecca Cheng, Boris Desiatov, C. J. Xin, Yaowen Hu, Jeffrey Holzgrafe, Soumya Ghosh, Amirhassan Shams-Ansari, Eric Puma, Neil Sinclair, Christian Reimer, Mian Zhang, and Marko Lončar. Integrated photonics on thin-film lithium niobate. *Advances in Optics and Photonics*, 13(2):242, jun 2021.

[114] Andreas Boes, Lin Chang, Carsten Langrock, Mengjie Yu, Mian Zhang, Qiang Lin, Marko Lončar, Martin Fejer, John Bowers, and Arnan Mitchell. Lithium niobate photonics: Unlocking the electromagnetic spectrum. *Science*, 379(6627):eabj4396, 2023.

[115] Sara L. Mouradian, Tim Schröder, Carl B. Poitras, Luozhou Li, Jordan Goldstein, Edward H. Chen, Michael Walsh, Jaime Cardenas, Matthew L. Markham, Daniel J. Twitchen, Michal Lipson, and Dirk Englund. Scalable integration of long-lived quantum memories into a photonic circuit. *Physical Review X*, 5(3):031009, jul 2015.

[116] Yifan Zhu, Wenqi Wei, Ailun Yi, Tingting Jin, Chen Shen, Xudong Wang, Liping Zhou, Chengli Wang, Weiwen Ou, Sannian Song, Ting Wang, Jianjun Zhang, Xin Ou, and Jiaxiang Zhang. Hybrid integration of deterministic quantum dot-based single-photon sources with cmos-compatible silicon carbide photonics. *Laser & Photonics Reviews*, 16(9):2200172, sep 2022.

[117] Ashish Chanana, Hugo Larocque, Renan Moreira, Jacques Carolan, Biswarup Guha, Emerson G. Melo, Vikas Anant, Jindong Song, Dirk Englund, Daniel J. Blumenthal, Kartik Srinivasan, and Marcelo Davanco. Ultra-low loss quantum photonic circuits integrated with single quantum emitters. *Nature Communications*, 13:7693, 2022.

[118] Noel H. Wan, Tsung-Ju Lu, Kevin C. Chen, Michael P. Walsh, Matthew E. Trusheim, Lorenzo De Santis, Eric A. Bersin, Isaac B. Harris, Sara L. Mouradian, Ian R. Christen, Edward S. Bielejec, and Dirk Englund. Large-scale integration of artificial atoms in hybrid photonic circuits. *Nature*, 583(7815):226–231, jul 2020.

[119] Ling Xie, Tony X. Zhou, Rainer J. Stöhr, and Amir Yacoby. Crystallographic orientation dependent reactive ion etching in single crystal diamond. *Advanced Materials*, 30(11):1705501, mar 2018.

[120] Behzad Khanaliloo, Harishankar Jayakumar, Aaron C. Hryciw, David P. Lake, Hamidreza Kaviani, and Paul E. Barclay. Single-crystal diamond nanobeam waveguide optomechanics. *Physical Review X*, 5(4):041051, dec 2015.

[121] Behzad Khanaliloo, Matthew Mitchell, Aaron C. Hryciw, and Paul E. Barclay. High- q / v monolithic diamond microdisks fabricated with quasi-isotropic etching. *Nano Letters*, 15(8):5131–5136, aug 2015.

[122] Timothy P McKenna, Jeremy D Witmer, Rishi N Patel, Wentao Jiang, Raphaël Van Laer, Patricio Arrangoiz-Arriola, E Alex Wollack, Jason F Herrmann, and Amir H Safavi-Naeini. Cryogenic microwave-to-optical conversion using a triply resonant lithium-niobate-on-sapphire transducer. *Optica*, 7(12):1737–1745, 2020.

[123] Elke Neu, David Steinmetz, Janine Riedrich-Möller, Stefan Gsell, Martin Fischer, Matthias Schreck, and Christoph Becher. Single photon emission from silicon-vacancy colour centres in chemical vapour deposition nano-diamonds on iridium. *New Journal of Physics*, 13(2):025012, feb 2011.

[124] E. N. Knall, C. M. Knaut, R. Bekenstein, D. R. Assumpcao, P. L. Stroganov, W. Gong, Y. Q. Huan, P.-J. Stas, B. Machielse, M. Chalupnik, D. Levonian, A. Suleymanzade, R. Riedinger, H. Park, M. Lončar, M. K. Bhaskar, and M. D. Lukin. Efficient source of shaped single photons based on an integrated diamond nanophotonic system. *Physical Review Letters*, 129(5):053603, jul 2022.

[125] Tim Schröder, Matthew E. Trusheim, Michael Walsh, Luozhou Li, Jiabao Zheng, Marco Schukraft, Alp Sipahigil, Ruffin E. Evans, Denis D. Sukachev, Christian T. Nguyen, Jose L. Pacheco, Ryan M. Camacho, Edward S. Bielejec, Mikhail D. Lukin, and Dirk Englund. Scalable focused ion beam creation of nearly lifetime-limited single quantum emitters in diamond nanostructures. *Nature Communications*, 8(1):15376, aug 2017.

[126] Michael Titze, Heejun Byeon, Anthony Flores, Jacob Henshaw, C. Thomas Harris, Andrew M. Mounce, and Edward S. Bielejec. In situ ion counting for improved implanted ion error rate and silicon vacancy yield uncertainty. *Nano Letters*, 22(8):3212–3218, apr 2022.

[127] Madison Sutula, Ian Christen, Eric Bersin, Michael P. Walsh, Kevin C. Chen, Justin Mallek, Alexander Melville, Michael Titze, Edward S. Bielejec, Scott Hamilton, Danielle Braje, P. Benjamin Dixon, and Dirk R. Englund. Large-scale optical characterizaton of solid-state quantum emitters. *Nature Materials*, https://doi.org/10.1038/s41563-023-01644-8, 2022.

[128] Ali W. Elshaari, Iman Esmaeil Zadeh, Andreas Fognini, Michael E. Reimer, Dan Dalacu, Philip J. Poole, Val Zwiller, and Klaus D. Jöns. On-chip single photon filtering and multiplexing in hybrid quantum photonic circuits. *Nature Communications*, 8(1):379, dec 2017.

[129] G. Reithmaier, M. Kaniber, F. Flassig, S. Lichtmannecker, K. Müller, A. Andrejew, J. Vučković, R. Gross, and J. J. Finley. On-chip generation, routing, and detection of resonance fluorescence. *Nano Letters*, 15(8):5208–5213, aug 2015.

[130] Faraz Najafi, Jacob Mower, Nicholas C. Harris, Francesco Bellei, Andrew Dane, Catherine Lee, Xiaolong Hu, Prashanta Kharel, Francesco Marsili, Solomon Assefa, Karl K. Berggren, and

Dirk Englund. On-chip detection of non-classical light by scalable integration of single-photon detectors. *Nature Communications*, 6(1):5873, may 2015.

[131] Beibei Zeng, Chawina De-Eknamkul, Daniel Assumpcao, Dylan Renaud, Zhuoxian Wang, Daniel Riedel, Jeonghoon Ha, Carsten Robens, David Levonian, Mikhail Lukin, Mihir Bhaskar, Denis Sukachev, Marko Loncar, and Bart Machielse. Cryogenic optical packaging of nanophotonic devices with coupling loss ¡ 1 db. *Applied Physics Letters*, 123(16):161106, 10 2023.

[132] Arian J. Stolk, Kian L. van der Enden, Marie-Christine Slater, Ingmar te Raa-Derckx, Pieter Botma, Joris van Rantwijk, J. J. Benjamin Biemond, Ronald A. J. Hagen, Rodolf W. Herfst, Wouter D. Koek, Adrianus J. H. Meskers, René Vollmer, Erwin J. van Zwet, Matthew Markham, Andrew M. Edmonds, J. Fabian Geus, Florian Elsen, Bernd Jungbluth, Constantin Haefner, Christoph Tresp, Jürgen Stuhler, Stephan Ritter, and Ronald Hanson. Metropolitan-scale heralded entanglement of solid-state qubits. *Science Advances*, 10(44):eadp6442, 2024.

[133] L. J. Stephenson, D. P. Nadlinger, B. C. Nichol, S. An, P. Drmota, T. G. Ballance, K. Thirumalai, J. F. Goodwin, D. M. Lucas, and C. J. Ballance. High-rate, high-fidelity entanglement of qubits across an elementary quantum network. *Phys. Rev. Lett.*, 124:110501, Mar 2020.

[134] Stefan Langenfeld, Stephan Welte, Lukas Hartung, Severin Daiss, Philip Thomas, Olivier Morin, Emanuele Distante, and Gerhard Rempe. Quantum teleportation between remote qubit memories with only a single photon as a resource. *Phys. Rev. Lett.*, 126:130502, Mar 2021.

[135] R. Stockill, M. J. Stanley, L. Huthmacher, E. Clarke, M. Hugues, A. J. Miller, C. Matthiesen, C. Le Gall, and M. Atatüre. Phase-tuned entangled state generation between distant spin qubits. *Phys. Rev. Lett.*, 119:010503, Jul 2017.

[136] Andrei Ruskuc, Chun-Ju Wu, Emanuel Green, Sophie L. N. Hermans, Joonhee Choi, and Andrei Faraon. Multiplexed entanglement of multi-emitter quantum network nodes, 2025.

[137] P-J Stas, Yan Qi Huan, Bartholomeus Machielse, Erik N Knall, Aziza Suleymanzade, Benjamin Pingault, Madison Sutula, Sophie W Ding, Can M Knaut, Daniel R Assumpcao, et al. Robust multi-qubit quantum network node with integrated error detection. *Science*, 378(6619):557–560, 2022.

[138] David Hucul, Ismail V Inlek, Grahame Vittorini, Clayton Crocker, Shantanu Debnath, Susan M Clark, and Christopher Monroe. Modular entanglement of atomic qubits using photons and phonons. *Nature Physics*, 11(1):37–42, 2015.

[139] Colin D. Bruzewicz, John Chiaverini, Robert McConnell, and Jeremy M. Sage. Trapped-ion quantum computing: Progress and challenges. *Applied Physics Reviews*, 6(2):021314, 05 2019.

[140] Jonas Nils Becker and Christoph Becher. Coherence properties and quantum control of silicon vacancy color centers in diamond. *physica status solidi (a)*, 214(11):1700586, 2017.

[141] JD Wong-Campos, KG Johnson, B Neyenhuis, J Mizrahi, and C Monroe. High-resolution adaptive imaging of a single atom. *Nature Photonics*, 10(9):606–610, 2016.

[142] Alessandro Laneve, Giuseppe Ronco, Mattia Beccaceci, Paolo Barigelli, Francesco Salusti, Nicolas Claro-Rodriguez, Giorgio De Pascalis, Alessia Suprano, Leone Chiaudano, Eva Schöll, et al. Quantum teleportation with dissimilar quantum dots over a hybrid quantum network. *Nature Communications*, 16(1):10028, 2025.

[143] Pascale Senellart, Glenn Solomon, and Andrew White. High-performance semiconductor quantum-dot single-photon sources. *Nature nanotechnology*, 12(11):1026–1039, 2017.

[144] Edo Waks and Jelena Vuckovic. Dipole induced transparency in drop-filter cavity-waveguide systems. *Phys. Rev. Lett.*, 96:153601, Apr 2006.

[145] Andrei Faraon, Ilya Fushman, Dirk Englund, Nick Stoltz, Pierre Petroff, and Jelena Vučković. Dipole induced transparency in waveguide coupled photonic crystal cavities. *Opt. Express*, 16(16):12154–12162, Aug 2008.

[146] Erika Janitz, Mihir K. Bhaskar, and Lilian Childress. Cavity quantum electrodynamics with color centers in diamond. *Optica*, 7(10):1232–1252, Oct 2020.

[147] GL Van De Stolpe, LJ Feije, SJH Loenen, Antariksha Das, GM Timmer, TW De Jong, and TH Taminiau. Check-probe spectroscopy of lifetime-limited emitters in bulk-grown silicon carbide. *NPJ Quantum Information*, 11(1):31, 2025.

[148] Gregor Pieplow, Yannick Strocka, Mariano Isaza-Monsalve, Joseph H. D. Munns, and Tim Schröder. Deterministic creation of large photonic multipartite entangled states with group-iv color centers in diamond. *arXiv preprint arXiv:2312.03952*, 2023.

[149] Anpan Han, Bingdong Chang, Matteo Todeschini, Hoa Thanh Le, William Tiddi, and Matthias Keil. Inductively coupled plasma nanoetching of atomic layer deposition alumina. *Microelectronic Engineering*, 193:28–33, 2018.

[150] Linsen Li, Lorenzo De Santis, Isaac BW Harris, Kevin C Chen, Yihuai Gao, Ian Christen, Hyeongrak Choi, Matthew Trusheim, Yixuan Song, Carlos Errando-Herranz, et al. Heterogeneous integration of spin–photon interfaces with a cmos platform. *Nature*, 630(8015):70–76, 2024.

[151] Jonathan C Lee, Andrew P Magyar, David O Bracher, Igor Aharonovich, and Evelyn L Hu. Fabrication of thin diamond membranes for photonic applications. *Diamond and related materials*, 33:45–48, 2013.

[152] Lillian B Hughes, Zhiran Zhang, Chang Jin, Simon A Meynell, Bingtian Ye, Weijie Wu, Zilin Wang, Emily J Davis, Thomas E Mates, Norman Y Yao, et al. Two-dimensional spin systems in pecvd-grown diamond with tunable density and long coherence for enhanced quantum sensing and simulation. *APL Materials*, 11(2), 2023.

[153] Sorawis Sangtawesin, Bo L. Dwyer, Srikanth Srinivasan, James J. Allred, Lila V. H. Rodgers, Kristiaan De Greve, Alastair Stacey, Nikolai Dontschuk, Kane M. O'Donnell, Di Hu, D. Andrew Evans, Cherno Jaye, Daniel A. Fischer, Matthew L. Markham, Daniel J. Twitchen, Hongkun Park, Mikhail D. Lukin, and Nathalie P. de Leon. Origins of diamond surface noise probed by correlating single-spin measurements with surface spectroscopy. *Phys. Rev. X*, 9:031052, Sep 2019.

[154] Ravi Kumar, Saksham Mahajan, Felix Donaldson, Siddharth Dhomkar, Hector J. Lancaster, Curran Kalha, Aysha A. Riaz, Yujiang Zhu, Christopher A. Howard, Anna Regoutz, and John J. L. Morton. Stability of near-surface nitrogen vacancy centers using dielectric surface passivation. *ACS Photonics*, 11(3):1244–1251, 2024.

[155] U. Schlarb and K. Betzler. Refractive indices of lithium niobate as a function of temperature, wavelength, and composition: A generalized fit. *Physical Review B*, 48(21):15613–15620, 1993.

[156] Moritz Bartnick, Matteo Santandrea, Jan Philipp Höpker, Frederik Thiele, Raimund Ricken, Viktor Quiring, Christof Eigner, Harald Herrmann, Christine Silberhorn, and Tim J. Bartley. Cryogenic second-harmonic generation in periodically poled lithium niobate waveguides. *Physical Review Applied*, 15(2):1, 2021.

[157] David E. Zelmon, David L. Small, and Dieter Jundt. Infrared corrected sellmeier coefficients for congruently grown lithium niobate and 5 mol *Journal of the Optical Society of America B*, 14(12):3319, 1997.

[158] Giorgio Turri, Scott Webster, Ying Chen, Benjamin Wickham, Andrew Bennett, and Michael Bass. Index of refraction from the near-ultraviolet to the near-infrared from a single crystal microwave-assisted cvd diamond. *Optical Materials Express*, 7(3):855, 2017.

[159] I. H. Malitson. Interspecimen comparison of the refractive index of fused silica. *Journal of the Optical Society of America*, 55(10):1205, 1965.